Dark-field Chest Radiography –
Image Artifacts and COPD Assessment

Author:
Theresa Urban

Supervisor:
Prof. Dr. Franz Pfeiffer

PhD Thesis

Chair of Biomedical Physics
School of Natural Sciences
Technical University of Munich

July 2023

TECHNISCHE UNIVERSITÄT MÜNCHEN
TUM School of Natural Sciences

Dark-field Chest Radiography – Image Artifacts and COPD Assessment

Theresa Urban

Vollständiger Abdruck der von der TUM School of Natural Sciences der Technischen Universität München zur Erlangung des akademischen Grades einer

Doktorin der Naturwissenschaften (Dr. rer. nat.)

genehmigten Dissertation.

Vorsitz:	Prof. Dr. David Egger
Prüfer*innen der Dissertation:	1. Prof. Dr. Franz Pfeiffer
	2. Prof. Dr. Daniel Rückert

Die Dissertation wurde am 06.07.2023 bei der Technischen Universität München eingereicht und durch die TUM School of Natural Sciences am 08.08.2023 angenommen.

Contents

Acknowledgments **v**

Abstract **vii**

Zusammenfassung **ix**

1 Introduction **1**

2 Background **3**
- 2.1 Conventional X-ray Imaging Methods . . . 3
  - 2.1.1 Conventional thorax radiography . . . 3
  - 2.1.2 Chest CT . . . 4
- 2.2 Dark-field Radiography . . . 4
  - 2.2.1 Dark-field signal formation . . . 5
  - 2.2.2 Grating-based dark-field X-ray imaging . . . 5
  - 2.2.3 The clinical dark-field chest radiography system . . . 7
- 2.3 COPD and the Human Lung . . . 8
  - 2.3.1 Healthy lungs . . . 8
  - 2.3.2 COPD lungs . . . 9

3 Image Artifacts **11**
- 3.1 Motivation . . . 11
- 3.2 Theory . . . 13
  - 3.2.1 Detector crosstalk . . . 13
  - 3.2.2 Scatter . . . 14
  - 3.2.3 Beam hardening . . . 15
- 3.3 Methods . . . 16
  - 3.3.1 Monte-Carlo simulations . . . 16
  - 3.3.2 Detector crosstalk . . . 17
  - 3.3.3 Scatter from the analyzer grating . . . 18
  - 3.3.4 Sample scatter . . . 19
  - 3.3.5 Beam hardening . . . 21
  - 3.3.6 Validation phantoms . . . 22
  - 3.3.7 Image processing chain . . . 22
- 3.4 Results . . . 24
  - 3.4.1 Detector crosstalk . . . 24
  - 3.4.2 Scatter from the analyzer grating . . . 25
  - 3.4.3 Sample scatter . . . 28
  - 3.4.4 Beam hardening . . . 31
  - 3.4.5 Quantitative validation of corrections with phantoms . . . 32
  - 3.4.6 Application to dark-field chest radiographs . . . 35
- 3.5 Discussion . . . 36

4 Application for COPD Assessment **41**
- 4.1 Medical Context . . . 41
- 4.2 Quantitative Dark-field Radiography . . . 42
- 4.3 Methods . . . 42
  - 4.3.1 Participants . . . 43
  - 4.3.2 Imaging protocols . . . 43
  - 4.3.3 Quantitative image analysis . . . 43

- 4.3.4 Reader study . . . 44
- 4.3.5 Statistical analysis . . . 45
- 4.4 Results . . . 45
  - 4.4.1 Subjects . . . 45
  - 4.4.2 Dark-field chest radiography of healthy lungs . . . 45
  - 4.4.3 Dark-field chest radiography for pulmonary emphysema . . . 46
  - 4.4.4 Comparison of conventional and dark-field chest radiography . . . 49
- 4.5 Discussion . . . 51

5 Conclusion **55**

Bibliography **57**

List of Figures **65**

List of Tables **67**

List of Abbreviations **69**

Scientific Contributions **71**

Acknowledgments

This work would not have been possible without the previous work by my countless predecessors in research or the trust and support of many people working with me. I want to thank all of them. Specifically, I want to thank ...

- the european, german, and bavarian tax payers and all relevant institutions and decision makers – for funding research in general, and this project and through it my position here at TUM and MRI in particular.
- Franz Pfeiffer – for getting me to work on dark-field radiography, for trusting me with this project, for supporting, guiding and teaching me, and for providing the infrastructure. Thank you for the opportunities and encouragement to attend national and international medical and physics conferences, and also for the summer school. I enjoyed working here at the E17 Chair a lot for both its scientific and social environment.
- the initial patient scanner team around Konsti, Wolfgang, and Fabio – for teaching me everything about dark-field imaging in general and the patient scanner specifically, and for showing me how to do research as a PhD student.
- the second generation working with me at the patient scanner, i.e. Manu, Henriette, and Rafael – for the great environment in our little clinics group, for discussing POM, scatter, reader study setups, and everything else with me, and for the many relaxing breaks in between. Manu and Henriette, a special thanks for proof-reading parts of this thesis.
- the medical team in the clinics around Daniela, Andi, Alex, and Flo – for your efforts for the clinical studies from planning and writing BfS proposals to acquiring patients, performing reader studies, and discussing the results. A special thanks goes to Flo for making me plan, write, and review papers with him at this pace, for his contagious motivation and his many ideas for further projects.
- the team at Philips Research, specifically Thomas in Hamburg and Klaus-Jürgen in Eindhoven – for the regular instructive and worthwhile discussions, and for the ensuing motivation to dig deeper whenever I did not understand something.
- my Masters students Maggie, Philipp, Jule, and Sandra – for teaching me how to (and how not to) supervise students and for their contributions to this work.
- the E17 IT team around Martin, Wolfgang, and Clemens – for providing the infrastructure, for enabling me to work in Garching, in the clinics, and at home, for solving my problems, and for showing me how to solve them myself. A special thanks to Wolfgang for `xpreen`.
- the radiology IT team and medical physicists David, Felix, Christiane and Bernhard – for all the work on the inclusion of the patient scanner into clinical routine, especially for countless PACS fixes.
- Nelly and Veronica – for all the administrative work related to ordering equipment, to going to conferences and on business trips, and to getting keys.
- the Powerpuffs Lisa, Manu, and Kersti – for their friendship, for making me come to Garching every once in a while, for hopefully organising my upcoming defense, and for keeping me entertained through lockdowns.
- Konsti, Wolfgang, and Manu – for being a great team when I first came to this group, and for being great friends soon after that.
- all past and current members of E17 – for the great time I had here.

Abstract

X-ray imaging is widely employed in industry and medicine for non-destructive assessment of internal sample features. In conventional X-ray imaging, the image contrast is based on the different attenuation of X-rays in different materials. Thus, it offers good contrast for imaging samples that contain materials with very different attenuation, such as bone, soft tissue, and air in medical imaging.
Grating-based dark-field X-ray imaging in contrast is sensitive to both attenuation and additionally ultra-small-angle scattering of X-rays. The associated additional modality is called the dark-field image. To measure these modalities simultaneously, an interferometer is used to imprint a fine intensity pattern onto the X-ray beam. The pattern characteristics mean intensity and contrast encode attenuation and dark-field signal, respectively.
This novel imaging technique has raised great interest in the last 15 years. For medical applications, numerous pre-clinical studies have shown its potential for lung assessment: With its many air-tissue interfaces causing ultra-small-angle scattering, tissue with intact alveolar structure generates a strong dark-field signal. Diseases that impair the alveolar integrity lead to a loss of dark-field signal.
The translation to clinical application has recently made a big step forward: A first clinical system for dark-field chest radiography was installed and is currently used in patient studies to evaluate the technique's diagnostic potential in humans.

This thesis works with this dark-field chest radiography system to improve and evaluate the diagnostic value of the obtained radiographs.
First, image quality and quantitative accuracy are improved by investigating image artifacts and establishing corrections for them. Besides the well-known sample scatter it is demonstrated that X-ray scatter at the interferometer as well as detector crosstalk also create artifacts in the dark-field radiographs. For the associated artifacts, deconvolution-based correction methods are established. The kernel for detector crosstalk is measured and fitted to a model. For the kernel for scatter from the interferometer, the system is implemented in a Monte-Carlo simulation. To estimate scatter from the sample, an adapted algorithm originally developed for scatter correction in conventional radiography is used. The estimated scatter and crosstalk intensities are validated with a variety of simulations and measurements.
Beam hardening also creates artifacts in dark-field radiographs. Its impact in the clinical dark-field chest radiography sytem is characterized with calibration measurements with purely attenuating materials. These yield a look-up table to connect attenuation to the associated beam hardening induced dark-field signal.
Images of well-known phantoms prove that the established corrections work well. Finally, the impact of detector crosstalk, scatter from the interferometer, scatter from the sample, and beam hardening and their successful correction are shown on dark-field radiographs of a human thorax.

The second part of this thesis evaluates the diagnostic value of dark-field chest radiography for assessment of a wide-spread lung disease, COPD. For a quantitative evaluation, the dark-field coefficient is introduced, which describes the dark-field signal generated per length of tissue.
The dark-field radiographs are analyzed for their capability to assess the severity of pulmonary emphysema, the main manifestation of COPD, using CT scans as reference. The dark-field coefficient shows a strong correlation with the emphysema index from quantitative CT evaluation, and decreases with emphysema severity from visual CT evaluation. Signal losses in the dark-field radiograph and CT-based emphysema localization agree very well.
Further, it is demontrated that dark-field chest radiography outperforms conventional radiography for emphysema diagnosis and staging in a reader study comparing the two imaging methods.

The established corrections increase the diagnostic value of dark-field chest radiography, and the evaluations prove the technique's potential as a low-dose, image-based tool for emphysema assessment. Thus, this thesis constitutes an important step in the way towards clinical application of dark-field chest radiography.

Zusammenfassung

Die Röntgenbildgebung wird in der Industrie und der Medizin häufig zur zerstörungsfreien Untersuchung des Inneren von Proben eingesetzt. Der Bildkontrast in der konventionellen Röntgenbildgebung basiert auf der unterschiedlichen Abschwächung von Röntgenstrahlen in verschiedenen Materialien. Daher bietet sie einen guten Kontrast bei Proben, die sehr unterschiedlich abschwächende Materialien enthalten, wie beispielsweise Knochen, Weichgewebe und Luft in der medizinischen Bildgebung.

Die Dunkelfeld-Röntgenbildgebung hingegen stellt sowohl die Abschwächung als auch zusätzlich die Ultrakleinwinkelstreuung der Röntgenstrahlen dar. Diese zusätzliche Modalität wird als Dunkelfeldbild bezeichnet. Mithilfe eines Interferometers können die beiden Modalitäten gleichzeitig gemessen werden. Dem Röntgenstrahl wird dabei ein feines Intensitätsmuster aufgeprägt, dessen mittlere Intensität die Abschwächung und dessen Kontrast das Dunkelfeld zeigt.

Diese neuartige Bildgebungsmethode hat in den letzten 15 Jahren großes Interesse geweckt. Für medizinische Anwendungen haben zahlreiche prä-klinische Studien das Potenzial für die Beurteilung der Lunge gezeigt: Mit seinen vielen Grenzflächen von Luft und Gewebe, die Ultrakleinwinkelstreuung verursachen, erzeugt eine intakte Alveolarstruktur ein starkes Dunkelfeldsignal. Lungenerkrankungen, die die Alveolarstruktur beeinträchtigen, führen zu einem Signalverlust.

Die Übertragung in die klinische Anwendung hat kürzlich einen großen Schritt nach vorn gemacht: Ein erstes klinisches System für die Dunkelfeld-Thoraxradiographie wurde gebaut und wird derzeit in Patientenstudien eingesetzt, um das diagnostische Potenzial der Technik beim Menschen zu untersuchen.

Die vorliegende Arbeit verbessert und untersucht den diagnostischen Wert der mit diesem System gewonnenen Bilder. Zunächst werden die Bildqualität und die quantitative Genauigkeit verbessert, indem Bildartefakte untersucht und Korrekturen dafür etabliert werden. Es wird gezeigt, dass neben der bekannten Streuung an der Probe auch Streuung am Interferometer sowie das Übersprechen im Detektor Artefakte in den Dunkelfeldbildern erzeugen. Für diese werden entfaltungsbasierte Korrekturverfahren entwickelt. Der Kernel für das Detektorübersprechen wird gemessen und an ein Modell angepasst. Der Kernel für die Streuung am Interferometer wird mit einer Monte-Carlo-Simulation des Systems berechnet. Zur Schätzung der Streuung von der Probe wird ein für dieses System angepasster Algorithmus verwendet, der ursprünglich für Streuungskorrektur in der konventionellen Radiographie entwickelt wurde. Die geschätzten Intensitäten werden mit einer Reihe von Simulationen und Messungen validiert.

Strahlaufhärtung erzeugt ebenfalls Artefakte in Dunkelfeldbildern. Dieser Effekt wird durch Messungen an rein schwächenden Materialien charakterisiert. Dabei wird eine Nachschlage-Tabelle erstellt, die die Schwächung einer Probe mit dem durch die Strahlaufhärtung verursachten Dunkelfeldsignal in Verbindung bringt.

Bilder von bekannten Phantomen beweisen, dass die vorgestellten Korrekturen gut funktionieren. Schließlich werden die Auswirkungen von Detektorübersprechen, Streuung am Interferometer, Streuung an der Probe und Strahlaufhärtung und deren erfolgreiche Korrektur an Dunkelfeld-Röntgenaufnahmen eines menschlichen Thorax gezeigt.

Im zweiten Teil dieser Arbeit wird der diagnostische Wert der Dunkelfeld-Thoraxradiographie zur Beurteilung einer weit verbreiteten Lungenerkrankung, der COPD, untersucht. Zur quantitativen Auswertung wird der Dunkelfeldkoeffizient eingeführt, der das pro Gewebelänge erzeugte Dunkelfeldsignal beschreibt.

Die Dunkelfeld-Bildgebung wird auf ihre Fähigkeit hin untersucht, Lungenemphyseme, eine der Hauptmanifestationen der COPD, darzustellen, wobei CT-Aufnahmen als Referenz dienen. Der Dunkelfeldkoeffizient zeigt eine starke Korrelation mit dem Emphysemindex aus der quantitativen CT-Auswertung, und nimmt mit zunehmendem Schweregrad des Emphysems aus der visuellen Bewertung der CT-Aufnahmen ab. Die Signalverluste in Dunkelfeld-Röntgenaufnahmen und die CT-basierte Emphysemlokalisierung stimmen ebenfalls sehr gut überein.

Schließlich wird in einer Reader-Studie, die die beiden Bildgebungsverfahren vergleicht, gezeigt, dass die Dunkelfeld-Thoraxradiographie der konventionellen Radiographie bei der Emphysemdiagnose und -einstufung überlegen ist.

Die ermittelten Korrekturen erhöhen den diagnostischen Wert der Dunkelfeld-Thoraxradiographie, und die Auswertungen belegen das Potenzial der Technik als bildgebendes Instrument zur Emphysembeurteilung mit geringer Dosis. Damit stellt diese Arbeit einen wichtigen Schritt auf dem Weg zur klinischen Anwendung der Dunkelfeld-Röntgenbildgebung dar.

Chapter 1

Introduction

X-ray imaging is a tool widely used in both medicine and industry for non-destructive investigation of the internal structures of a sample that are otherwise inaccessible. Contrast formation is based on the attenuation of X-rays: dense materials attenuate X-rays more than materials with lower density. By recording the intensity reduction of X-rays after passing the sample, an X-ray examination allows to draw conclusions about the sample's interior without destroying it.

Context

X-ray imaging has been an active field of research in physics and medicine alike for more than 100 years. Researchers are deveolping contrast agents and spectral imaging to increase image contrast, improving X-ray sources and detectors to enhance image quality and resolution, or finding new acquisition protocols and image processing methods to reduce artifacts, cost, time, or – for medical imaging – applied dose.

Another target point for research in X-ray imaging is using other underlaying X-ray mechanisms for image contrast generation. When passing through matter, X-rays are subjected not only to attenuation, but also to phase shift and scattering. These processes are complimentary to attenuation, i.e. they offer additional information on other sample properties. Thus, they are of high interest, especially in cases where the attenuation alone cannot provide the wanted information. However, as X-ray detectors can only measure the intensity of X-rays, measuring these processes is quite difficult.

A number of methods have been developed in basic research to convert a phase shift of the X-ray wave to a change in intensity on the detector [1–6]. All of them rely on some level of interference of X-rays after the sample. Thus, they have high demands on X-ray coherence and could for a long time only be investigated at synchrotron facilities, preventing a wide-spread application.

One of these methods is grating-based X-ray imaging, also first developed and used at synchrotron facilities [6]: a grating imprints a very fine intensity pattern onto the X-ray beam, and a second grating allows to extract pattern characteristics without resolving it [7]. In 2006, a system featuring an additional third grating was developed that enabled the use of conventional X-ray sources [8]. This led to a high research activity regarding this method and possible applications, and in 2008, the so-called X-ray dark-field imaging contrast was introduced as a third modality, in addition to attenuation and phase shift [9]. It is called dark-field in analogy to visible light dark-field microscopy: The dark-field signal originates from spatial fluctuations of the wavefront due to unresolved micro-structures in the sample [10]. These spatial fluctuations are induced by ultra-small-angle scattering at inhomogeneities in the sample's electron density, i.e. material interfaces, which are too fine and numerous to be resolved individually. The length scale of material interfaces the system is sensitive to depends on system parameters and is typically in the micrometer range [11]. The dark-field signal is the stronger the more of these microscopic material interfaces the beam passes through [12]. Such interfaces are present in porous structures such as foam, in powders, in fibrous structures such as wood, or in the alveolar structure of the lung. Homogeneous materials, such as aluminum or water, do not generate any dark-field signal. Thus, dark-field imaging allows to get information on the sample's micro-structure, without resolving it directly.

Possible medical applications of grating-based dark-field X-ray imaging have ever since been of high interest. Extensive studies on phantoms, small animals, and ex-vivo human samples investigated the value of dark-field radiography and soon also dark-field computed tomography for different diseases. Besides imaging of joints [13] and bones [14], gout assessment [15], and mammography [16, 17], imaging of the lung soon proved to be a promising target [18–24].

The translation to human lung imaging took some time, mainly because of the size of the human thorax and associated difficulties in the production of the necessary gratings. After some further development in grating hardware [25, 26], and image acquisition precedures [27, 28], studies in in-vivo pigs [29, 30] and ex-vivo humans [31, 32] proved the potential and feasibility of dark-field chest radiography in humans. Finally, in 2018, a first system for clinical dark-field chest radiography was installed and commissioned at the Klinikum rechts der Isar, the university hospital of the Technical University of Munich [33].

There are a number of patient studies currently conducted with this clinical dark-field chest radiography system to investigate the diagnostic potential of this new technique.

The collaboration

The mentioned clinical dark-field chest radiography system is the product of a collaborative effort of fellow PhD students and other researchers from the Physics Department of the Technical University of Munich, from the Radiology Department of the Klinikum rechts der Isar, and from Philips Research in Hamburg.

Lukas Gromann, Fabio De Marco, Konstantin Willer, and Jana Andrejewski laid the ground work by developing, evaluating, and improving the preceding large field of view dark-field system for pre-clinical studies. Konstantin Willer conceived and technically implemented the current clinical dark-field chest radiography system together with Fabio De Marco, Alex Gustschin, Bernhard Gleich, Manuela Frank, and myself. In parallel, Wolfang Noichl and Fabio De Marco advanced image reconstruction algorithms specifically for this system. Manuela Frank, Konstantin Willer, and myself evaluated patient dose and established patient exposure protocols, and me and Rafael Schick still work on further advancements of image reconstruction for artifact correction and dose reduction. Dr. Thomas Koehler from Philips Research continues to provide support in all these aspects.

The clinical evaluation of dark-field chest radiography was and still is also done in a multidisciplinary team in a number of patient studies. The lung diseases currently investigated are chronic obstructive pulmonary disease (COPD) with pulmonary emphysema as its main manifestation, COVID-19 pneumonia, pneumothorax, and lung cancer. The involved people are Konstantin Willer, Manuela Frank, Henriette Bast, Rafael Schick, and myself under the lead of Prof. Franz Pfeiffer from the physics department, as well as Alexander Fingerle, Andreas Sauter, and Florian Gassert under the lead of Prof. Daniela Pfeiffer from the radiology department. Clinicians from the departments for pulmonology and thorax surgery are also involved.

The corresponding publications, PhD theses, and habilitation reports of these people provide further reading on dark-field chest radiography for lung assessment.

Additional value of this thesis

In the first part of this thesis (chapter 3), the clinical dark-field chest radiography system is characterized regarding its image and contrast formation, with a focus on possible artifacts in the dark-field image. Four sources of artifacts, namely detector crosstalk, scatter from the gratings, scatter from the sample, and beam hardening, are invesigated with Monte-Carlo simulations and measurements. For each of them, a method to correct the obtained images is developed and validated, to ensure an unobstructed evaluation of dark-field radiographs.

In the second part of this thesis (chapter 4), a patient study is conducted and evaluated to assess the diagnostic potential of dark-field chest radiography for assessment of COPD, a lung disease that destroys the alveolar integrity of lung tissue. Dark-field radiographs are evaluated qualitatively, quantitatively, and in a reader study, using X-ray computed tomography (CT) scans as reference.

Overall, this thesis aims to increase and evaluate the diagnostic value of dark-field chest radiography, and thereby promote its clinical application for lung assessment.

Chapter 2

Background

Medical imaging includes a variety of imaging modalities. There are a number of different magnetic resonance imaging (MRI) methods, ultrasound, functional imaging methods such as positron emission tomography (PET) and single photon emission computed tomography (SPECT), X-ray imaging methods such as CT and radiography [34], and many more. These methods come with different imaging characteristics, such as resolution, image contrast, radiation dose, or cost, and they are used for specific diagnostic purposes. There is active research going on in all fields of medical imaging. As it is the focus of this thesis, only X-ray imaging will be explained in further detail.

2.1 Conventional X-ray Imaging Methods

Conventional X-ray imaging is a non-destructive, pain-free and relatively fast imaging method widely used in clinical routine. It uses the attenuation of X-rays to form the image contrast. The attenuation is due to interactions of the X-rays with matter, where the interaction probabilities differ depending on X-ray energy and material properties [35]. Thus, different materials can be distinguished based on their different X-ray attenuation properties. With X-ray imaging, it is possible to obtain information about internal structures of a sample that is otherwise inaccessible.

With energies in the range of tens of keV, X-rays have sufficiently high and sufficiently different interaction probabilities with materials common in the human body, and a sufficient portion of them reaches the detector. The exact energy spectrum of the X-rays is chosen depending on the specific application. Electromagnetic waves with much higher energies are not suitable because of their lower and more similar interaction probabilities, while electromagnetic waves with much lower energies, such as visible light, are attenuated completely.

All X-ray imaging methods expose the patient to ionizing radiation, whose negative effect on the patient, described by the effective patient dose, depends on the overall exposure and the imaged body part. The expected diagnostic benefit of an X-ray imaging procedure has to justify the applied radiation dose [36]. This trade-off is the starting point of most research in medical X-ray imaging: The aim is usually to achieve higher diagnostic value, lower radiation dose, or both. There are mainly three different methods of diagnostic X-ray imaging [34]: Plain radiography provides a single two-dimensional projection of the imaged sample, called a radiograph. Fluoroscopy allows the acquisition of multiple radiographs in short time intervals, yielding real-time moving images. CT acquires many projections from many different angles, and generates overlap-free cross-sectional images of the sample. As this work focuses on imaging the lung, only CT and conventional radiography of the thorax will be explained in further detail.

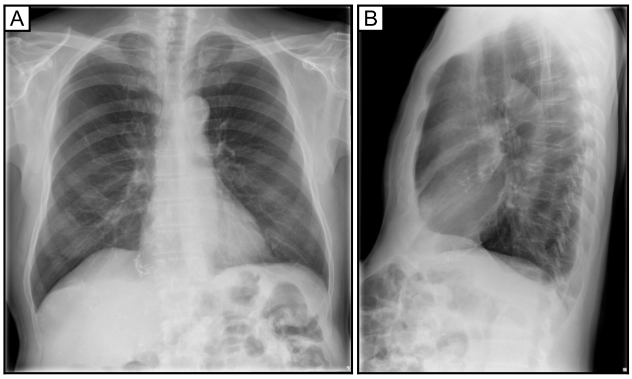

Figure 2.1: Conventional radiograph of the thorax of a 74-year old man. **A**, posterior-anterior orientation. **B**, lateral orientation.

2.1.1 Conventional thorax radiography

Plain radiography is the simplest of the X-ray imaging methods. Conventional thorax radiography is often used for the initial assessment of the lung. X-ray machines consist of an X-ray tube operated with a tube voltage of typically 120 kVp and a flat-panel detector. The distance between source and detector is usually 180 cm. The patient is standing upright close to the detector. Typical exposure times are in the range of a few µs, during which the patient is advised to hold breath. Typical effective doses for a posterior-anterior (pa) radiograph are in the range of 0.2 µSv [37].

Exemplary thorax radiographs in pa and lateral (lat) orientation of a 74-year old man are shown in fig. 2.1. The outlines of bones, soft tissue, and the lung can clearly be distinguished, and also finer structures like

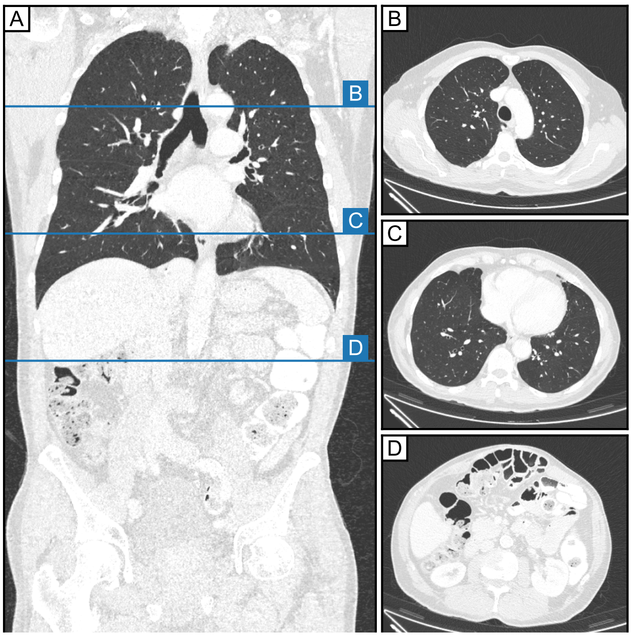

Figure 2.2: Exemplary slices from a CT scan with iodinated contrast agent of the thorax and abdomen of a 74-year old man in the lung window (-1350 HU to 150 HU). **A**, coronal slice. **B**, **C**, **D**, axial slices, at the locations indicated in **A**.

the vessels in the lung are visible. However, due to the projection, tissues in the same beam path overlap, impeding the diagnostic value of radiography.

Conventional radiographs are usually post-processed to increase the image contrast of fine structures and to reduce noise for an optimal evaluation by radiologists. This contrast enhancement renders the radiographs qualitative only.

2.1.2 Chest CT

CT uses an X-ray tube and a detector on a gantry that is rotated around the patient who is lying in supine position, i.e. on their back. Even though the gantry is rotating with a few Hz, due to the large field of view the overall image acquisition takes a few tens of seconds, during which the patient is advised to hold breath. Slices in coronal and axial reformation from an CT-scan of the thorax and abdomen of the same patient as in fig. 2.1 are shown in fig. 2.2. There is no more overlap of tissues, and e.g. the finer structures of the lung and the heart can be assessed much better than in plain radiography.

CT imaging is quantitative and voxel attenuation is usually given in Hounsfield units (HU). Even though HU values may vary with the used machine, the applied dose and reconstruction algorithm [38], quantitative CT evaluation is often used in clinical practice [39].

The dose for a standard chest CT scan is about 7 mSv[40]. Even though a significant dose reduction is possible by using low-dose techniques [41], still a radiation exposure of 1.4 mSv to 2.4 mSv is applied [42]. Since the contrast between different soft tissues and organs in the abdomen is quite low, contrast agent, in most cases iodine, is used to enhance the attenuation of tissues depending on their blood circulation. However, this comes with the risk of adverse effects such as allergic reactions [43].

Another possibility to enhance the contrast is spectral CT, where the attenuation for different X-ray energy spectra is recorded separately. By comparing the attenuation of tissues for the different spectra, more information on the material under investigation can be provided. Especially in the research community, spectral CT imaging has recently been further promoted by the introduction of a commercially available photon counting CT [44].

2.2 Dark-field Radiography

Dark-field radiography is an emerging new X-ray imaging modality. Similar to dark-field microscopy with visible light, it uses not attenuation, but the so-called ultra-small-angle scattering at microscopic material interfaces for image contrast generation, and is thus sensitive to the micro-structural properties of the sample.

X-ray dark-field imaging with conventional X-ray tubes was first reported in 2008 [9], and its potential for medical imaging applications was investigated in animal studies soon after. Its main advantage is whenever a disease generates, alters, or destroys the micro-structure of a tissue or organ while maintaining its attenuation properties, such as gout forming crystals in the joints [15, 45], breast tumors forming microcalcifications [17, 46], osteoporosis altering trabecular bone structure [14, 47], or pulmonary diseases affecting the alveolar structure of the lung [20, 22–24, 48–51].

After extensive research in animal models, the lung with its alveolar structure was determined as the most promising candidate for further research focusing on clinical application in humans. Nevertheless, there is also active research towards clinical application of dark-field imaging for other diseases.

For dark-field chest radiography, an experimental prototype for samples lying on an experimental table was developed at this Chair. After successful imaging of pigs [29, 52] and human cadavers [30–32], a system for dark-field chest radiography in living humans was conceived and installed at the Department for Diagnostic and Interventional Radiology at the Klinikum rechts der Isar of the Technical University of Munich [53, 54]. It was cleared for application by the authorities in autumn 2018. This dark-field chest radiography system is used, characterized and evaluated throughout this thesis. A detailed explanation of its working principle and more details on the system will be given in the following.

2.2.1 Dark-field signal formation

Measuring not only attenuation but also the scattering of X-rays at a sample has been used to investigate the sample's inner structure long before the development of X-ray dark-field imaging. Using the information of X-rays scattered forward at small angles, the so-called small-angle X-ray scattering (SAXS), allows to draw conclusions about sample structures in the nanometer range, and has been developed and investigated at synchrotron sources for the last century [35, 55].

SAXS [55, 56] is an X-ray technique that measures the scattered intensity of coherent X-rays with energies typically in the keV range at relatively small angles in the orders of mrad. The exploited physical effect is the coherent scattering of X-rays at electrons in the sample. As the binding energy of electrons is typically much smaller than the X-ray energy, the electrons can be considered free.

The incoming X-rays and the scattering process are coherent, i.e. the phase of the electromagnetic wave is known after the scattering process. This means that all scattered waves from the different electrons in the sample need to be superimposed before calculating the scattered intensity, and interference effects between waves scattered at different electrons need to be included. In doing so, it is also usually assumed that there is only one interaction per wave in the sample, i.e. there is no multiple scattering (the so-called kinematic scattering approximation). It can be shown that the resulting scattered intensity distribution is the Fourier transform of the electron density distribution of the sample [55].

Due to the reciprocity in the Fourier transform, smaller angles correspond to larger structures [55]. Typically, the measured small angles in SAXS experiments are in the range of mrad, leading to information on the sample's structure on nanometer scales [56].

Dark-field X-ray imaging can be thought of as the extension of SAXS towards smaller angles [11, 57], thus being sensitive to larger sample structures in the micrometer range. This is reflected in the description of the origin of the dark-field signal as ultra-small-angle scattering.

2.2.2 Grating-based dark-field X-ray imaging

There are different methods to measure the dark-field signal. For conventional X-ray sources, there is either edge illumination [58, 59], or grating-based dark-field imaging [8, 9]. As the setup used in this work employs grating-based dark-field imaging, this method will be explained in further detail.

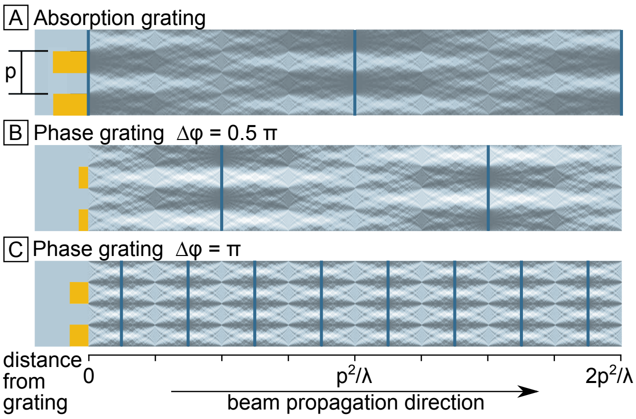

Figure 2.3: Exemplary intensity distributions, called Talbot carpets, behind a **A**, attenuating **B**, $\pi/2$-phase-shifting and **C**, π-phase-shifting grating. The dark blue lines indicate the periodic intensity patterns occurring in certain distances of the grating. Figure color-adapted from [60].

The Talbot effect

Grating-based X-ray dark-field imaging uses the Talbot effect [61]: Inserting a periodic structure into the X-ray beam generates a periodic intensity pattern similar to the inserted structure in certain distances. This periodic structure is commonly referred to as a grating, and the contrast of the intensity pattern, i.e. amplitude over mean intensity, is called visibility.

The periodic distances d_{talbot} in which the periodic intensity patterns with the highest visibility occur depend on the period of the structure p and the wavelength of the X-rays λ [62]:

$$d_{\text{talbot}} = n\ p^2/\lambda\ . \tag{2.1}$$

The factors n depend on the grating. It can be either attenuating or phase-shifting [63, 64]. Exemplary intensity distributions, called Talbot carpets, behind an attenuating, a $\pi/2$-phase-shifting and a π-phase-shifting grating are shown in fig. 2.3. For X-rays, whose wavelengths are in the order of tens of pm, grating periods in the order of a few µm are necessary to achieve practical Talbot distances of a few meters.

Contrast mechanisms

A sample in the beam path alters the intensity pattern generated by the grating as shown in fig. 2.4: Attenuating material leads to an overall reduction of the intensity, while the pattern visibility remains unchanged. Large-scale gradients of phase-shifting material leads to a lateral shift of the pattern, while the intensity remains unchanged [6]. And small-scale thickness variations of a phase-shifting material destroys the pattern contrast and periodicity, while the intensity again remains unchanged. This constitutes the dark-field signal [9].

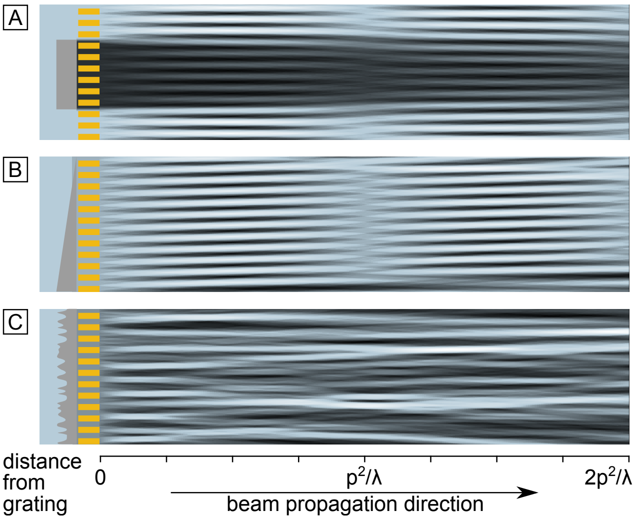

Figure 2.4: Influence of the different contrast mechanisms on the Talbot carpet of a $\pi/2$-phase-shifting grating. **A**, a purely attenuating material reduces overall intensity. **B**, a wedge of purely phase-shifting material induces a lateral shift of the pattern. **C**, a purely phase-shifting material with thickness variations on very small length scales partly destroys the periodicity and contrast of the intensity pattern. Talbot carpets are slightly smoothed. Figure color-adapted from [65].

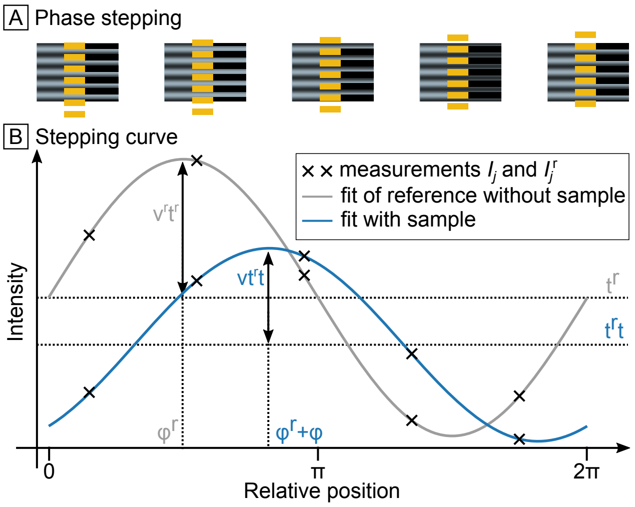

Figure 2.5: Phase stepping and stepping curve. **A**, phase stepping. By taking multiple exposures with varying relative positions of analyzer grating and intensity pattern, the pattern characteristics can be obtained without resolving it directly. **B**, influence of the different contrast mechanisms on the stepping curve. Transmission t, visibility reduction v and differential phase shift φ are obtained by performing the phase stepping procedure without and with the sample in the beam path.

By observing the changes in the intensity pattern due to a sample, information about its attenuation, phase-shift and dark-field signals can be obtained.

Analyzer grating and stepping

Typical flat-panel detectors (and most other X-ray detectors) have pixel sizes in the order of hundreds of µm, which is by far too large to resolve the intensity pattern directly. This can be solved with an absorbing analyzer grating G_2 which is placed directly in front of the detector [6]. Its period needs to match the period of the intensity pattern. By taking multiple exposures with varying relative positions of analyzer grating and intensity pattern, denoted by index j, a so-called stepping curve is obtained at each pixel, as shown in fig. 2.5 [7]. This procedure only works because of the periodicity of the intensity pattern and the analyzer grating, and allows to obtain information about the pattern characteristics mean intensity, phase and visibility in one pixel without resolving the pattern directly.

The stepping is typically performed once for reference without a sample in the beam path (denoted with superscript r) and once with the sample in the beam path. The measured intensities can be modelled as

$$I_j^{\mathrm{r}} = t^{\mathrm{r}}(1 + v^{\mathrm{r}} \cos(\varphi^{\mathrm{r}} + \phi_j)) \tag{2.2}$$

for the reference scan and

$$I_j = t^{\mathrm{r}} t (1 + v^{\mathrm{r}} v \cos(\varphi^{\mathrm{r}} + \phi_j + \varphi)) \tag{2.3}$$

for the sample scan [9], where the stepping is performed by varying the phase ϕ_j. The reference intensity t^{r}, reference visibility v^{r} and reference phase φ^{r}, and sample properties transmission t, relative visibility reduction v and differential phase shift φ are obtained with a least squares fit of the reference and sample scans [54]. The attenuation A and dark-field signal D are then calculated via

$$A = -\ln(t) \quad \text{and} \tag{2.4}$$

$$D = -\ln(v)\ . \tag{2.5}$$

The phase image from the differential phase φ is so far not used for clinical evaluation.

Dark-field imaging with clinical X-ray equipment

Clinical X-ray equipment comes with challenges for the detection of the dark-field contrast mechanism.

First, clinical sources have focal spot sizes in the mm range and thus have insufficient spatial coherence, which leads to many different Talbot carpets shifted laterally and overlapping, such that no resulting contrast can be measured at all. This can be counteracted by placing a absorption grating close to the source [8]. This source grating G_0 splits the large incoherent source into many small line sources, mutually incoherent but each with sufficient spatial coherence. By a thoughtful choice of the grating parameters, each small line source generates a congruent intensity pattern at the measured distance, i.e. the individual Talbot carpets of the line sources add up constructively. Such a three-grating system is called a Talbot-Lau interferometer.

Second, clinical systems do not feature a parallel beam, but use a cone-beam geometry. This leads to magnification and different propagation distances of the Talbot carpets. This can be accounted for by adapting the grating periods [66].
Third, clinical sources have wide polychromatic spectra. The dependence of the Talbot distances on the X-ray energy leads to a blurring of the Talbot carpet and reduced visibility. In turn, as the pattern visibility is measured at a fixed distance, the visibility depends on the X-ray spectrum at this point, which in turn depends on the spectral attenuation of the sample [67]. Dark-field and attenuation signals are thereby not independent any more. More details on this effect and its correction at our setup are part of chapter 3.

Dark-field imaging for clinical application

For most clinical applications relatively high X-ray energies in the range of 40 keV to 100 keV are necessary. Even though all above considerations are still valid, high X-ray energies make it harder to manufacture suitable gratings. These have to have small periods to keep the Talbot distances at practical levels and high structures to ensure sufficient absorption.
Additionally, clinical applications often require a large field of view, e.g. to image a whole thorax. As appropriate gratings with these large areas are currently not available, the clinical dark-field chest radiography system uses a scanning acquisition scheme [33, 54].
Finally, the higher X-ray energies in combination with the large exposed sample volume close to the detector leads to a relatively high amount of scattered photons, leading to artifacts in the dark-field and attenuation radiographs. More details on this effect and its correction at our setup are part of chapter 3.

2.2.3 The clinical dark-field chest radiography system

The clinical dark-field chest radiography system was built in a collaborative effort. Its design considerations and system specifications [53], image reconstruction algorithms [54], and dosimetry and patient exposure control [68] are described in detail in other works. Here, only a short overview will be given. For further details, please refer to the publications mentioned above and in the introduction.

System overview

An overview of the dark-field chest radiography system is shown in fig. 2.6. It is implemented as a conventional X-ray system in combination with a Talbot-Lau interferometer with three gratings G_0, G_1, and G_2.
The interferometer parameters are listed in table 2.1. All gratings are bent cylindrically with their distance from the source as bending radius, to ensure their correct alignment with respect to the beam path also in outer parts of the grating area [69]. Since the production of a grating large enough to cover the whole field of view is currently not possible, we use a scanning acquisition mode [27, 28]. The total grating area of the analyzer grating is about 6.5 cm × 42 cm, which was achieved by stitching it from 6 smaller tiles of 6.5 cm × 7 cm each. The other gratings are one single piece. By slightly detuning the interferometer, moiré fringes are generated in the detector plane, meaning that different interferometer positions relative to a pixel result in different relative positions of analyzer grating and intensity pattern. Thus, a stepping curve can be obtained for each pixel by taking multiple exposures while scanning the interferometer over it.

	G_0	G_1	G_2
distance from source (cm)	30	102	241
period (µm)	7.7	10.1	14.8
height (µm)	250	9.2	250
material	Au	Au	Au
substrate height (µm)	1000	200	1000
substrate material	graphite	glass	graphite
number of tiles	1	1	6

Table 2.1: Interferometer parameters

Typically, one full scan consists of 195 exposures. Example exposures showing the subject structures superimposed with the intensity pattern are displayed in fig. 2.6B. As each exposure is applied only on the grating area, this procedure results in 24 exposures per pixel, which are the measurements I_j of the stepping curve. From these, attenuation and dark-field radiographs can be reconstructed as described in section 2.2.2.
The tube (MRC 200 0508 ROT-GS 1003; Philips Medical Systems) has a tube filtration of 2.8 mm Al equivalent and is operated with large focal spot (0.8 as per IEC 60336) and 70 kV tube voltage at 30 s^{-1} pulse rate while the interferometer is scanned upwards, leading to the above mentioned 195 images per acquisition and an overall duration of one image acquisition of about 7 seconds.
The detector (PIXIUM 4343 F4; Trixell) is placed at a distance of 244 cm from the source and features a 600 µm CsI scintillator layer. It is operated with 3 × 3 binning, resulting in a pixel size of 444 µm × 444 µm.
The patient is leaning onto the patient contact plane (not shown in fig. 2.6 for simplicity). In pa orientation, the center of the patient is assumed to be 14 cm upstream of the patient contact plane, resulting in a distance of 34 cm between patient and detector. The effective pixel size at the patient position is hereby about 400 µm. In lat orientation, the distances are assumed to increase by 4 cm. The effective dose for the

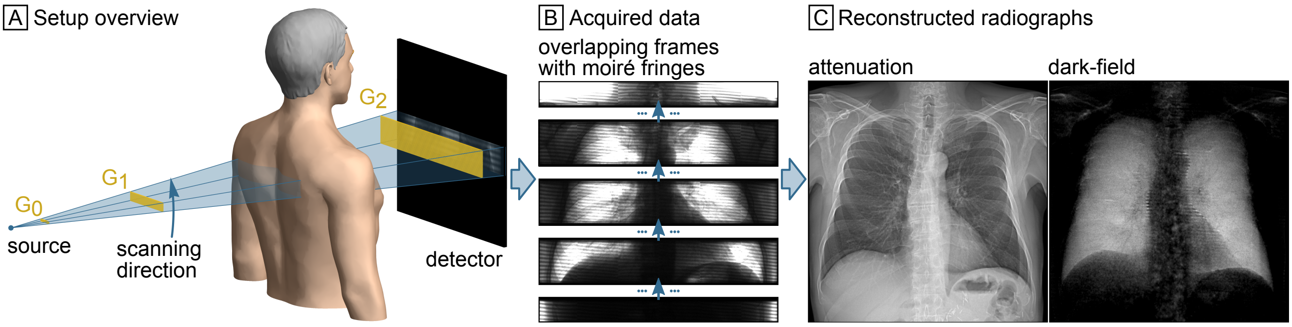

Figure 2.6: Overview of the dark-field chest radiography system. **A**, schematic view of the X-ray system. During one image acquisition, the interferometer with source grating G_0, phase grating G_1 and analyzer grating G_2 is scanned upwards over the field of view, while the source is operated at 30 Hz pulsed mode. **B**, exemplary exposures from the in total 195 acquired overlapping exposures showing the subject features superimposed with moiré fringes, which encode different relative positions of intensity pattern and analyzer grating. **C**, attenuation and dark-field radiograph, reconstructed from the exposures. Note that the radiographs shown here are already corrected with the results from chapter 3.

reference person is 35 µSv in pa orientation [70].

Implications of scanning image acquisition

The scanning image acquisition leads to several noteworthy implications: First, the reference pattern actually looks different for every exposure. To acount for this, we perform a series of reference scans (denoted by subscript i) to fit the reference parameters t_j^{r}, v_j^{r}, and φ_j^{r} separately for every exposure j. Our model intensities then are

$$I_j^{\mathrm{r}} = t_j^{\mathrm{r}}(1 + v_j^{\mathrm{r}} \cos(\varphi_j^{\mathrm{r}} + \phi_i)) \qquad (2.6)$$

for the reference scan and

$$I_j = t_j^{\mathrm{r}} t (1 + v_j^{\mathrm{r}} v \cos(\varphi_j^{\mathrm{r}} + \varphi)) \qquad (2.7)$$

for the sample scan.

The moving interferometer might also vibrate, both during and between exposures. These vibrations can also be accounted for by including them in the model. See [54] for further details.

Additionally, the overall acquisition time of 7 seconds is much longer than in conventional radiography. Holding breath for this duration is possible, but can be difficult especially for patients with lung diseases. The heart beat cannot be stopped during this time, and other movement, such as the diaphragm moving despite breath hold or a slight swaying of the patient, cannot be avoided completely. However, it is possible to reduce the ensuing artifacts by detecting affected exposures and image areas and using only the exposures without movement [71].

At the same time, the smaller grating area comes with benefits: The small grating area is cheaper and easier to fabricate, and the relatively little exposed volume per frame reduces the generated scatter (see chapter 3).

The future will show whether a simplified and faster image acquisition process will justify the increased fabrication effort and higher scatter intensities from larger gratings. Stay tuned!

2.3 COPD and the Human Lung

2.3.1 Healthy lungs

Unless indicated otherwise, this section is based on [72]. The human lung is responsible for gas exchange in the metabolism. Its main purpose is to release CO_2 from blood into the ambient air and at the same time take oxygen from the ambient air into the blood. This interchange happens in the capillary network surrounding the alveoli, small air cavities with a diameter between 75 µm and 300 µm, which are inflated and deflated with ambient air during breathing.

The total air volume in a adult lung is about 5 L to 6 L. The left and right lungs consist of two and three lobes, respectively. The airflow is through a hierarchical system of bronchi, which branch from the trachea up to 16 generations down to the small terminal bronchioles with less than 1 mm diameter. These in turn branch again into respiratory bronchioles, which already have alveoli on them and take part in the gas exchange, but also branch for up to 5 more generations until the final saccus alveolaris, groups of alveoli.

In total, a human lung has hundreds of millions of alveoli. Ochs et al. [73] counted the alveoli in six human lungs and found that the alveolar number increases with lung volume, suggesting a constant alveolar density of about 170 alveoli/mm^3 of lung tissue. Their exact shape is not known, but they are mostly assumed to be somewhere between angular and spherical [74].

With its many interfaces of air and tissue due to its alveolar structure, healthy lung tissue causes a strong dark-field signal. A quantitative analysis of healthy lungs is part of chapter 4.

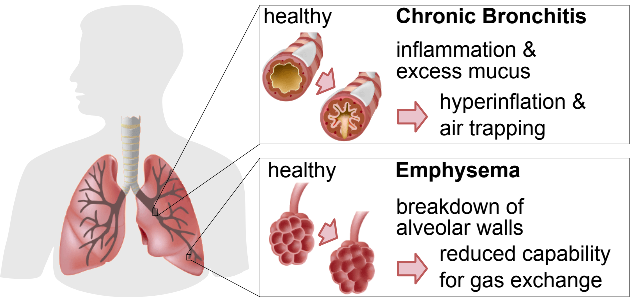
healthy
Chronic Bronchitis
inflammation &
excess mucus
hyperinflation &
air trapping
healthy
Emphysema
breakdown of
alveolar walls
reduced capability
for gas exchange

Figure 2.7: Influence of COPD on the human lung. Illustrations from [75], information from [76].

2.3.2 COPD lungs

The effect of COPD on the human lung is displayed in fig. 2.7. The Global Initiative for Chronic Obstructive Lung Disease defines COPD as "a heterogeneous lung condition characterized by chronic respiratory symptoms (dyspnea, cough, sputum production, exacerbations) due to abnormalities of the airways (bronchitis, bronchiolitis) and/or alveoli (emphysema) that cause persistent, often progressive, airflow obstruction" [77]. A person with COPD can have chronic bronchitis, emphysema, or a combination of both conditions. The amount of each of these conditions differs from person to person [76].

For dark-field chest radiography, especially the emphysema manifestation of COPD is of interest. Emphysema is a lung condition "characterized by abnormal, permanent enlargement of the air spaces distal to the terminal bronchiole, accompanied by destruction of their walls" [78].

This means that the emphysema destroys the alveolar structure of the lung, leading to larger air spaces and reducing its gas exchange capabilities. Due to less air-tissue interfaces, the dark-field signal is expected to decrease with emphysema severity. This was previously shown in a mouse model [20]. For humans, first results showed that emphysema can be diagnosed with dark-field chest radiography [33]. A further analysis of emphysema assessment with dark-field chest radiography is part of chapter 4.

Chapter 3

Image Artifacts

3.1 Motivation

The diagnostic value of dark-field radiography is currently investigated in many research groups and many applications [79]. In our group, we investigate the use of dark-field chest radiography. Initial results from currently ongoing patient studies (see also chapter 4) show that dark-field chest radiographs allow the detection and quantification of pulmonary emphysema [33, 80] and the assessment of Covid-19 pneumonia [81]. The obtained radiographs are evaluated both qualitatively in reader studies by radiologists [33, 81, 82], and quantitativly [80, 83]. Especially the quantitative evaluation is of great interest, as it is potentially less work-intensive and yields objective results. For both qualitative and quantitative analyses, it is necessary to provide correct radiographs. However, the quantitative accuracy is not granted, as the interferometer used for detecting the dark-field signal is a very sensitive instrument. Therefore, there are a number of corrections performed on the dark-field and attenuation radiographs before they are evaluated. Section 3.3.7 gives an overview of the whole processing pipeline. The corrections for detector crosstalk, for scatter from the analyzer grating, for sample scatter, and for beam hardening induced dark-field signal were developed in this thesis. They will be explained, investigated and evaluated in detail in the following chapter.
Parts of the sections about detector crosstalk, scatter from the analyzer grating, and sample scatter have been previously published in [84]. This thesis here covers these published contents and shows more details and further in-depth analyses.

Scatter and crosstalk

The mean and visibility of the intensity pattern (see section 2.2.2) used for dark-field imaging are also influenced by scatter and crosstalk. In this work, this refers to any interactions of photons with matter, where the photon still reaches the detector but at a different location than if it did not undergo any interaction.

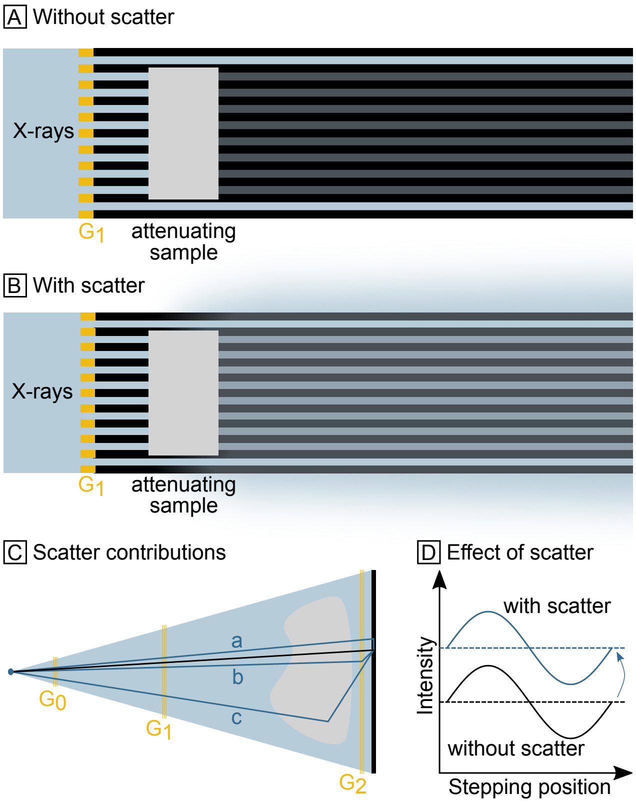

Figure 3.1: The effect of scatter and crosstalk in dark-field radiography. **A**, the grating G_1 imprints an intensity pattern onto the X-ray beam, wich is shown as a G_1 shadow for simplicity. The pattern mean and visibility encode attenuation and dark-field signal, respectively. **B**, scatter adds an offset to the intensity pattern, increasing its mean and thereby decreasing its contrast. **C**, schematic top view of the dark-field chest radiography system. The black line depicts the path of an exemplary unscattered photon, whereas blue lines depict exemplary paths of photons subject to scatter or crosstalk, which are measured in the same position as the unscattered photon. The three main contributions of related artifacts are detector crosstalk (path a), scatter from the analyzer grating G_2 (path b) and scatter from the sample (path c). **D**, scatter adds an offset to the stepping curve. Since both attenuation and dark-field signals depend on the mean of the stepping curve, scatter leads to artifacts in the respective images.

These effects include scattering and fluorescence of X-rays in the setup, and optical crosstalk after scintillation in the detector. Furthermore, these effects also include photons reaching the detector through incoherent scattering in the sample as well as coherent scattering with larger angles. Note that the sample's coherent ultra-small angle scattering is due to microscopic material interfaces and generates the wanted dark-field signal. Coherent scattering at larger angles – e.g. corresponding to those used in SAXS experiments [55, 56] – is due to much smaller structures on a nanometer scale such as atoms and molecules, and therefore an unwanted effect (see section 2.2.1). Scatter created upstream of the sample can be neglected, since only photons that actually reach the detector cause artifacts.

Unlike primary radiation, the detector signal generated by scatter barely depends on the relative position of analyzer grating and intensity pattern (fig. 3.1). Crosstalk intensities depend mainly on the intensity of neighbouring pixels. Thus, scatter and crosstalk lead to an approximately constant offset on the whole stepping curve. The increased mean value of the stepping curve leads to artifacts in the attenuation image that are well known from conventional radiography.

The visibility of the stepping curve depends on the mean intensity as well. Therefore, scatter and crosstalk also cause artifacts in the dark-field radiograph which impair image appearance for qualitative analysis and prevent a quantitative analysis of the dark-field signal.

The effect of scatter from the sample in grating-based imaging has previously been studied in [85] for smaller setups in the context of mammography. In the current clinical setup for chest imaging, the effect of scatter is more prominent due to the larger exposed volume, the higher photon energy, and a higher total attenuation of the sample. Scatter from the analyzer grating was simulated by Vignero et al. [86], but only its effect on the setup's reference visibility was investigated. To the best of our knowledge, the effect of neither detector crosstalk nor scatter from the analyzer grating in dark-field radiographs have been investigated before.

Here, we propose methods to estimate scatter and crosstalk intensities for a correction of dark-field and attenuation images. We perform Monte-Carlo simulations for an in-depth analysis of the estimated scatter intensities and the underlying processes, and for validation of the developed correction methods. Furthermore, we validate the corrections with a purely attenuating water phantom and a more complex phantom with attenuating and dark-field generating components. Finally, we demonstrate the effect of detector crosstalk, scatter from the analyzer grating and scatter from the sample and their correction on dark-field radiographs of a participant from the current patient study.

Beam hardening

Beam hardening is a very well known effect in X-ray imaging [87]. It occurs whenever X-rays from a polychromatic spectrum are attenuated in a sample. As the X-ray attenuation depends on X-ray energy – lower energies are attenuated more – the X-ray spectrum becomes harder with sample thickness. In the attenuation contrast, this leads to a non-linear relationship between sample thickness and measured attenuation [87]. Corresponding artifacts in radiographs are often neglected as these are non-quantitative anyway. For CT imaging, where artifacts are more prominent and quantitativeness is important, there are a number of correction algorithms [88–90].

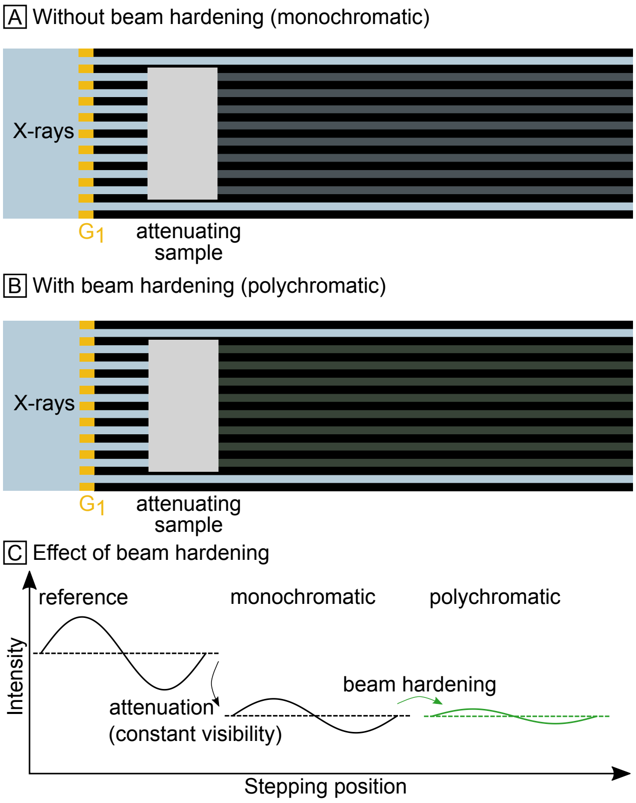

Figure 3.2: The effect of beam hardening in dark-field radiography. **A**, the grating G_1 imprints an intensity pattern onto the X-ray beam, wich is shown as a G_1 shadow for simplicity. The reduction in mean and visibility encode attenuation and dark-field signal, respectively. With a monochromatic X-ray beam, the beam spectrum does not change with the sample. **B**, a polychromatic beam and spectrally differential attenuation causes beam hardening, i.e. a change in X-ray spectrum. **C**, as the overall visibility depends on the X-ray spectrum, a lower visibility is observed behind attenuating objects. It is falsely interpreted as a dark-field signal, leading to artifacts in the dark-field radiograph.

In dark-field radiography, a harder X-ray spectrum also leads to a change in the visibility of the intensity pattern, which is then falsely interpreted as dark-field signal (fig. 3.2). This beam hardening induced dark-field signal has been previously investigated in a number of works [67, 91–93]. The overall impact of beam hardening depends on the sample attenuation, the used X-ray spectrum, and the setup.

Here, we investigate the effect of beam hardening on dark-field radiographs obtained with our dark-field chest radiography system and refine and extend a method using calibration measurements [29] to correct for it. We validate the correction with a

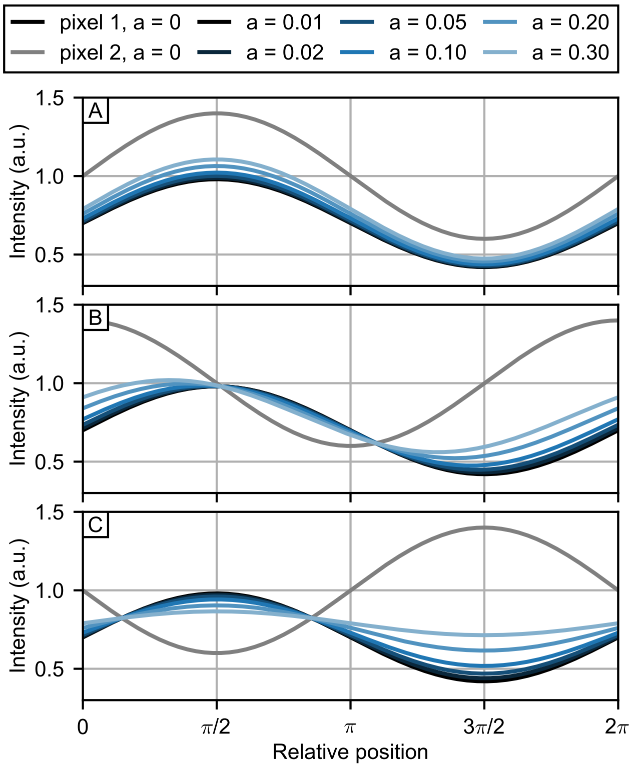

Figure 3.3: Exemplary stepping curves after crosstalk between two pixels with the same visibility $v_1 = v_2 = 40\%$ for different crosstalk factors a. The colored lines represent stepping curves I'_1 of pixel 1 after crosstalk with pixel 2. **A**, same phase. **B**, $\pi/2$ relative phase difference. **C**, π phase difference. Note that both pixels have similar mean values ($t_1 = 0.7$, $t_2 = 1$) for an easier visualization. In real samples, the difference in attenuation of neighbouring pixels can be much higher, leading to stronger crosstalk effects.

purely attenuating water phantom and a more complex phantom with attenuating and dark-field generating components. Finally, we demonstrate the impact of beam hardening and its correction on dark-field radiographs of a participant from the current patient study.

3.2 Theory

3.2.1 Detector crosstalk

In the scope of this thesis, the term detector crosstalk is used for all processes that lead to a measured intensity remote from the incident photon, mainly due to the spread of optical photons originating from scintillation [94]. This well-known effect is characterized by a point spread function, leading to a loss of spatial resolution in the recorded exposures and consequently also in the reconstructed attenuation and dark-field images. In dark-field imaging there is additionally another effect: Wherever the phase of the moiré fringes in pixels in close vicinity differs, crosstalk also decreases the measured contrast of the stepping curve. This causes a spurious, crosstalk-induced dark-field signal the same way X-ray scatter does.

Here, we evaluate theoretically when and how detector crosstalk actually impacts the obtained radiographs. This behaviour is different from scatter because detector crosstalk happens after the moiré fringes are generated on the detector, and the spread is local enough that the crosstalk intensities have a strong dependency on the phase of the moiré fringe of the pixel they are generated in. Note that the following calculations were derived in close collaboration with Dr. Thomas Koehler (Philips Research, Hamburg).

To get an estimate of detector crosstalk, we regard the measured intensity in a pixel I' in a simplified system with only two pixels, where crosstalk transfers a portion a of the intensity I_2 at pixel 2 to pixel 1 and vice versa (fig. 3.3):

$$I'_{1j} = (1-a) I_{1j} + a I_{2j} \,, \tag{3.1}$$

where the $'$ denotes crosstalk-affected parameters. Using eq. (2.7) and assuming the same reference intensity t^{r}, reference visibility v^{r}, and stepping phase ϕ_j in both pixels, this becomes

$$\begin{aligned} I'_{1j} = {} & (1-a) t^{\mathrm{r}} t_1 (1 + v^{\mathrm{r}} v_1 \cos(\varphi^{\mathrm{r}}_{1j} + \varphi_1 + \phi_j)) \\ & + a\, t^{\mathrm{r}} t_2 (1 + v^{\mathrm{r}} v_2 \cos(\varphi^{\mathrm{r}}_{2j} + \varphi_2 + \phi_j)) \,. \end{aligned} \tag{3.2}$$

With the calculus rules for sums of cosines, this can be refactored to show the obtained parameters t'_1, v'_1 and φ'_1 that are obtained if detector crosstalk is ignored during phase retrieval:

$$I'_{1j} = t^{\mathrm{r}} t'_1 (1 + v^{\mathrm{r}} v'_1 \cos(\varphi'_1 + \phi_j)) \tag{3.3}$$

with

$$t'_1 = (1-a) t_1 + a t_2 \tag{3.4}$$

$$v'_1 = \frac{\sqrt{\begin{aligned} & ((1-a) t_1 v_1)^2 + (a t_2 v_2)^2 \\ & + 2a(1-a) t_1 t_2 v_1 v_2 \cos(\varphi^{\mathrm{r}}_1 + \varphi_1 - \varphi^{\mathrm{r}}_2 - \varphi_2) \end{aligned}}}{(1-a) t_1 + a t_2} \tag{3.5}$$

$$\varphi'_1 = \arctan \left(\frac{\begin{aligned} & (1-a) t_1 v_1 \sin(\varphi^{\mathrm{r}}_1 + \varphi_1) \\ & \quad + a t_2 v_2 \sin(\varphi^{\mathrm{r}}_2 + \varphi_2) \end{aligned}}{\begin{aligned} & (1-a) t_1 v_1 \cos(\varphi^{\mathrm{r}}_1 + \varphi_1) \\ & \quad + a t_2 v_2 \cos(\varphi^{\mathrm{r}}_2 + \varphi_2) \end{aligned}} \right) . \tag{3.6}$$

The effect in the measured transmission t'_1 is in all cases simply a mix of the true transmission values of the two pixels, i.e. a loss of spatial resolution. However, the effect on the visibility reduction is quite complex, and depends heavily on the difference in phase and attenuation between the two pixels (fig. 3.4). To illustrate this, the following provides a more detailed analysis of special cases.

In the case where the measured fringe phase is the same in both pixels (fig. 3.3A), i.e. $\varphi^{\mathrm{r}}_1 + \varphi_1 = \varphi^{\mathrm{r}}_2 + \varphi_2$,

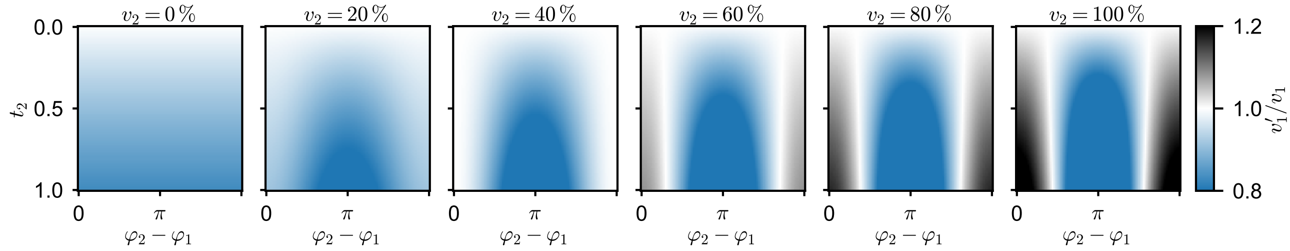

Figure 3.4: Effect of crosstalk with a factor of $a = 0.02$ from pixel 2 on the apparent visibility of pixel 1 with original transmission $t_1 = 0.1$ and original visibility $v_1 = 40\%$. The visibility is affected more the higher the mean intensity t_2 of pixel 2, the higher the visibility v_2 of pixel 2, and the higher the absolute difference in phase of the two pixels. Note that φ_i here denotes the effective pixels phase, $\varphi_\mathrm{i}^\mathrm{r} + \varphi_\mathrm{i}$.

the addition from the second pixel is in sync with the first pixel. The visibility reduction is then

$$v_1' = \frac{(1-a)t_1v_1 + at_2v_2}{(1-a)t_1 + at_2}\,. \tag{3.7}$$

This formula is a mix of the two visibilities, weighted by their mean intensities and of course by the detector crosstalk factor a.

In the case where the measured fringe phase of the two pixels is opposite (fig. 3.3C), i.e. $\varphi_1^\mathrm{r} + \varphi_1 = \varphi_2^\mathrm{r} + \varphi_2 + \pi$, the addition from the second pixel is in opposite phase to the pixel. In this case, the apparent visibility reduction v_1' is always smaller than the actual visibility reduction v_1:

$$v_1' = \frac{(1-a)t_1v_1 - at_2v_2}{(1-a)t_1 + at_2}\,. \tag{3.8}$$

Generally, the effect on the visibility is not simply a mix of the two visibilities from pixel 1 and 2. The relative phase difference determines how the two stepping curves match, and the difference in mean intensity, i.e. their attenuation, determines the overall impact. Higher differences in attenuation mean a higher detector crosstalk effect. In conclusion, the effect of detector crosstalk is not only a loss of spatial resolution, but an artificial dark-field signal.

In a real detector, there are of course many pixels interacting via crosstalk with each other, with, depending on the reference phase pattern and the sample, different relative phase of their stepping curves und consequently different phase of the moiré fringes on the detector. Assuming that the sample has very little phase signal itself, the overall effect of detector crosstalk is worse with a high frequent reference phase and at locations of discontinuous reference phase, e.g. at stiching lines of grating tiles.

Depending on the attenuation of the sample, the detector is exposed with varying intensity. The worst detector crosstalk impact is expected for image areas of low primary intensity that are close to edges of attenuation, being contaminated by detector crosstalk from closeby areas of high intensity.

3.2.2 Scatter

Scatter occurs in both the reference and the sample scan, and leads to additional intensity at the detector. This scatter intensity generally depends on the exposed volume and the gratings. However, to get an approximate estimation of the impact of scatter on dark-field and attenuation images, we consider a simplified case, where scatter is uniform enough so that the scatter intensity does not depend on the exposure index j. Further, we assume that reference intensity t^r and visibility v^r are also independent of exposure index j.

The measured intensities I_j then include the primary intensities according to eqs. (2.6) and (2.7) and an additive scatter intensity I_s. This leads to

$$I_j^\mathrm{r} = t^\mathrm{r}(1 + v^\mathrm{r}\cos(\varphi_j^\mathrm{r})) + I_\mathrm{s}^\mathrm{r} \tag{3.9}$$

for the reference scan and

$$I_j = t^\mathrm{r}t(1 + v^\mathrm{r}v\cos(\varphi_j^\mathrm{r} + \varphi)) + I_\mathrm{s} \tag{3.10}$$

for the sample scan. Even in this simplified case, I_s cannot be included as a variable in the least squares fit, since the effect of scatter and attenuation cannot be separated. For a correction of the ensuing artifacts, it is rather necessary to estimate the scatter intensities and subtract them from the measured ones before the final signal retrieval.

To estimate the impact of scatter when it is ignored in the phase retrieval, eq. (3.9) can be factorized to show the scatter-affected reference intensity $t^{\mathrm{r}\prime}$ and reference visibility $v^{\mathrm{r}\prime}$. These are obtained when the measured intensities from the reference scan in eq. (3.9) are fitted with the model in eq. (2.6):

$$I_j^\mathrm{r} = t^{\mathrm{r}\prime}(1 + v^{\mathrm{r}\prime}\cos(\varphi_j^\mathrm{r} + \varphi)) \tag{3.11}$$

with

$$t^{\mathrm{r}\prime} = t^\mathrm{r}\,(1 + s^\mathrm{r}) \quad \text{and} \tag{3.12}$$

$$v^{\mathrm{r}\prime} = v^\mathrm{r}\,(1 + s^\mathrm{r})^{-1}\,, \tag{3.13}$$

where $s^\mathrm{r} = I_\mathrm{s}^\mathrm{r}/t^\mathrm{r}$ is the ratio of scatter to primary intensity in the reference scan. These scatter-affected reference values are further used to obtain scatter-affected sample transmission t' and relative visibility reduction v' from the measured intensities in the sample scan, by fitting the measured intensity in eq. (3.10) using the model in eq. (2.7):

$$I_j = t^{\mathrm{r}\prime} t' (1 + v^{\mathrm{r}\prime} v' \cos(\varphi_j^{\mathrm{r}} + \varphi)) \tag{3.14}$$

with

$$t' = t \, \frac{1+s}{1+s^{\mathrm{r}}} \tag{3.15}$$

and

$$v' = v \, \frac{1+s^{\mathrm{r}}}{1+s} \,, \tag{3.16}$$

where $s = I_{\mathrm{s}} / t^{\mathrm{r}} t$ is the ratio of scatter to primary intensity in the sample scan.

We find that scatter leads to an offset S in the corresponding attenuation and dark-field images:

$$A' = -\ln(t') = -\ln(t) - \ln\left(\frac{1+s}{1+s^{\mathrm{r}}}\right) = A - S \tag{3.17}$$

and

$$D' = -\ln(v') = -\ln(v) - \ln\left(\frac{1+s^{\mathrm{r}}}{1+s}\right) = D + S \,, \tag{3.18}$$

where

$$S := \ln\left(\frac{1+s}{1+s^{\mathrm{r}}}\right) \,. \tag{3.19}$$

The absolute offset in the dark-field signal is the same as for the attenuation signal, albeit with an opposite sign. Its value depends only on the scatter-to-primary ratio in reference and sample scan. Since in most practical cases, $s > s^{\mathrm{r}}$ and $S > 0$, the attenuation is underestimated while the dark-field signal is overestimated.

3.2.3 Beam hardening

The X-ray wavelength and thus its energy influence the Talbot carpet and the corresponding Talbot distances, i.e. the distances from the phase grating in which the pattern visibility is highest (see section 2.2.2 and eq. (2.1)). It can be shown that no interference effects occur between the fields of photons with different energies, i.e. we can regard the Talbot carpets of the different photon energies individually and sum over them according to the spectrum [65].

The distance between phase grating G_1 and analyzer grating G_2 is adjusted with regard to the used spectrum and gratings. It is then fixed and not changed during any measurements. As the Talbot distance of individual energies differ, different photon energies show different visibilities at this fixed distance. This is called the visibility spectrum. With perfect gratings this visibility spectrum would be a simple sinusoidal in dependence of X-ray wavelength, and thus $\sin(1/E)$ in dependence of X-ray energy E. For real gratings, the sinusoidal is additionally multiplied with the energy-dependent grating performance. An exemplary visibility spectrum that was simulated in another work [98] for the dark-field chest radiography system is shown in fig. 3.5C.

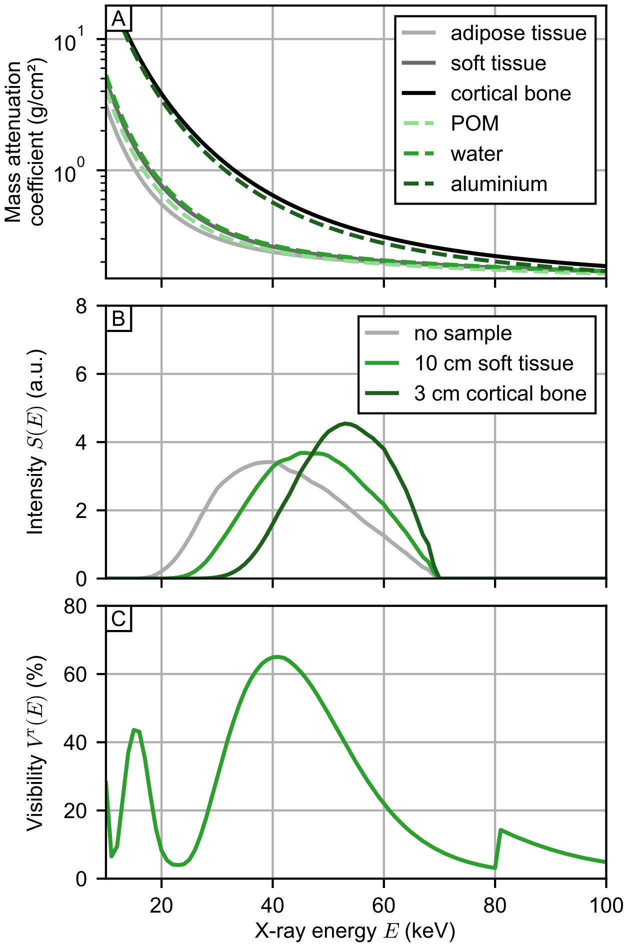

Figure 3.5: Theory behind beam hardening in dark-field radiography. **A**, mass attenuation coefficients for different materials in the thorax and for materials used in calibration phantoms. Material compositions from [95], corresponding attenuation coefficients from [96]. **B**, estimated initial spectrum used at the dark-field chest radiography system (data from [97]) and example spectra of the beam after passing a sample. **C**, estimated visibility spectrum of the dark-field chest radiography system. Data courtesy of Manuela Frank [98]. Note that the data in **B** and **C** are only estimated to illustrate the effects and may not actually display the spectra at the dark-field chest radiography system.

The overall measured visibility V is the weighted mean over the visibility spectrum $V(E)$ and the spectrum $S(E)$ of the X-ray beam.

$$V = \int_E S(E) V(E) \, \mathrm{d}E \tag{3.20}$$

In a polychromatic beam, the X-ray spectrum $S(E)$ changes due to spectrally different attenuation of X-rays in the sample. Figure 3.5A shows the mass attenuation coefficient for different materials in the thorax, and fig. 3.5B the initial X-ray spectrum $S^{\mathrm{r}}(E)$ and exemplary resulting spectra $S^{\mathrm{s}}(E)$ after a sample.

To estimate the effect of beam hardening, we consider a simplified case where the reference visibility is independent of exposure j. Then, the measured dark-field signal D' is the logarithm of the ratio of sample to reference visibility:

$$D' = -\ln\left(\frac{V^{\mathrm{s}}}{V^{\mathrm{r}}}\right) \tag{3.21}$$

Additionally, we assume that the decrease of visibility due to the micro-structure of the sample does not depend on X-ray energy:

$$V^{\mathrm{s}}(E) = v(E) \cdot V^{\mathrm{r}}(E) \approx v \cdot V^{\mathrm{r}}(E). \tag{3.22}$$

This allows to separate the true dark-field signal due to a reduction of the visibility spectrum D and the beam hardening induced dark-field D_{bh}:

$$\begin{aligned} D' &= -\ln\left(\frac{\int_E S^{\mathrm{s}}(E)\, v\, V^{\mathrm{r}}(E)\,\mathrm{d}E}{\int_E S^{\mathrm{r}}(E)V^{\mathrm{r}}(E)\,\mathrm{d}E}\right) && (3.23)\\ &= -\ln(v) - \ln\left(\frac{\int_E S^{\mathrm{s}}(E)V^{\mathrm{r}}(E)\,\mathrm{d}E}{\int_E S^{\mathrm{r}}(E)V^{\mathrm{r}}(E)\,\mathrm{d}E}\right) && (3.24)\\ &=: D + D_{\mathrm{bh}} && (3.25) \end{aligned}$$

with

$$D_{\mathrm{bh}} = -\ln\left(\frac{\int_E S^{\mathrm{s}}(E)V^{\mathrm{r}}(E)\,\mathrm{d}E}{\int_E S^{\mathrm{r}}(E)V^{\mathrm{r}}(E)\,\mathrm{d}E}\right). \tag{3.26}$$

Thus, the attenuation in the sample leads via a change in spectrum to an additional dark-field signal D_{bh}.

Note that attenuation and dark-field contrast are not independent any more. If we did not correct for that, the beam hardening induced dark-field signal would be falsely interpreted as a true dark-field signal, corrupting both image appearance for qualitative evaluations and quantitative values.

The assumption of an energy-independent decrease in visibility by the sample in eq. (3.22) is not actually true. This means that the true dark-field D cannot as easily be separated from the beam hardening induced dark-field D_{bh}, and that another effect called visibility hardening occurs. Fabio de Marco investigated this during his PhD at another experimental dark-field imaging setup [65, 92]. The analysis and correction of these effects at the dark-field chest radiography system will hopefully be part of future PhD theses at the chair.

3.3 Methods

The previously described artifacts are characterized by either measuring them directly (beam hardening), modelling them and fitting the model to measurements (detector crosstalk), or simulating them and verifying the results from the simulation with measurements (grating and sample scatter). These characterizations then allow the development of correction algorithms.

3.3.1 Monte-Carlo simulations

For all Monte-Carlo simulations in this work, Geant4 (version 10.06.p03), was used. Geant4 is a C++-based toolkit originally developed at CERN [99–102] for Monte-Carlo simulations of particles passing through matter. Geant4 was made to simulate particles and their interactions, and is thus very appropriate to simulate scatter. However, including optical photons and wave effects requires special care [103, 104].

Note that coherent scattering in Geant4 refers to the scattering of photons at the electrons in the material's atoms, including the atomic form factors [105, 106]. This does not include effects from the distribution of electrons on a larger scale such as in molecules, particles, or material micro-structures. Due to the particle nature of photons in Geant4, interference effects from photons scattered at different electrons (see section 2.2.1) cannot be simulated. Therefore, corresponding dark-field and phase-contrast effects are hard to include in the simulation [107]. Even though this is an active area of further development of Geant4, both optical photons and wave properties of X-rays were left out of the simulations in this work for simplicity.

The toolkit has predefined classes for particle generation, particle interactions and transport through the world, and tracking of these particles. The user needs to specify the wanted setup, including the materials and the particle properties, and to use a suitable, often predefined way of yielding the wanted information from the simulation.

Geant4 is installed on the Chair's server `quito`. All code is available on the Chair's data storage[1]. The code for simulations with CT scans as samples is also available on the Chair's gitlab repository[2].

Implementation of the dark-field chest radiography system

Figure 3.6 shows an exemplary screenshot of the implemented dark-field chest radiography system. The X-ray source is implemented using the

---

[1] on `\data\DPC\local_setups\patscanner\2020_Geant4_Simulations`

[2] `https://gitlab.lrz.de/e17/geant-4-pat-scanner`

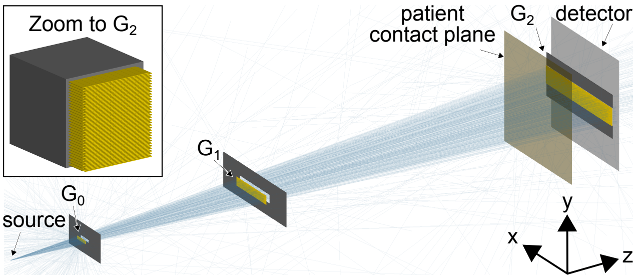

Figure 3.6: The dark-field chest radiography system implemented in Geant4. The blue lines depict the paths of 10000 exemplary simulated photons. The source is located at the origin of the coordinate system.

`G4GeneralParticleSource` class to allow easy adaption of source size and angular distribution of emitted photons depending on the application. The initial spectrum of the X-rays is implemented according to [97] and is shown in fig. 3.5B. As the X-ray energies are comparably low for Geant4 applications, the `livermore` physics list is used for all simulations.

The gratings were implemented according to their specifications (see table 2.1). We included the bending of the gratings as well as their microscopic structure with grating lamellae of gold and photoresist in between. They were oriented such that the substrate faces the source and the gold lamellae face the detector. For the analyzer grating, even the auxiliary bridges due to the fabrication process [25], with a bridge fraction of 3 %, were implemented. The tungsten shieldings surrounding the gratings were also added.

The patient contact plane is made of 1 mm Kapton, 20 cm upstream of the detector. The detector consists of 0.6 mm Caesium-Iodine doted with Thallium (CsI-Tl), with a filling factor of 75 % according to personal communication with Klaus-Juergen Engel from Philips Research. We added an additional layer of carbon fiber material (0.5 mm CFRP) directly upstream on it and a layer of electronics (0.5 mm Si) directly downstream to represent the detector housing.

Implementation of information yield

The `G4AnalysisManager` tool is used to store the information during the simulation and write it to .csv files. This tool provides histograms that can be filled during the simulation. Two such histograms were used in this work: The first one records the energy deposited in the detector, i.e. the obtained images. The second one records the X-ray spectrum at different positions in the setup.

Detector images are recorded depending on the processes and their locations the photons undergo on their way from source to detector. To this end, whenever a photon undergoes any process besides transportation, the name of the volume this process is happening in is stored. The energy deposited in the detector by this photon is then added to the corresponding histogram. Thus, separate detector images are obtained for primary photons (processes besides transportation only within the detector) and all the materials present in the setup.

The grating G_0 and G_1 are each treated as one volume, while the grating G_2 is kept separated into grating substrate, grating photoresist and grating lamellae. Additionally, scattering at the air, at the tungsten plates, at the sample materials, and at the patient contact plane is recorded. The detector itself is not considered a scattering material, i.e. photons that are scattered only within the detector count as primary photons.

For the simulation of scatter from the analyzer grating (section 3.3.3), detector images are further separated for the different processes photoelectric effect (including subsequent fluorescence), coherent scattering, and incoherent scattering.

For the tracking of X-ray spectra, additional air sheets were added to the geometry. Whenever an X-ray passes such an air sheet in positive z-direction, i.e. travelling towards the detector (see fig. 3.6), one count is added to the corresponding energy bin in the spectrum histogram. Six different points in the geometry were selected: Just after the source ($z = 20$ cm), after the source grating G_0 ($z = 100$ cm), after the phase grating G_1 ($z = 110$ cm), after the sample ($z = 224$ cm), after the patient contact plane ($z = 240$ cm), and after the analyzer grating G_2 ($z = 243.5$ cm). The spectra are recorded as sum over the whole field of view, so there is no further spatial differentiation in x- and y-direction possible.

3.3.2 Detector crosstalk

Correction concept

To estimate and correct for detector crosstalk, we use a kernel-based method. To that end, we need to first find a kernel that describes the point-spread function of detector crosstalk, and then use that kernel to estimate and subtract the intensities due to detector crosstalk from the measured data.

The crosstalk intensity $\vec{I}_s$ can be calculated by a convolution of primary intensity $\vec{I}$ with a crosstalk kernel $\vec{k}$ [108]:

$$\vec{I}_s = \vec{I} * \vec{k}\,. \tag{3.27}$$

To model the crosstalk kernel $\vec{k}$, we assume that optical photons are isotropically scattered with a model according to a 2D-Beer-Lambert decay, expressed as

$$k(r) = \begin{cases} \alpha e^{-\beta r}/r^2 & r > 0 \\ 0 & r = 0\,, \end{cases} \tag{3.28}$$

where r denotes the distance from the point of impact of the incident photon. The parameters α and β describe the overall probability of scattering in the detector and the radial linear attenuation coefficient of the scattered photons, respectively. Photons scattered within one pixel ($r = 0$) are counted as primary intensity.

The measured intensity $\vec{I}'$ is the sum of primary intensity $\vec{I}$ and crosstalk intensity $\vec{I}_\mathrm{s}$:

$$\vec{I}' = \vec{I} + \vec{I}_\mathrm{s}\,. \tag{3.29}$$

Knowing the crosstalk kernel $\vec{k}$ and using eq. (3.27), the crosstalk intensity can be calculated from the measured intensity by

$$\vec{I}_\mathrm{s} = \vec{I}' - \vec{I} = \vec{I}' - \left(\vec{I}' * (1 + \vec{k})^{-1}\right)\,. \tag{3.30}$$

With the Neumann series,

$$\left(1 - \vec{k}\right)^{-1} = \sum_{n=0}^{\infty} \vec{k}^{*n}\,, \tag{3.31}$$

where ^{*n} denotes convolving n times, this can be expressed as

$$\vec{I}_\mathrm{s} = \vec{I}' - \left(\vec{I}' * \sum_{n=0}^{\infty} \left(-\vec{k}\right)^{*n}\right) \tag{3.32}$$

$$= \vec{I}' * \vec{k} - \vec{I}' * \vec{k}^{*2} + \vec{I}' * \vec{k}^{*3} - \ldots\,. \tag{3.33}$$

Measurements

To find the kernel parameters, measurements with a 2 mm tungsten plate placed directly in front of the detector, covering about half of it, were conducted (see fig. 3.7A). Since the tungsten plate absorbs all photons coming directly from the source (transmission for the used spectrum is about 4×10^{-7}), the intensity measured behind the tungsten plate is only due to detector crosstalk from the adjacent exposed area.

We performed a least-squares fit for the kernel parameters α and β. The cost function was the difference of the measured intensity behind the tungsten plate to the one estimated from the measured intensity with the current kernel parameters. We used all exposures of one full scan.

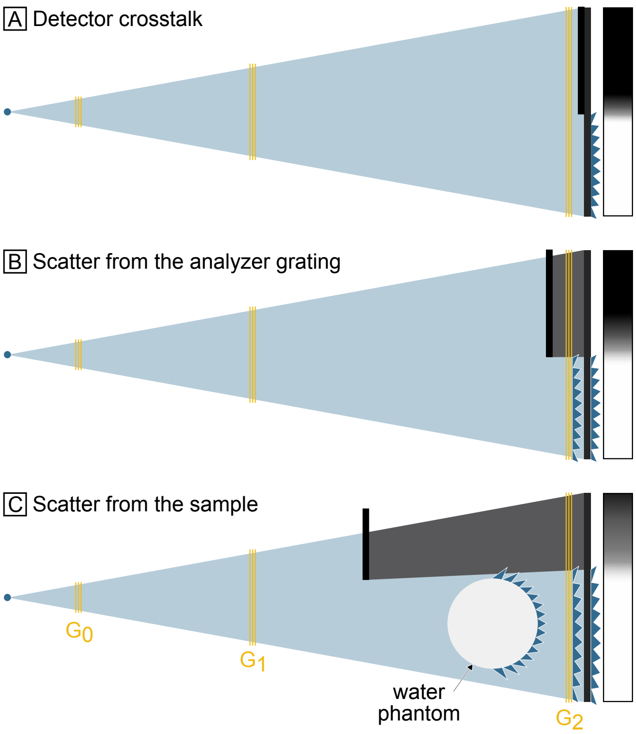
A Detector crosstalk
B Scatter from the analyzer grating
C Scatter from the sample
G0
G1
water phantom
G2

Figure 3.7: Measurements for scatter characterization and verification of scatter estimates. Images show a top view of the dark-field chest radiography system. Depending on the position of the tungsten plate in the beam path, different parts of the system contribute to the intensity measured in the shadow of the plate, depicted on the right. **A**, characterization of detector crosstalk. The plate is positioned directly on the detector. Only intensity due to detector crosstalk is measured in its shadow. **B**, verification of estimates of scatter from the analyzer grating. The plate is positioned just upstream of the analyzer grating. The intensity in its shadow is due to detector crosstalk and scatter from the analyzer grating. **C**, verification of sample scatter estimates. The plate is positioned upstream of a water phantom, such that the water phantom is still fully exposed. The intensity in the plate's shadow is due to detector crosstalk, scatter from the analyzer grating, and scatter from the sample.

3.3.3 Scatter from the analyzer grating

Correction concept

Scatter from the interferometer mainly consists of X-ray photons scattered at the analyzer grating located between sample and detector. The analyzer grating acts both as an anti-scatter grid for all scatter happening upstream as well as a scatter source itself. This includes photons scattered via coherent scattering or incoherent scattering at the substrate, the photoresist, or the grating lamellae, as well as fluorescence photons.

To correct for scatter from the analyzer grating, we use eq. (3.27) similar to the correction for detector crosstalk. However, the expected kernel has a complex shape due to the microscopic structure of the grating. For lack of a simple analytic model, we conducted Monte-Carlo simulations using the Geant4 toolkit (see section 3.3.1).

To estimate the scatter from the analyzer grating with the simulated kernel, we use eq. (3.27), for which the intensity distribution reaching the analyzer grating is

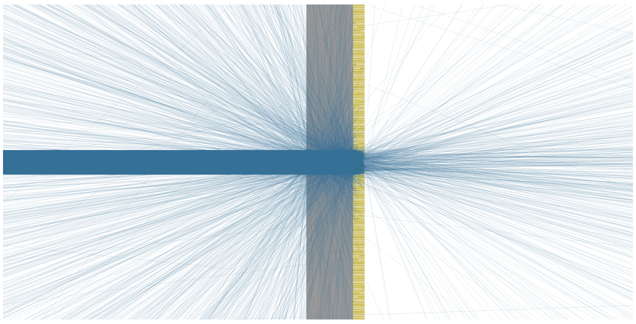

Figure 3.8: Monte-Carlo simulation of scatter from the analyzer grating. The blue lines depict the paths of photons scattered at the analyzer grating. The grating lamellae act as an anti-scatter grid for scatter from the grating substrate and photoresist.

necessary. To this end, we use the scatter-affected attenuation image multiplied with the reference intensity t_j^{r}.

Simulations

Figure 3.8 shows a screenshot of the Monte-Carlo simulation in side view, showing the anti-scatter grid property of the grating lamellae for scatter from the grating substrate.

The incident beam was circular with a diameter of 400 µm, which is slightly smaller than the detector pixel size of 444 µm. The resulting kernel was obtained by recording the energy deposited within the detector by photons that experienced any interaction within the analyzer grating, normalized by the energy deposited by all photons.

The broad active grating area and the lateral fan beam geometry (see fig. 2.6) lead to the beam passing the gratings at angles up to 4.7° with respect to the grating surface normal, and the scanning of the interferometer on a circular arc from $-4.7°$ to 4.7° leads to varying distances between analyzer grating and detector. To obtain a scatter kernel that can be used over the whole field of view, we repeated the scatter kernel simulation with varying incident angle degrees (0° to 4.7° in 10 steps) and varying interferometer positions (0° to 4.7° in 10 steps), obtaining a total of 100 grating scatter kernels. We use the average over all these individual kernels as the resulting kernel for the whole field of view.

To verify that the obtained kernel is indeed valid over the whole field of view, we conducted another simulation. This time, we did not simulate a pencil beam, but increased the grating sizes to cover the whole field of view and exposed the whole detector at once. We further added the barrel-shaped water phantom (see section 3.3.6) at the patient position (which effectively is the same simulation as in fig. 3.9C). This allows to compare the scatter from the analyzer grating estimated with the simulated primary intensity and the kernel to the one from the full-field simulation.

Measurements

For verification of intensities estimated with the simulated kernel, we conducted again measurements with the 2 mm tungsten plate. However, this time, the plate was placed upstream of the analyzer grating on the patient contact plane (see fig. 3.7B). In this configuration, the measured intensity in the plate shadow sums up from scattered photons from the analyzer grating as well as from detector crosstalk.

3.3.4 Sample scatter

Playing a significant role in attenuation contrast, the sample itself is a source of incoherent and coherent scatter. The overall sample scatter intensity depends on sample exposure and of course the sample itself.

Sample scatter is a well-known problem in conventional radiography [109], which is usually counteracted by placing anti-scatter grids right in front of the detector [110]. In our setup, only a comparably small region of the sample is exposed at once. Additionally, the analyzer grating between sample and detector acts as an anti-scatter grid, which prevents most of the photons scattered at the sample from reaching the detector. We chose not to use an additional anti-scatter grid because of dose considerations. As we found that the amount of sample scatter reaching the detector is significant nevertheless, we need to estimate the scatter from the sample.

Correction concept

Both the chemical composition and the spatial distribution of the sample are generally unknown. We adapted the scatter correction software SkyFlow (Philips Medical Systems; [111]), which was originally developed for cases in conventional radiography where no anti-scatter grid can be used. Patches of the sample are approximated by water spheres featuring a locally identical attenuation signal [112], using the scatter-affected attenuation image. Scatter kernels for different water spheres are calculated beforehand using Monte Carlo simulations to allow a fast scatter estimation for a sample measurement.

Dr. Klaus-Juergen Engel (Philips Research, Eindhoven) adapted this approach by calculating the respective kernels specifically for the dark-field chest radiography system with its lower tube voltage and increased distance of the patient to the detector compared to conventional radiography. The gratings were also included to account for the anti-scatter grid property of the analyzer grating.

The Chair got the resulting scatter estimation software as a black box, without any further possibilities to retrace or modify the scatter estimation.

A Barrel-shaped water phantom

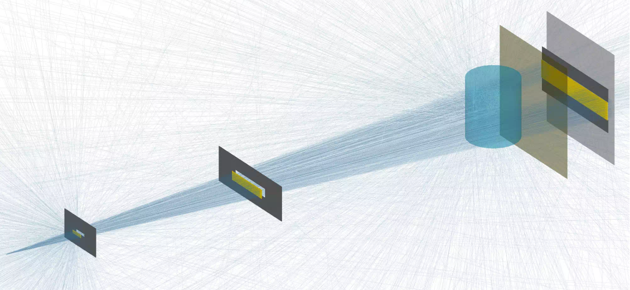

B Lungman phantom

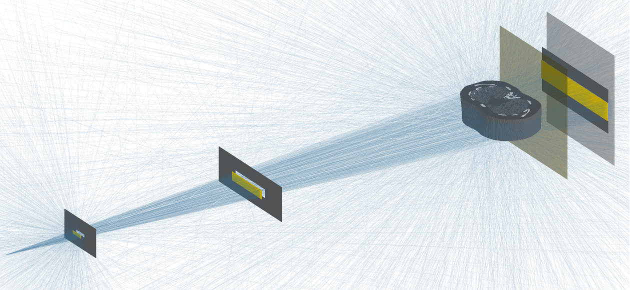

C Barrel-shaped water phantom with full-field gratings

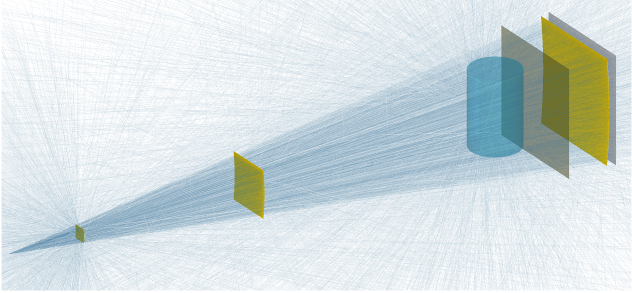

Figure 3.9: Monte-Carlo simulations of experiments for verification of sample scatter estimates and scatter in a hypothetical dark-field chest radiography system with full-field gratings. The blue lines depict the paths of simulated photons. **A**, the barrel-shaped water phantom, with 500000 photons simulated. **B**, the LUNGMAN phantom, with 500000 photons simulated. **C**, the barrel-shaped water phantom in the full-field system, with 1000000 photons simulated.

Simulations

We conducted two simulations with different phantoms to verify the estimations of scatter intensities from the scatter estimation software. We simulated one exposure in horizontal interferometer position, once with and once without the respective phantom. The attenuation image calculated from the simulation was used as input for the scatter estimation software. The resulting scatter intensities from the software can then be compared with the ones from the Monte-Carlo simulation.

As a first simple phantom we used the barrel-shaped water phantom described in section 3.3.6 (fig. 3.9A). It is easy to include in the simulation geometry, and the shape of the phantom is also expected to comply well with the water sphere approximation of the scatter estimation software.

In a second step, we wanted to check if the water sphere approximation is still valid in a more complex, human-like sample. Therefore, we included the LUNGMAN phantom (Multipurpose Chest Phantom N1 "LUNGMAN", Kyoto Kagaku, Kyoto, Japan) in the Monte-Carlo simulation (fig. 3.9B). This phantom mimics the thorax of a average japanese man (168 cm, 65 kg). Its materials represent the attenuating properties of the tissues on the thorax, such that conventional thorax radiographs and chest CTs are very similar to ones from real patients. As we could not get a three-dimensional model of the phantom's internal structure from the manufacturer, we used a CT-scan of this phantom (courtesy of Dr. Lorenz Birnbacher).

The advantage of using a phantom instead of a CT-scan of a real patient is mainly its rigidity. This means that everything, also internal organs, maintain their position between the CT-scan (lying on the examination table) and the dark-field imaging (standing upright). Also, scans can be repeated if necessary.

The procedure to include the CT-scan in the Monte-Carlo simulation was adapted from the `DICOM` example from the Geant4 collaboration [113]: First, the CT is binned to lower the overall resolution and data usage. Second, the HU-values from the CT-scan are converted to the appropriate materials according to the look-up table provided in [113]. Finally, the `G4PhantomParameterisation` class is used to generate a voxelized phantom, where each voxel has the material according to the CT-scan.

Finally, future dark-field chest radiography systems might feature larger gratings that cover the whole field of view, to get rid of the scanning procedure and reduce acquisition time. In this scenario, the larger exposed area would lead to more scatter, especially from the sample. To investigate this effect, another simulation with the barrel-shaped water phantom was conducted, but with a modified system geometry featuring full-field gratings (fig. 3.9C).

Measurements

For experimental verification of the estimated sample scatter intensities, we used the barrel-shaped water phantom described in section 3.3.6 at the patient position as an exemplary, well defined sample. A tungsten plate was put between the G_1 and the water phantom in the beam path, such that the water phantom was still fully exposed, but a part of the direct beam was blocked (see fig. 3.7C). Photons reaching the detector in the shadow of the tungsten plate are due to detector crosstalk, scatter from the analyzer grating, and scatter from the water phantom.

For the estimation of scatter from the water phantom, the attenuation image from the same measurement without the tungsten plate was used, as the scatter correction software would otherwise misinterpret the tungsten shadow as high attenuating water.

3.3.5 Beam hardening

Correction concept

For a characterization of beam hardening induced dark-field signal, we measured its effect with materials that have no micro-structure themselves, but whose spectral attenuation is similar to materials in the human thorax. Candidates for such equivalent absorber materials are Aluminum for bone and either polyoxymethylen (POM) or water for soft and adipose tissue. Their corresponding mass attenuation coefficients are also displayed in fig. 3.5. Water fits a little better to soft tissue, but POM is better for a mixture of soft and adipose tissue, and is easier to handly because it is solid. We therefore initially wanted to use POM.

By performing measurements with different thicknesses of these materials, we can obtain a look-up table connecting the beam-hardening induced dark-field signal with the attenuation. For a correction, we again need to estimate the relative thickness of bone and soft or adipose tissue in the sample. For phantoms, we know the material compostion. For patients, we simply assume that the overall attenuation is half from bone and half from soft or adipose tissue for lack of a better model.

Measurements

All measurements related to beam hardening were performed with the phantoms not at the patient position, but close to the X-ray source, which brings two advantages: First, because of the cone beam geometry we can use smaller phantom sizes in x and y, which simplifies phantom handling. Second, with the large distance from the detector, we reduce the amount of scatter that is generated in the phantom and reaches the detector. To ensure that we actually measure beam hardening induced dark-field signal and not scatter induced dark-field signal, we also simulated the corresponding scatter-to-primary ratios with Monte-Carlo simulations.

The beam hardening induced dark-field signal for a given material depends on the initial spectrum and the visibility spectrum. As both vary over the field of view and especially with grating tile, we used sheets covering the whole field of view for the measurements, increasing material thickness by adding sheets. Thus, we can record calibration curves for every pixel individually.

The material thicknesses were chosen as appropriate to represent the attenuation in patients. All measurements were performed with the same tube configurations as in patient measurements (70 kVp tube voltage and large focal spot). The tube current was adapted to material thickness such that the detector receives the highest possible dose without overexposure. For larger thicknesses, where the maximum tube current of 930 mA was used, multiple scans were conducted to increase statistics.

A POM1 phantom

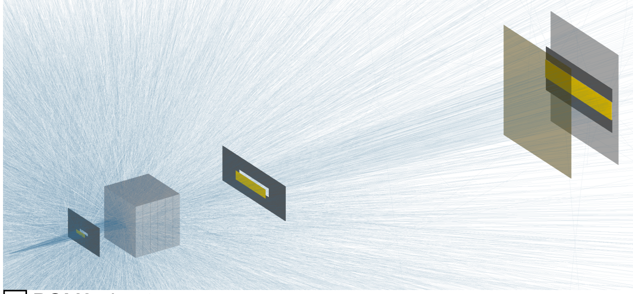

B POM2 phantom

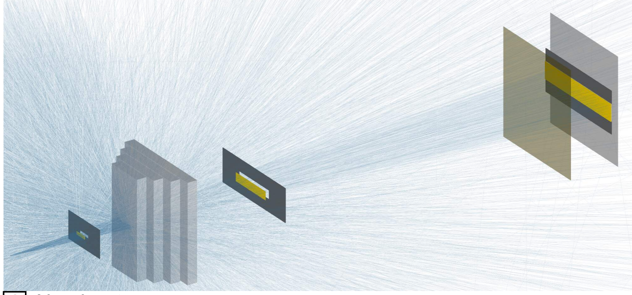

C Alu phantom

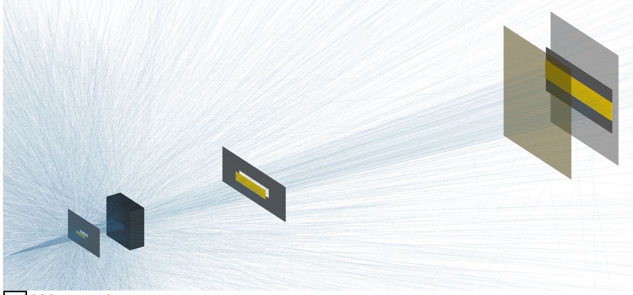

D Water phantom

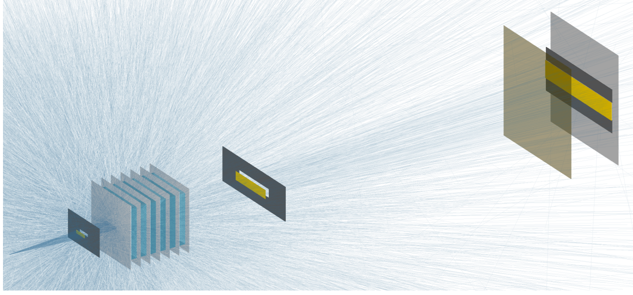

Figure 3.10: Monte-Carlo simulations of experiments for beam hardening characterization. The blue lines depict the paths of 5000 exemplary simulated photons. **A**, the POM1 phantom, with all six sheets in the beam path. **B**, the POM2 phantom consisting of a different set of POM sheets, with all four sheets in the beam path. **C**, the Alu phantom, with all sheets, corresponding to 60 mm thickness, inserted. **D**, the Water phantom, consisting of thin PMMA sheets separating six wells, here all filled with water.

We performed the corresponding calibration for different materials and with different phantoms as summarized in table 3.1: We initially wanted to use POM, as it attenuates very similarly to soft and adipose tissue (see fig. 3.5) and is easier to handle than water. Konstantin Willer designed a dedicated phantom (from hereon called POM1) of six sheets with 3 cm each for that purpose during his PhD [53] (see

Name	Materials	Thicknesses (mm)	Distance from G_0 (cm)	Distance between sheets (mm)	Material between sheets
POM1	POM	30, 60, 90, 120, 150 and 180	44.5	1.5	air
POM2	POM	40, 80, 120 and 160	44.5	5	air
Water	PMMA/ water	9 (PMMA) + 40, 80, 120, 160, 200, and 240 (water)	43	1	PMMA
Alu	Aluminum	2, 4, 6, 7, 11, 14, 21, 25, 30, 39, 50, and 60	46	0	-

Table 3.1: Phantoms for beam hardening calibration. All sheets are added from G_0 in direction of G_1, such that the distance between first sheet and G_0 remains constant. The water phantom has 1 mm PMMA sheets between the wells for the water, and 2 mm PMMA in the front and back, totalling 9 mm of PMMA even with an empty phantom. Abbreviations: POM, polyoxymethylen; PMMA, polymethylmethacrylat.

fig. 3.10A).

We further designed a phantom for beam hardening calibration measurements with water. It consists of thin layers of polymethylmethacrylat (PMMA), separating in total six wells, 4 cm each, that can be filled with water. The phantom without water amounts to a total of 9 mm PMMA in the beam (see fig. 3.10D).

Finally, we also used Aluminum sheets of various thicknesses (1 mm to 21 mm, also imaged together yielding up to 60 mm, see fig. 3.10C) to investigate the difference in beam hardening induced dark-field signal between bone and soft tissue.

Monte-Carlo simulations of scatter in beam hardening measurement

To eliminate the influence of scatter from the measurements for beam hardening calibration, scatter-to-primary ratios were calculated for each measurement with Monte-Carlo simulations. The general framework was as outlined in section 3.3.1.

Figure 3.10 shows the simulated setup for the different phantoms. The phantoms were inserted at their positions and with the appropriate materials. We simulated one exposure with the interferometer in horizontal position. By comparing the intensity from photons scattered at the phantom to primary photons, we obtained the scatter-to-primary ratio s. Assuming no scatter in the reference scan ($s^r = 0$) and using eq. (3.19), the scatter induced dark-field S was calculated. This value was used for all exposures of one scan. To obtain the beam hardening induced dark-field signal without the influence of scatter, S was subtracted from the initially measured dark-field values D' (see eq. (3.18)).

The POM investigation

We found inconsistencies when applying the correction for beam hardening induced dark-field signal found with the POM1 phantom to the barrel-shaped water phantom at patient position. To further examine the POM1 phantom, we repeated the measurements with a second set of POM sheets, 4 cm each, originally planned for another phantom (from hereon called POM2), for comparison (see fig. 3.10B).

We further imaged one of the sheets of both sets individually at different positions between G_0 and G_1, thereby varying the interferometer sensitivity [114]. As beam hardening induced dark-field signal stems only from attenuation, it is not affected by sample position. The scatter reaching the detector varies with sample position. As we accounted for that with Monte-Carlo simulations, we expected to retrieve the same dark-field signal for every position.

3.3.6 Validation phantoms

For testing the proposed correction methods, we used two phantoms. First, as a very simple, purely attenuating sample with known ground truth in the dark-field signal, we used a barrel-shaped phantom of 20 cm diameter. It is made out of PMMA with a wall thickness of 0.5 cm and filled with water.

Second, we used the so-called constancy phantom. It consists of layers of neoprene foam and POM, which are assembled such that there are 5 × 5 fields with different combinations of POM and foam thicknesses over the whole field of view. There is a constant foam thickness in every phantom column. The exact material thicknesses for every field is given in table 3.2.

Both phantoms were imaged at the patient position, i.e. with its center 14 cm from the patient contact plane. We used the standard scan parameters described in section 2.2.3, and a tube current of 140 mA, which is the maximum tube current possible without detector saturation. For the correction for beam hardening induced dark-field signal, we used water only as equivalent absorber material for both phantoms.

3.3.7 Image processing chain

The overall image processing chain to obtain dark-field and attenuation images from the raw data includes corrections detector crosstalk, scatter from the analyzer grating sample scatter, and beam hardening induced dark-field signal as well as corrections for

Constancy phantom

Foam thickness (cm) POM thickness (cm)				
0 0	2 0	4 0	6 0	8 0
0 4	2 2	4 1	6 1	8 1
0 8	2 6	4 4	6 2	8 1
0 12	2 10	4 8	6 6	8 4
0 16	2 14	4 12	6 10	8 8

Table 3.2: Material thicknesses in the constancy phantom for each of the 5×5 fields. Upper number indicates foam thickness, lower number indicates POM thickness. Abbreviation: POM, polyoxymethylen.

other artifacts. The entire processing pipeline is depicted in fig. 3.11. Processing is performed from top to bottom of the flowchart. First, the measured reference intensities are corrected for non-scatter related corrections and detector crosstalk before using eq. (2.6) to calculate the reference images. These are then corrected for scatter from the analyzer grating.

The sample intensities are consecutively corrected for detector crosstalk, scatter from the analyzer grating and scatter from the sample. After each correction, a phase retrieval with eq. (2.7) is performed to update the current sample images before the subsequent step. The correction for beam hardening induced dark-field signal is performed after the final phase retrieval using only the obtained images, not the intensities.

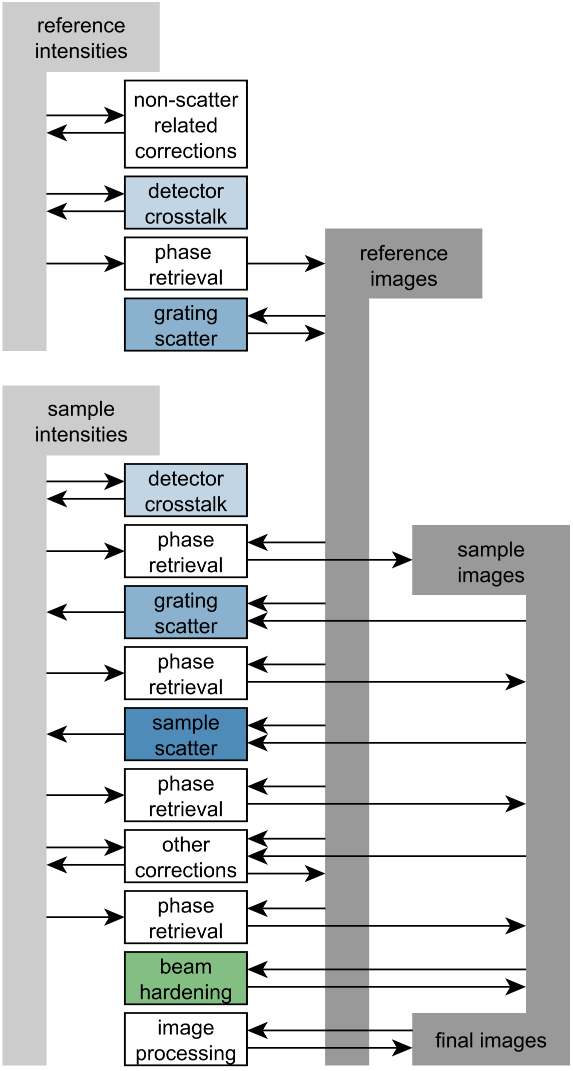

Figure 3.11: Flowchart of processing pipeline, with the applied steps detailed in this work in color. Reference intensities refer to the measured intensities in the reference scans I_j^{r}, reference images refer to the mean intensity t_j^{r}, visibility v_j^{r}, and phase φ_j^{r} of the fringe pattern without an object, see eq. (2.6). Sample intensities refer to the measured intensities in the sample scans I_j, sample images refer to the transmission t, visibility reduction v, and differential phase φ of the sample, see eq. (2.7). After each consecutive estimation of detector crosstalk, scatter from the analyzer grating and sample scatter, respectively, a phase retrieval with eq. (2.7) is performed on the updated inetnsities, whose results are then used to update the images before the subsequent step. Beam hardening is applied after the final phase retrieval, using the reconstructed attenuation for calculation of the beam hardening induced dark-field signal.

Correction for detector crosstalk

Intensities due to detector crosstalk are estimated for both reference and sample measurements for each exposure separately from the measured intensities with eq. (3.32). We account for detector saturation by assuming a direct beam in all overexposed pixels. Via subtraction of the crosstalk intensities, the measured intensities are updated, and a subsequent phase retrieval is performed to obtain the corrected dark-field and attenuation images.

Correction for scatter from the analyzer grating

Intensities due to scatter from the analyzer grating are estimated for both reference and sample measurements for each exposure separately with eq. (3.27). To do so, we need the intensity distribution at the analyzer grating. Since the analyzer grating is very close to the detector, and there are only a few cm of air in between, we can use the intensity at the detector. However, we need to remove the moiré fringes, as these are generated by the analyzer grating and not present in the incident beam.

In the reference measurement, we simply use the initially obtained reference intensity t_j^{r} calculated from the individual reference scans. In the sample measurement, we use the attenuation image scaled with the reference intensity, i.e. $t_j^{\mathrm{r}} t$. Again, we account for detector saturation by assuming a direct beam in all overexposed pixels. Via subtraction of scatter intensities, the measured intensities are updated, and a subsequent phase retrieval is performed to obtain the corrected dark-field and attenuation images.

Correction for sample scatter

The scatter estimation software takes the scatter-affected attenuation image and the reference intensity as input. To avoid artifacts, we account for detector saturation by assuming a direct beam in all overexposed pixels. Additionally, we also set a direct beam in the collimated areas, as these would otherwise be misinterpreted as high attenuating water. Via subtraction of scatter intensities, the measured intensities are updated, and a subsequent phase retrieval is performed to obtain the corrected dark-field and attenuation images.

Correction for mechanical instabilities

The vibrations of the interferometer arm both during and between exposures in the scanning procedure causes fine fringe-like artifacts in the images. We correct for these vibrations by modelling them in the reconstruction process [54]. The vibration during exposures can only be fitted once scatter is corrected for, as both artifacts lead to a reduced visibility.

Correction for patient motion

We correct for artifacts induced by motion of the patient, such as unintended breathing or the heartbeat, by locally reducing the number of evaluated exposures and thus the acquisition time for affected pixels [71].

Correction for artifacts due to shot noise

Noise in areas with low statistics can falsely increase the fitted visibility [115]. To counteract this effect, we locally increase the statistic by reducing the image resolution before reconstruction.

Correction for beam hardening induced dark-field signal

We correct for beam hardening induced dark-field signal using the look-up table as described in section 3.3.5. For the barrel-shaped water phantom and the constancy phantom, we use water only as equivalent absorber material. For patients, we do not know the exact tissue composition. For lack of a better model, we assume that the attenuation is due to soft tissue and bone equally, using water and aluminum as equivalent absorber material.

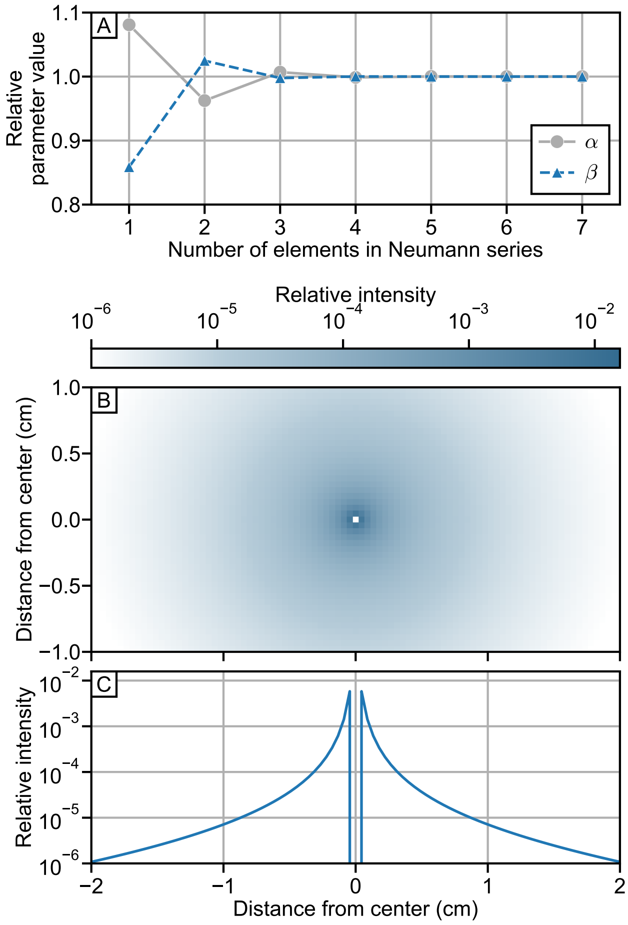

Figure 3.12: Fit of detector crosstalk kernel. **A**, the resulting kernel parameters α and β in dependence of the number of elements after which the neumann series (see eq. (3.32)) is truncated. **B** and **C**, the resulting kernel and its profile using 4 elements in the Neumann series. Parts of this figure have been previously published in [84].

3.4 Results

All scalebars, kernels, and distances shown in this chapter are on the detector plane, with a pixel size of 444 µm × 444 µm. Due to the cone beam geometry, the correspoding effective pixel size at the sample position is about 10 % smaller.

3.4.1 Detector crosstalk

Exemplary frames of the scans without and with the tungsten plate (see fig. 3.7) are shown in fig. 3.13A and B. Since the tungsten plate absorbs all photons coming directly from the source, the intensity measured behind the tungsten plate is only due to detector crosstalk from the adjacent exposed area.
Using all 195 frames from the scan with the tungsten plate (including the one shown in fig. 3.13B) we found

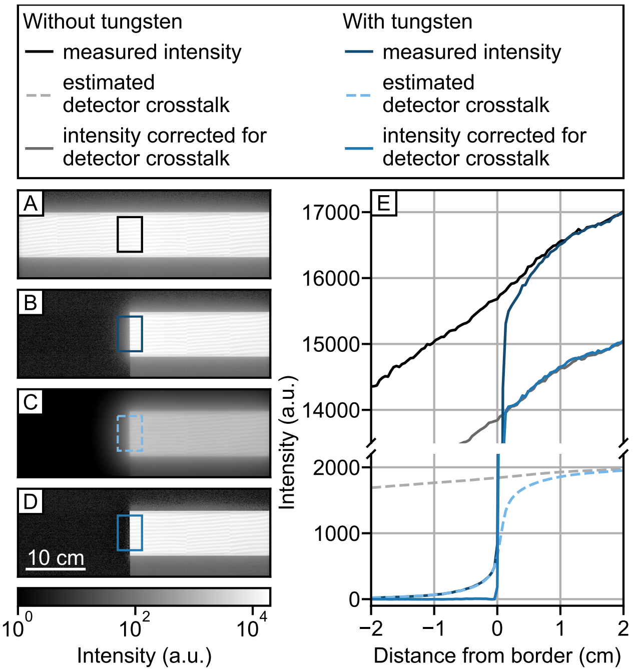

Figure 3.13: Measurement and verification of detector crosstalk estimates. **A**, raw detector image without, **B** with the tungsten plate on the detector. **C**, estimated detector crosstalk, **D**, detector image in **B** corrected with **C**. **E**, profiles of scan with and without the tungsten plates along the indicated rectangles. See fig. 3.7A for measurement details. Parts of this figure have been previously published in [84].

that truncating the Neumann series (see eq. (3.32)) after 4 elements is sufficient (fig. 3.12A). The kernel parameters were then

$$\alpha = 1.17 \times 10^{-3}\,\mathrm{mm}^2 \;(\sigma_\beta = 0.0612 \times 10^{-6}\,\mathrm{mm}^2)$$

and

$$\beta = 0.0499\,\mathrm{mm}^{-1} \;(\sigma_\alpha = 3.34 \times 10^{-6}\,\mathrm{mm}^{-1}).$$

The obtained detector crosstalk kernel $\vec{k}$ is shown in fig. 3.12B and C. The kernel is narrow enough so that the moiré fringes on the detector are still present in the crosstalk intensity estimated with it (fig. 3.13C), proving the necessity of estimating crosstalk separately for every exposure.

The corresponding profiles in fig. 3.13E along the indicated rectangles show that the estimated and measured crosstalk intensities behind the tungsten plate agree very well. The corrected intensity has the expected shape with a clear drop at the tungsten border, and is zero behind the tungsten plate. This is not surprising, since the frame displayed here was part of the data set used for fitting the kernel. However, it indicates that the model used for the kernel (eq. (3.28)) is valid.

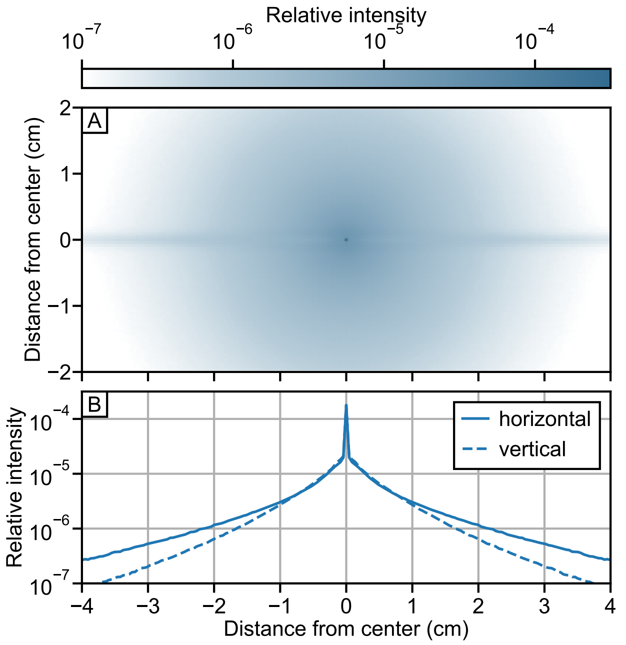

Figure 3.14: The simulated kernel for scatter from the analyzer grating, averaged over the field of view. **A**, the kernel. **B**, its horizontal and vertical profile. The horizontally higher intensity in **A** and corresponding higher horizontal profile in **B** is due to the horizontal orientation of the grating lamellae. Parts of this figure have been previously published in [84].

3.4.2 Scatter from the analyzer grating

The kernel for scatter from the analyzer grating, obtained with Monte-Carlo simulations and averaged over the field of view, is displayed in fig. 3.14. Its center pixel has a high relative intensity, while the surrounding relative intensity of scattered photons is much lower, and distributed broader than in the kernel for detector crosstalk.

The non-circular shape of the kernel is due to the horizontal direction of the grating lamellae, allowing a higher fraction of scattered photons travelling in that direction to pass than photons travelling in any other random direction. Therefore, the profile along the horizontal direction is more intense than the vertical one. This kernel is used for all future estimations of scatter from the analyzer grating. Before a validation of this kernel with further simulations and measurements, a deeper analysis of scatter from the analyzer grating will be given. This includes the underlying processes and scattering sources contributing to it, its spectrum and its dependence on the position in the field of view.

Underlying processes and scatter contributions

The kernel for scatter from the analyzer grating, split by both physical grating component (grating substrate, grating lamellae, and photoresist between lamellae) and by interaction process (photoelectric effect including subsequent fluorescence, coherent scattering, incoherent scattering, or more than one of these) is displayed in fig. 3.15. The contribution in

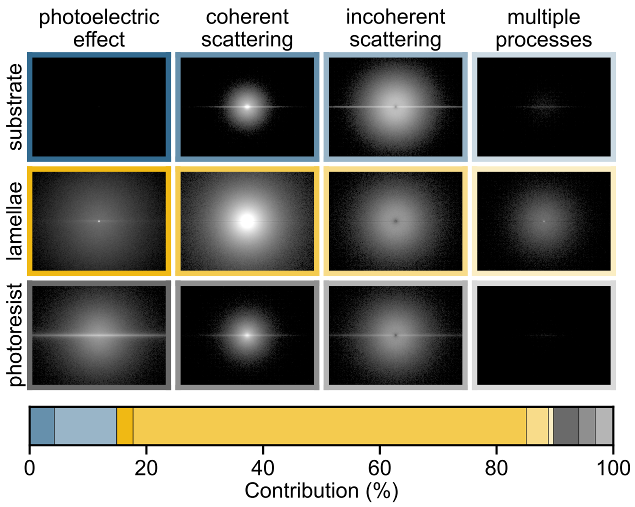

Figure 3.15: Contributions to scatter from the analyzer grating, for position in the center of the field of view, i.e. interferometer in horizontal position and incident angle of the pencil beam on the analyzer grating 90°. The by far most prominent effect is coherent scattering at the grating lamellae. Scatter happening in the grating substrate and photoresist is mostly reabsorbed in the grating lamellae (see fig. 3.8), leading to the horizontal line in the corresponding images.

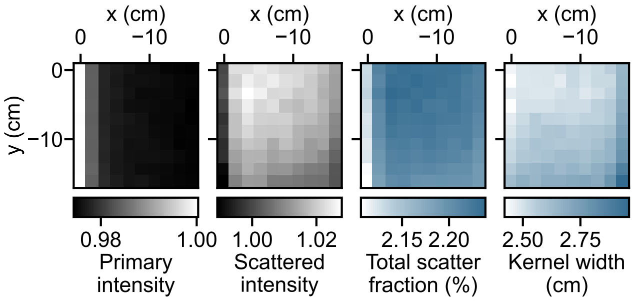

Figure 3.16: Dependency of scatter from the analyzer grating on position in the field of view. Intensities are normalized to the intensity of the pixel in the origin. Kernel width was calculated as the full width at 1 % maximum, assuming a cirular kernel.

this figure refers to the overall portion of photons scattered with the repsective process at the respective material compared to all scattered photons, and is averaged over all energies and the whole kernel area. The by far most prominent effect is coherent scattering from the grating lamellae, which yields relatively narrow profiles. Compton scattering and photoelectric effect have much wider resulting angles.

Scatter from the photoresist and the grating substrate is to a large portion reabsorbed in the grating lamellae, as also shown in fig. 3.8. The resulting distinct horizontal line is therefore only present in the scatter contributions from the substrate and the photoresist.

Dependence on position in the field of view

Figure 3.16 shows the dependency of total intensities and kernel parameters from the position in the field of view, derived from the 10×10 separate grating scatter simulations. The depicted area is the lower right quarter of the total field of view. The evaluated parameters are expected to be symmetric in x and y.

The total primary intensity is highest when $x = 0$, while it decreases towards the outer parts. This effects stems from the bridges in the grating lamellae (see inset in fig. 3.6). In the center of the field of view, the bridges are parallel to the beam direction, and allow a higher fraction of photons to pass the grating. With increasing angle, the effect of the bridges is reduced, as they are not parallel to the beam anymore.

Correspondingly, as the scatter from the analyzer grating stems mainly from the grating lamellae, the total intensity due to scatter from the grating increases with incident angle. Consequently, the total scatter fraction, calculated as the ratio of scattered and primary intensity, increases from 2.11 % to up to 2.24 %.

The kernel width was calculated from the area of the kernel having more than 1 % of its maximum intensity, and then assuming a cirular area to calculate its diameter. This is only a very crude estimate, especially since the assumption of a circular shape is not true (see fig. 3.14). However, we can still see that the kernel width increases a little towards the outer parts of the field of view, probably due to longer propagation distance between grating and detector. This effect is stronger in the vertical direction, where the distance between grating and detector varies more due to the interferometer rotation on a circular arc.

The overall resulting kernel used throughout this thesis was calculated as the mean of these individual kernels.

Spectrum

The spectrum of photons scattered at the analyzer grating is shown in fig. 3.17. The lines at 26.0 keV, 26.3 keV, 29.6 keV and 29.7 keV are the K_α and K_β lines of antimony (Sb) [116], which is present in the photoresist. These lines correspond to photons scatterd via absorption with the photoelectric effect and subsequent fluorescence.

The L_α (9.7 keV), L_β (11.4 keV), and L_γ (13.4 keV) lines of gold (Au) [116] from the lamellae are also distinct and expected. However, the K_α and K_β lines of Caesium (Cs) at 30.9 keV and 35.0 keV and Iodine (I) at 28.6 keV and 32.3 keV [116] are not as easily explained, because these materials are only present in the detector. As the spectra are recorded from all photons travelling in positive z-direction directly before the detector, the fluorescent lines from the detector should not appear here.

Figure 3.18 displays a screenshot of the simulation for scatter from the analyzer grating. Only paths of photons scattered at the analyzer grating and with an energy of 30.9 keV, corresponding to the Caesium K_α

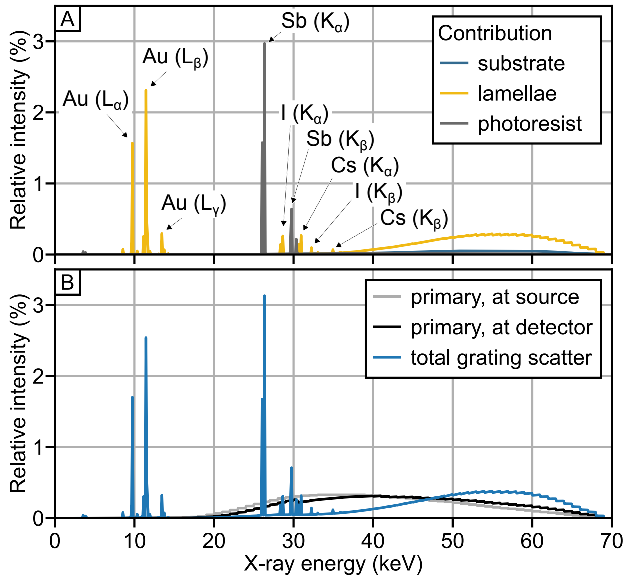

Figure 3.17: Spectra of photons scattered at the analyzer grating. **A**, spectra by physical grating component. The fluorescence lines can be attributed to Antimony (Sb) in the photoresist and gold (Au) in the lamellae, as well as Caesium (Cs) and Iodine (I) in the detector. **B**, the overall spectrum of photons scattered at the anaylzer grating in comparison with the ones of primary photons.

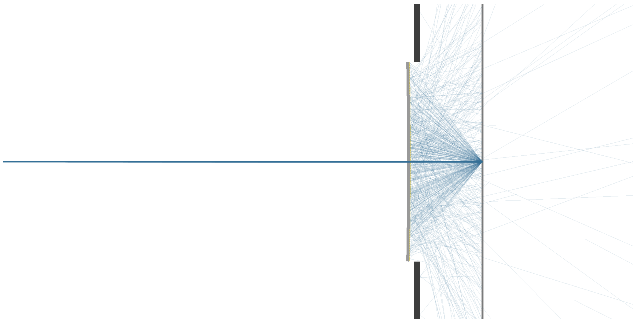

Figure 3.18: Screenshot of Monte-Carlo simulations of scatter from the analyzer grating, showing only photons scattered at the analyzer grating and with an energy of 30.9 keV, corresponding to the Caesium (Cs) K_α line.

line, are drawn. This shows the origin of the Caesium and Iodine lines in the spectrum: Primary photons are scattered at the detector via photoelectric effect and subsequent fluorescence (hence the energy of Caesium and Iodine lines). Some of these fluorescent photons then escape from the detector and travel back towards the analyzer grating. Since the detector itself is not counted as possible scattering source, these photons are still regarded as primary photons. At the analyzer grating lamellae, some of them are again scattered back towards the detector, passing the spectrum counter and now counting as scattered at the anaylzer grating. These photons are spread over the whole detector and contribute mainly to the outer parts of the kernel.

The impact of this process depends on the size of the analyzer grating and detector, as these determine the probability of photons scattered at the detector being scattered again the analyzer grating, and the probability of those photons reaching the detector. However, the overall impact is in all realistic cases admittedly quite small, as the overall intensity of these photons is relatively low. Nevertheless, it is an interesting detail, showing the power of the Monte-Carlo simulation.

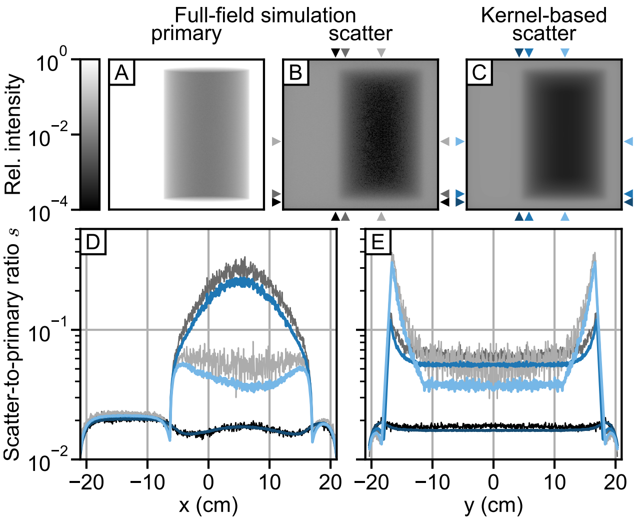

Figure 3.19: Validation of kernel for scatter from the analyzer grating with full-field simulation. **A**, **B**, results of the full-field Monte-Carlo simulation (for simulation details see fig. 3.9C). **A**, intensity due to primary photons. **B**, intensity due to scatter from the analyzer grating. **C**, scatter from the analyzer grating, estimated with the primary intensity in **A** and the simulated kernel. **D** and **E**, the profiles for different locations in the field of view in x- and y-direction indicated by the arrow-heads, respectively.

Validation with full-field simulations

For a validation of the simulated kernel for scatter from the analyzer grating, we used another Monte-Carlo simulation, where the gratings are large enough to cover the whole field of view, and the barrel-shaped water phantom described in section 3.3.6 is positioned at the patient position (see fig. 3.9). Figure 3.19 shows a comparison of the intensity due to scatter from the analyzer grating directly from the full-field simulation with the one estimated from the primary intensity in the full-field simulation and the simulated kernel via eq. (3.27).

Far away from the water phantom (left in fig. 3.19D), the scatter-to-primary ratios agree very well. In the areas around the edges of the phantom (middle and dark blue lines), the kernel still yields reasonably good results, with the correct trends but estimates about 15 % too low. In the center of the water phantom (light blue lines), the scatter-to-primary ratio from the kernel-based estimation is about 30 % lower than the one calculated directly.

The discrepancy of scatter intensities behind the water phantom could be due to beam hardening. The spectrum of the beam behind the water ton is harder than the one used for the kernel simulation. As the

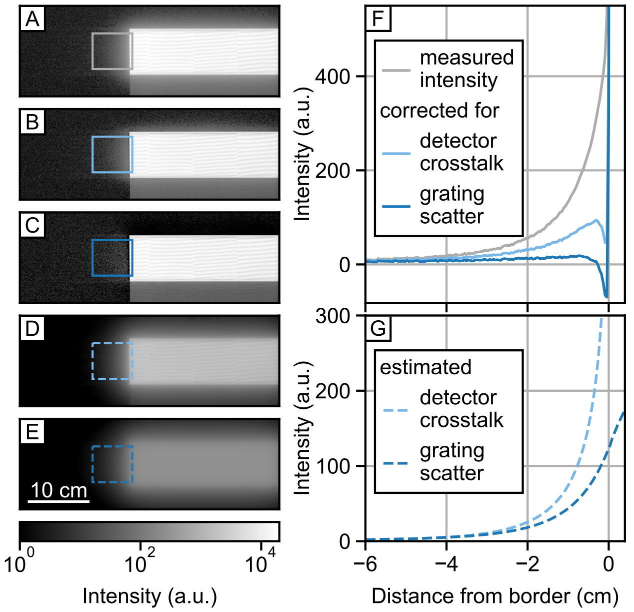

Figure 3.20: Verification of intensities estimated with the kernel for scatter from the analyzer grating. **A**, measurement with the tungsten plate placed upstream of the analyzer grating on the patient contact plane. **B** and **C**, the intensity corrected for detector crosstalk and scatter from the analyzer grating, with **D** and **E** the respective estimated intensities. **F** and **G**, corresponding profiles along the indicated rectangles. After correction for detector crosstalk and scatter from the analyzer grating, the intensity behind the tungsten plate is approximately zero. See fig. 3.7B for measurement details. Parts of this figure have been previously published in [84].

cross sections for the different processes behind scatter at the analyzer grating depend on photon energy, the different beam spectrum leads to different cross-sections and therefore false estimated scatter intensities.

As the overall agreement, especially in the most relevant regions around the edges of the phantoms, was quite well, the current approach was used for all estimations of scatter from the analyzer grating in this thesis.

Verification with measurements

For verification of intensities estimated with the simulated kernel, we conducted again measurements with a tungsten plate, where the measured intensity in the plate shadow (fig. 3.20A) sums up from photons scattered at the analyzer grating as well as from detector crosstalk (see fig. 3.7B). After correction for detector crosstalk and scatter from the analyzer grating, the intensity behind the tungsten plate is approximately zero.

There is a small undershoot close to the tungsten border, which is already present in the profile corrected for detector crosstalk. It is probably due to some inconsistency between the measurement used for fitting the detector crosstalk kernel and the one here. However, this residual artifact is much smaller than the crosstalk effects we are correcting.

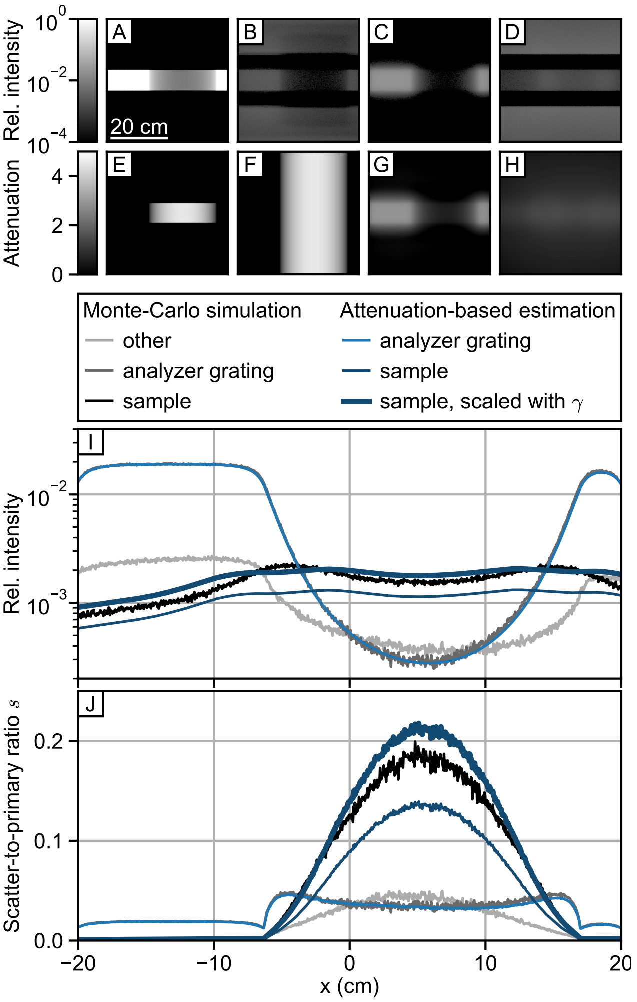

Figure 3.21: Comparison of full Monte-Carlo simulation with scatter estimation for the barrel-shaped water phantom.

Top row: Detector images from the Monte-Carlo simulation. **A**, intensity due to primary photons. **B**, intensity due to photons scattered anywhere but the sample or the analyzer grating. **C**, intensity due to photons scattered at the analyzer grating. **D**, intensity due to photons scattered at the sample. The vertical black bars are due to the tungsten shieldings around the analyzer grating.

Second row: Scatter estimation. **E**, attenuation image from the Monte-Carlo simulation. **F**, attenuation image, continuously expanded beyond the exposed area to avoid artifacts from the edges, used as input for scatter estimation. **G**, estimated scatter from the analyzer grating using the simulated kernel and the attenuation image in **E**, scaled by the reference intensity (not shown). **H**, estimated scatter from the sample, using the adapted Skyflow software and the attenuation image in **F**.

I and **J**, scatter intensity profiles and corresponding scatter-to-primary ratios along the exposed area. The scatter estimation method for scatter from the analyzer grating matches the Monte-Carlo simulation. For scatter from the sample, the estimated intensities need to be scaled with γ.

3.4.3 Sample scatter

Validation of estimates with water phantom simulation

For a first check-up of sample scatter intensities estimated with the adapted Skyflow software, we used a Monte-Carlo simulation of the barrel-shaped water phantom (see fig. 3.9A). This simulation yielded detector images for the different scatter contributions

(fig. 3.21, top row). From these, the attenuation image was calculated and used as input for both grating scatter estimation (see section 3.3.7) and the Skyflow sample scatter estimation software.
The intensities estimated with Skyflow have a slightly different shape than the simulated ones, and they are generally lower. The average ratio γ of scatter intensities from the Monte-Carlo simulation and scatter intensities from Skyflow was

$$\gamma = 1.56\,. \tag{3.34}$$

This factor is from now on used for scaling the scatter intensities from the Skyflow software. However, this is only a quite rough correction, as the ratio between the two sample scatter estimates varies over the exposed area.
This simulation also shows that the estimation of scatter from the analyzer grating works quite well. Also, the scatter from all other contributions besides the sample and the analyzer grating adds up to a scatter-to-primary ratio of about 0.05 in the center behind the water phantom. However, as this is rather small compared to the other two scatter contributions and is more difficult to correct for, we ignore this for now.

Validation of estimates with water phantom measurements

For a further verification of scatter intensities from the Skyflow scatter estimation software, we conducted measurements with the barrel-shaped water phantom described in section 3.3.6 and a tungsten plate (see fig. 3.7C). Photons reaching the detector in the shadow of the tungsten plate are due to detector crosstalk, scatter from the analyzer grating, and scatter from the water phantom. The corresponding intensities were estimated according to their respective algorithms (see section 3.3.7). Intensities for scatter from the sample were scaled with γ (see eq. (3.34)). Figure 3.22 shows the resulting images and intensity profiles.
Intensities due to detector crosstalk and scatter from the analyzer grating are higher than sample scatter close to the edge of the tungsten plate, whereas sample scatter is more uniform and has a far higher range. There is a small remaining intensity close to the tungsten border. This could either be because the single scaling factor of sample scatter over the whole field of view is not entirely correct, and in the area of the direct beam next to the water phantom, we would actually need a higher scaling factor (see fig. 3.21I). Another possible reason could be other scatter contributions that are not yet corrected for. Nevertheless, the intensity behind the tungsten plate is quite flat and close to zero in the corrected image, and the remaining intensity is much less than what we correct for.

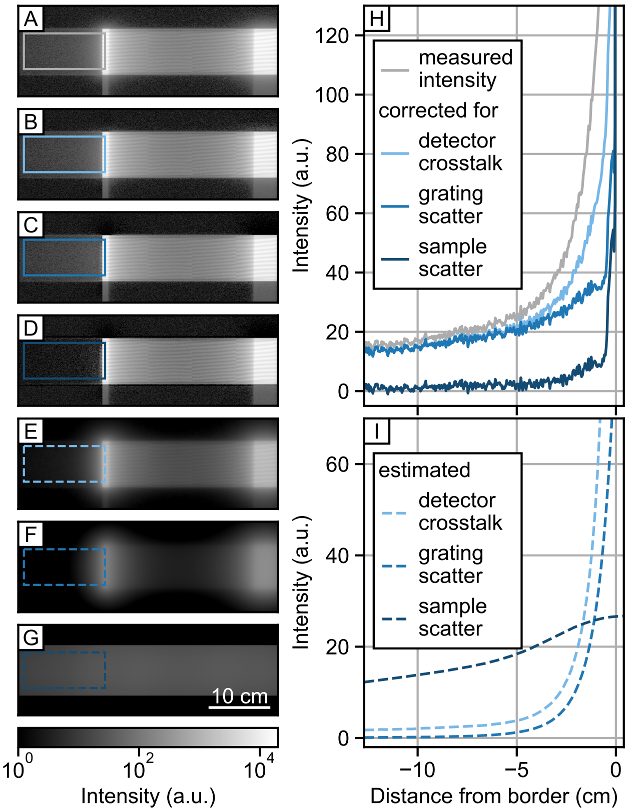

Figure 3.22: Verification of sample scatter estimation with the barrel-shaped water phantom measurement. **A**, measured intensity with the water phantom and the tungsten plate. **B**, **C** and **D**, the intensity after correction for detector crosstalk, scatter from the analyzer grating, and scatter from the sample, with **E**, **F** and **G** the respective estimated intensities. **H** and **I**, corresponding profiles along the indicated rectangles for the measured intensity and estimated scatter and crosstalk intensities. The resulting intensity behind the tungsten plate is flat and close to zero. See fig. 3.7C for measurement details. Parts of this figure have been previously published in [84].

An interesting feature is the small step at the tungsten border in the corrected profiles. This is due to the finite focal spot size: As the focal spot has a rectangular shape with peaks at the edges [117], and the tungsten plate in this measurement is 1.47 m from the source and 0.97 m from the detector, the focal spot width of 1.6 mm leads to this penumbra of 1.1 mm, or 3 pixels, width.

Validation of estimates with LUNGMAN phantom simulation

In a last step evaluating the Skyflow scatter estimation software, we wanted to check how it performs when the sample is more complex than a simple barrel of water. To this end, we used the LUNGMAN phantom. It is similar to a human thorax, meaning that it contains not just water or soft-tissue, but also a material similar to bones. Additionally, these materials are distributed like they are in a thorax, with the ribcage and spine and a cavity for the lungs. All these features

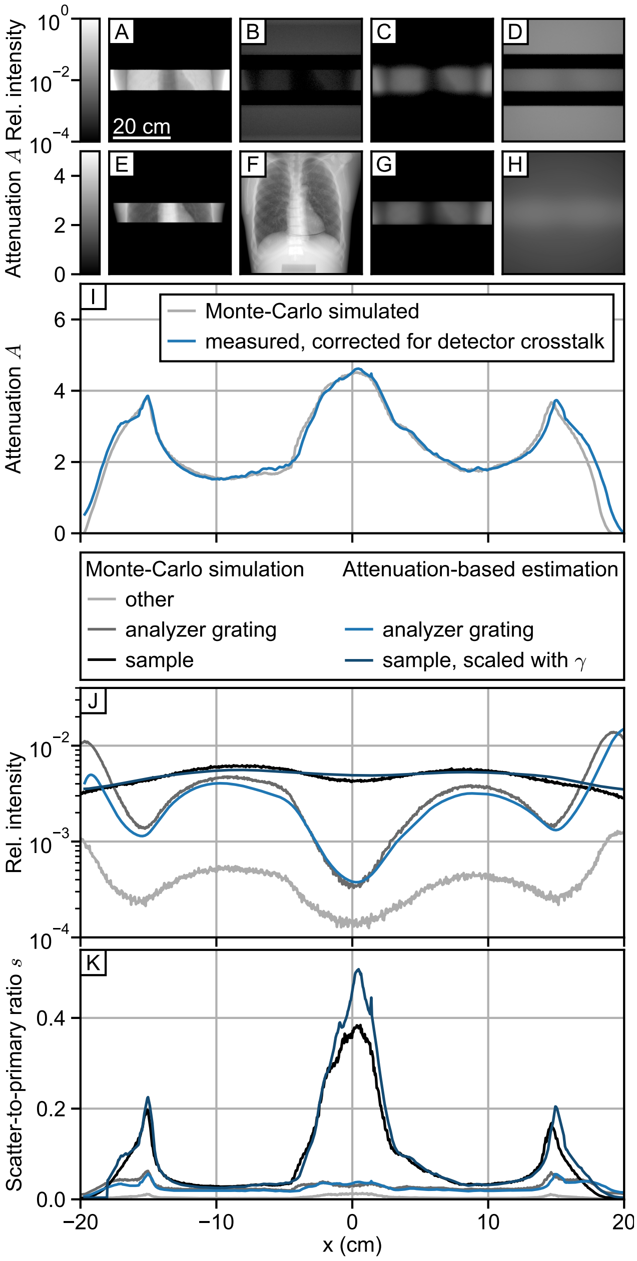

Figure 3.23: Comparison of full Monte-Carlo simulation with scatter estimation for the LUNGMAN phantom.

Top row: Detector images from the Monte-Carlo simulation. **A**, intensity due to primary photons. **B**, intensity due to photons scattered anywhere but the LUNGMAN phantom or the analyzer grating. **C**, intensity due to photons scattered at the analyzer grating. **D**, intensity due to photons scattered at the LUNGMAN phantom. The vertical black bars are due to the tungsten shieldings around the analyzer grating.

Second row: Scatter estimation. **E**, attenuation image from the Monte-Carlo simulation. **F**, attenuation image from a measurement of the LUNGMAN phantom, used as input for scatter estimation. **G**, estimated scatter from the analyzer grating using the simulated kernel and the attenuation image in **F**, scaled by the reference intensity (not shown). **H**, estimated scatter from the sample, using the adapted Skyflow software and the attenuation image in **F**.

I, comparison of simulated and measured attenuation. **J** and **K**, scatter intensity profiles and corresponding scatter-to-primary ratios along the exposed area. The scatter estimation method for scatter from the analyzer grating matches the Monte-Carlo simulation. For scatter from the sample, the estimated intensities scaled with γ are distributed slightly differently than the ones from the Monte-Carlo simulation.

are approximated with water spheres in the Skyflow scatter estimation software.

Figure 3.23 compares the attenuation-based scatter estimations with the results of the Monte-Carlo simulation. As detector crosstalk is not included in the Monte-Carlo simulation, we used the attenuation image corrected for detector crosstalk. We did not correct for any other scatter contribution in neither simulation nor measurement for this comparison.

First, the simulated and measured attenuation images match very well, proving the validity of the simulation.

Second, the overall agreement of scatter intensities calculated with Monte-Carlo simulations with the ones from the scatter estimation algorithms is quite well. The sample scatter intensities estimated with Skyflow were again scaled with γ, yielding the same average scatter intensity, albeit with a slightly different shape, as it was already the case for the water phantom.

Finally, the agreement of the corresponding scatter-to-primary ratios varies over the width of the exposed area. In the area behind the spine, the estimated scatter-to-primary ratio is about 15 % higher than the simulated one. However, in the regions behind the lung, they agree very well.

Scatter influence in a full-field system

Finally, for a hypothetical future setup with the same geometry but with gratings that cover the whole field of view, the influence of scatter is expected to be much higher than in the current scanning system, since a larger volume is exposed at a time. Due to the larger field of view, the exposed grating area increases by about a factor of 6 and the exposed sample volume (due to the size of the sample) by a factor of 5.

Figure 3.24 shows the comparison of simulated intensities for these two systems. The intensities due to scatter from the analyzer grating are higher in the full-field system. They increase about 15 % in the direct beam and up to 50 % behind the sample. This relatively small increase can be explained by the quite narrow scatter kernel and the horizontal grating lamellae with the consequently horizontal predominance of grating scatter. As the exposed area in the slot-scanning system was already horizontally as broad as the field of view, the contribution of scatter from the analyzer grating does not change much with vertically larger gratings.

Scatter from the sample, on the other hand, increases substantially by a factor between 2.5 to 3. This increase is expected and mainly due to the about five times larger exposed volume of the sample. However, the analyzer grating eliminates most photons that are not travelling in horizontal or primary beam direction, acting as an anti-scatter grid. This keeps the overall increase of sample scatter at bay.

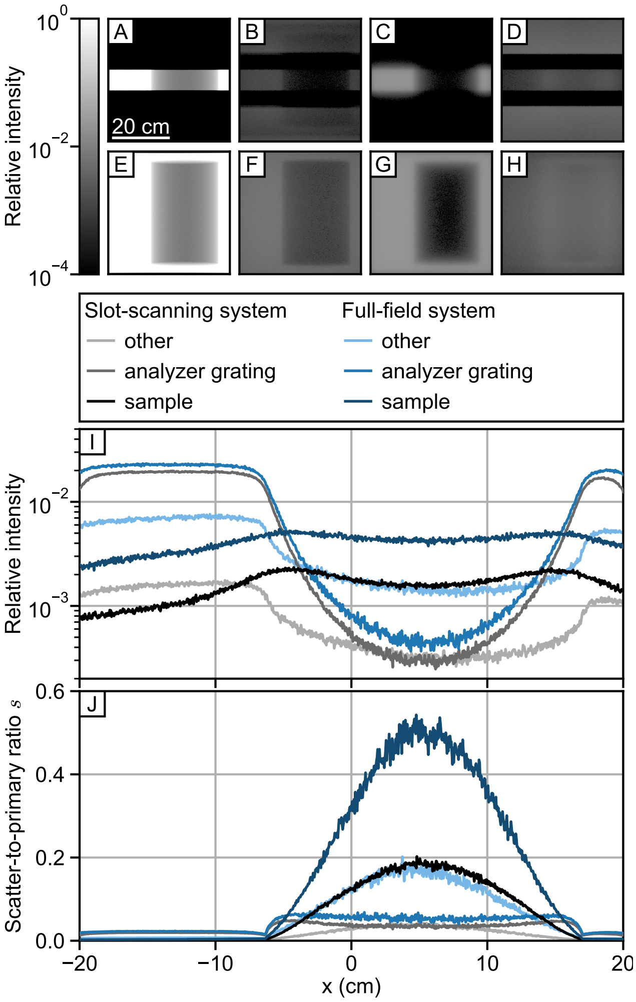

Figure 3.24: Comparison of scatter intensities in a system with full-field gratings to scatter intensities in the current slot-scanning system with the barrel-shaped water phantom.
Top row: Detector images from the Monte-Carlo simulation of the current slot-scanning system (see fig. 3.9A for simulation details). **Second row**: Detector images from the Monte-Carlo simulation of the system with full-field gratings (see fig. 3.9C for simulation details). **A** and **E**, intensity due to primary photons. **B** and **F**, intensity due to photons scattered anywhere but the sample or the analyzer grating. **C** and **G**, intensity due to photons scattered at the analyzer grating. **D** and **H**, intensity due to photons scattered at the sample. The vertical black regions in the top row are due to the tungsten shieldings around the analyzer grating, which were not present in the system with full-field gratings.
I and **J**, scatter intensity profiles and corresponding scatter-to-primary ratios for both systems along the exposed area of the slot-scanning system.

Scatter from other parts of the setup increases most, by a factor of about 4.4 over the whole width of the field of view. With that increase, it is in the full-field system about as high as sample scatter in the slot-scanning system. The main contributions to this other scatter are the patient contact plane, the air in the room and scatter at more than one of the specified materials.

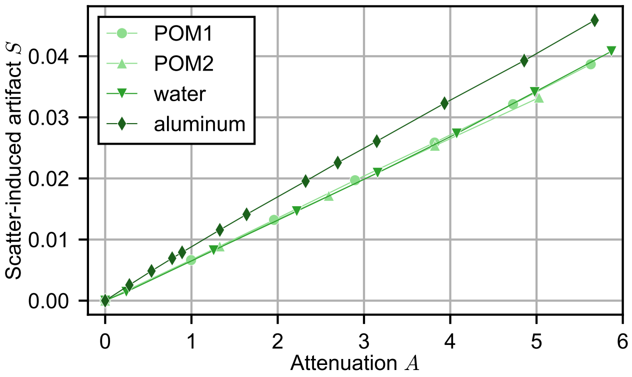

Figure 3.25: Influence of sample scatter in beam hardening measurements with different phantoms (see fig. 3.10 for measurement details). Aluminum scatters more per attenuation than POM or water.

3.4.4 Beam hardening

Scatter in beam hardening measurements

In the following, all measurements are corrected for detector crosstalk and scatter from the analyzer grating with the established corrections. For the correction of sample scatter, the previously described adapted Skyflow software cannot be used because of the different sample positions. Therefore, all measurements were simulated with Monte-Carlo simulations, yielding the sample scatter artifact S, which is subtracted from the measured dark-field signal to obtain the beam hardening induced dark-field signal D_{bh} only. Figure 3.25 shows the resulting simulated artifact S due to sample scatter in relation to the attenuation A for the different phantoms (see fig. 3.10 and table 3.1). As expected, both POM phantoms and the water phantom scatter very similarly. Aluminum on the other hand scatters more per attenuation.

The POM investigation

After we found some inconsistencies when applying the beam hardening correction with the POM1 phantom to the barrel-shaped water phantom, we conducted a deeper analysis of the POM1 phantom used for beam hardening calibration. Figure 3.26 shows the obtained dark-field signal of one sheet of POM from the POM1 phantom POM1, and for comparison, also from one sheet from the POM2 phantom. All measurements were corrected for detector crosstalk and scatter from the analyzer grating with the established corrections, and corrected for the influence of sample scatter via Monte-Carlo simulations. We observe a very different behaviour of the dark-field signal with distance from G_0 for the two phantoms. The measured dark-field signal is relatively constant signal for the sheet from the POM2 phantom, but increases distinctly with distance from G_0 for the sheet from the POM1 phantom.

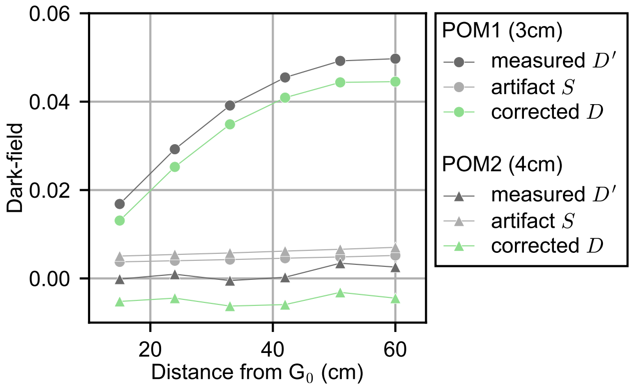

Figure 3.26: The dark-field signal of one sheet of POM from the two phantoms. The artifact due to scatter S was calculated from the simulated scatter-to-primary ratio accodring to eq. (3.19). The sheet of phantom POM1 exhbits a dark-field signal that increases with distance from G_0, while the dark-field signal of the sheet from phantom POM2 is much lower and does not depend as systematically on the sheet's position.

This signal increase indicates that there is some process active that depends on sample position. As beam hardening is a spectral effect and we account for scatter, these effects cannot explain the results. Instead,this can only mean that the sheet from the POM1 phantom generates some true dark-field signal by having an internal micro-structure. This means that when using this POM for beam hardening calibration, we overestimated beam hardening and thus corrected too much, corrupting quantitative signal values.

These results mean that we cannot trust the dark-field signal of POM, as we have two sets of POM sheets generating different signals. We therefore designed a water phantom for beam hardening, which was used for all ensuing beam hardening corrections from here on.

Beam hardening calibration curves

The obtained dark-field images for the different measurements with the water phantom are shown in fig. 3.27. There is a distinct spatial variance of beam hardening induced dark-field signal over the field of view, with a strong dependency on the grating tiles and discontinuities at tile borders. This proves the necessity of using large sheets covering the whole field of view, instead of e.g. step phantoms.

For very small absorber thickness, the beam hardening induced dark-field signal is below zero, meaning that the measured visibility with the absorber is higher than without. This can be attributed to energies with lower visibility than the mean visibility (see fig. 3.5C) being attenuated first. With increasing absorber thickness, also higher energies with higher visibilities are attenuated, leading to overall lower visibility and positive beam hardening induced dark-field signal.

Figure 3.28 shows exemplary beam hardening induced dark-field signals for the different phantoms with different absorber material, as the average over the small region indicated in white in fig. 3.27A. For lack of a model, we used splines for interpolating between the measurement points. There are three things to remark on this graph. First, as already shown in the previous section, the two curves of the POM1 and POM2 phantoms do not overlap. Due to its inherent dark-field signal, the POM1 phantom generates a much higher overall signal than the POM2 phantom, consisting of both true and beam hardening induced dark-field signal.

Second, water does absorb spectrally a little different from POM, leading to a little higher beam hardening induced dark-field signal than the POM2 phantom. As can be seen from fig. 3.5A, POM actually mimicks a mixture of soft and adipose tissue. However, due to the previously mentioned inherent dark-field signal of the POM in the POM1 phantom, we do not trust the dark-field signal of POM any more, and decided to use water for modelling both soft and adipose tissue instead.

Third, aluminum – mimicking cortical bone – generates a about a factor of 4 higher beam hardening induced dark-field signal than water. This indicates the need for an correction for beam hardening induced dark-field signal that is adapted to the sample material. In all phantom measurements with water or POM, we use water as equivalent absorber material for beam hardening correction. In patients, we do not know the exact material composition. For a lack of a better model, we simply use the mean of the water and aluminum curves (black line in fig. 3.27) for beam hardening correction.

3.4.5 Quantitative validation of corrections with phantoms

Barrel-shaped water phantom

For a first validation of the applied corrections, we imaged the barrel-shaped water phantom, described in section 3.4.3. Since water has no micro-structure, the true dark-field signal is known to be zero everywhere. Figure 3.29 shows the obtained attenuation and dark-field images after all corrections, and signal profiles after subsequent correction for detector crosstalk, scatter from the analyzer grating, scatter from the sample, and beam hardening induced dark-field signal. The initially measured dark-field signal behind the water phantom is about 0.25. After all corrections, the dark-field signal contains mainly noise, proving the effect and validity of the applied corrections.

In the artifact due to beam hardening, the spatial variance over the field of view of the beam hardening effect is clearly visible. Detector crosstalk and grating scatter do not depend on location in the field of view, but are only effective at egdes of attenuation.

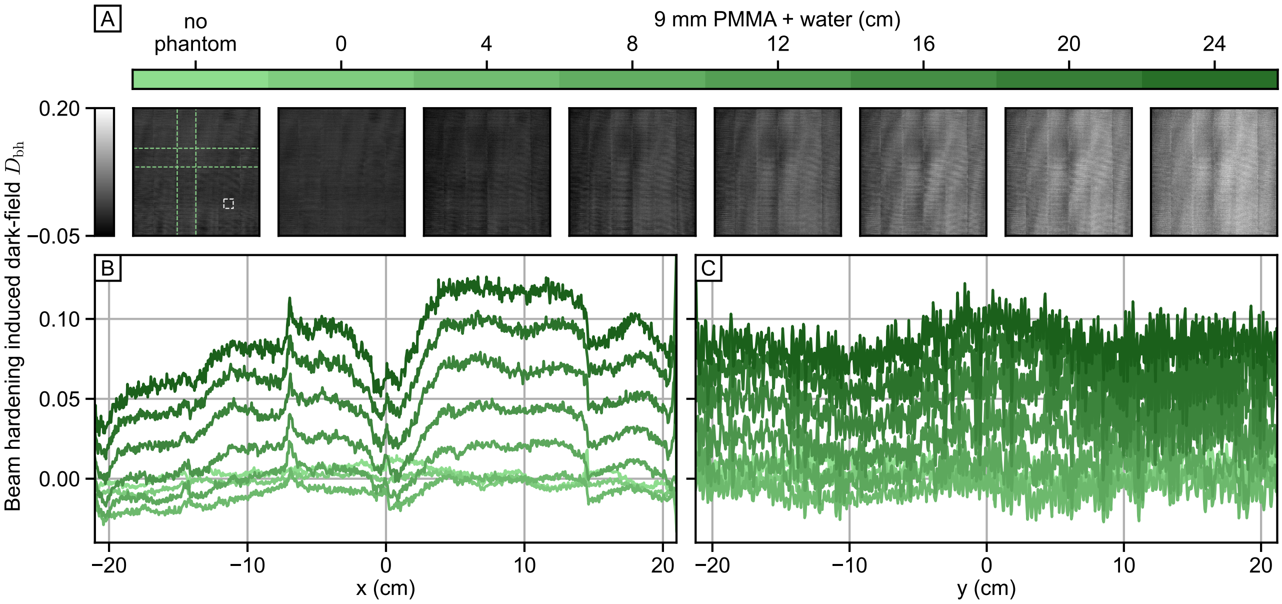

Figure 3.27: Beam hardening induced dark-field signal of water. **A**, obtained dark-field images with increasing aborber thickness of the water phantom. **B** and **C**, horizontal and vertical profiles of the regions indicated in green in the left image in **A** of all dark-field images. There is a distinct spatial variance of beam hardening induced dark-field signal over the field of view, with a dependency on grating tile. The white rectangle in the left image in **A** indicates the region evaluated in fig. 3.28 for different materials.

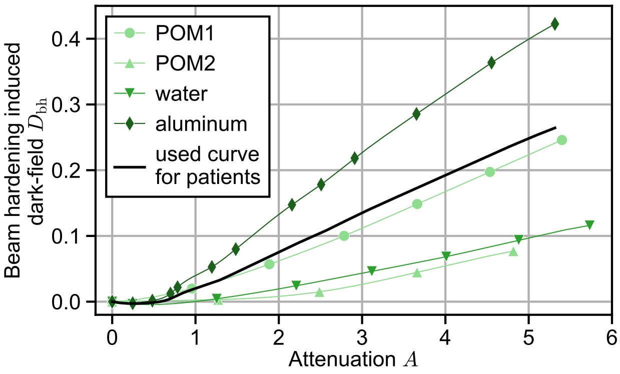

Figure 3.28: Beam hardening calibration curves for the different materials in the region indicated in white in fig. 3.27A.

The small remaining artifact up to about 0.05 on the right and the smaller one of up to 0.02 in the center (fig. 3.29H) are most likely due to the grating tile having slightly different structure or alignment, as the edges of these artifacts correspond to borders between grating tiles.

An interesting detail is the small undershoot just outside the water phantom if no correction for detector crosstalk is applied (fig. 3.29H). It is created by a reduced blur of the interference pattern in the sample scan compared to the reference scan, due to less crosstalk intensity from the neighboring pixels behind the attenuating sample.

Constancy phantom

For a further validation of the quantitivity of the obtained signal, we used the constancy phantom described in section 3.3.6. It consists of layers of neoprene foam and POM, which are assembled such that there is a constant foam thickness and varying POM thickness in every phantom column when it is imaged in normal orientation (see fig. 3.30A and C).

With this phantom, we do not have the ground truth of no true dark-field signal, since the neoprene foam features a micro-structure causing dark-field signal. Additionally, we assume that the POM in the phantom does not generate any true dark-field signal. However, in the light of section 3.4.4 we cannot be sure of that.

To still get a quantitative measure to compare against, we imaged the phantom once in normal orientation and once rotated by 90° counter-clockwise. Due to the slot-scanning image acquisition, this means that different parts of the phantom are exposed at a time for the different phantom orientations. Thus, we expect different effects of scatter in the two orientations, which should be eliminated by the scatter corrections applied. Additionally, the effect of beam hardening also varies over the field of view. If we do all corrections correctly, we expect to measure the same attenuation and dark-field signals in both orientations.

The resulting profiles through the dark-field and attenuation images are shown in fig. 3.30E and F. It is clearly visible that the signal levels from the two orientations do not always match. In the right parts

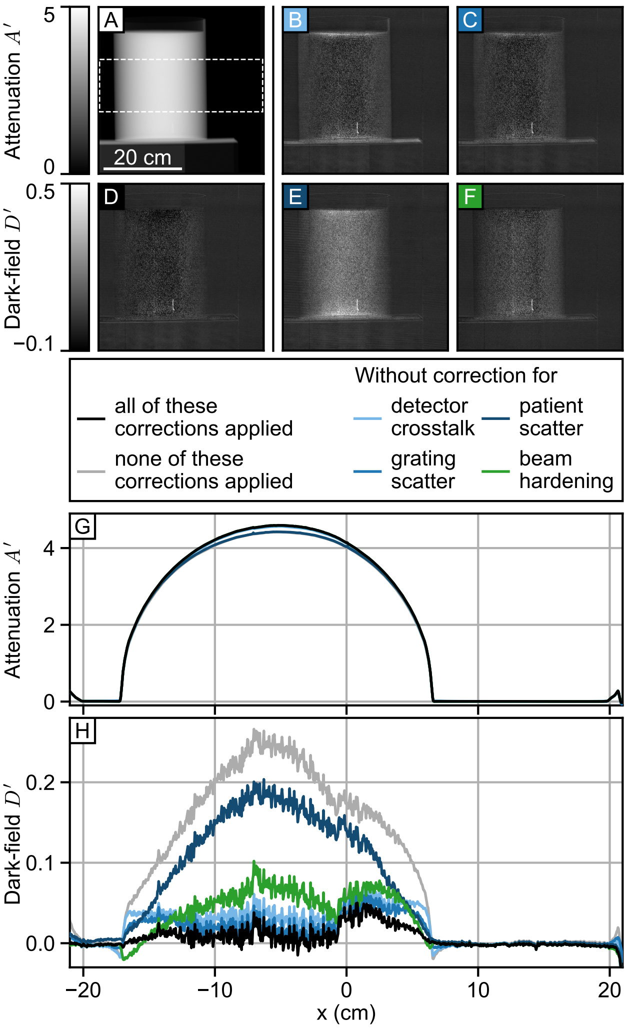

Figure 3.29: Validation of corrections with the barrel-shaped water phantom. **A**, **D**, final attenuation image and dark-field image. **B**, **C**, **E**, and **F**, dark-field images without correction for detector crosstalk, scatter from the analyzer grating, sample scatter and beam hardening induced dark-field signal, respectively. **G**, and **H**, profiles along the rectangle indicated in **A**, applied to all images. After all corrections, the resulting dark-field signal is zero behind the phantom in most regions, with a small positive remaining artifact on the right.

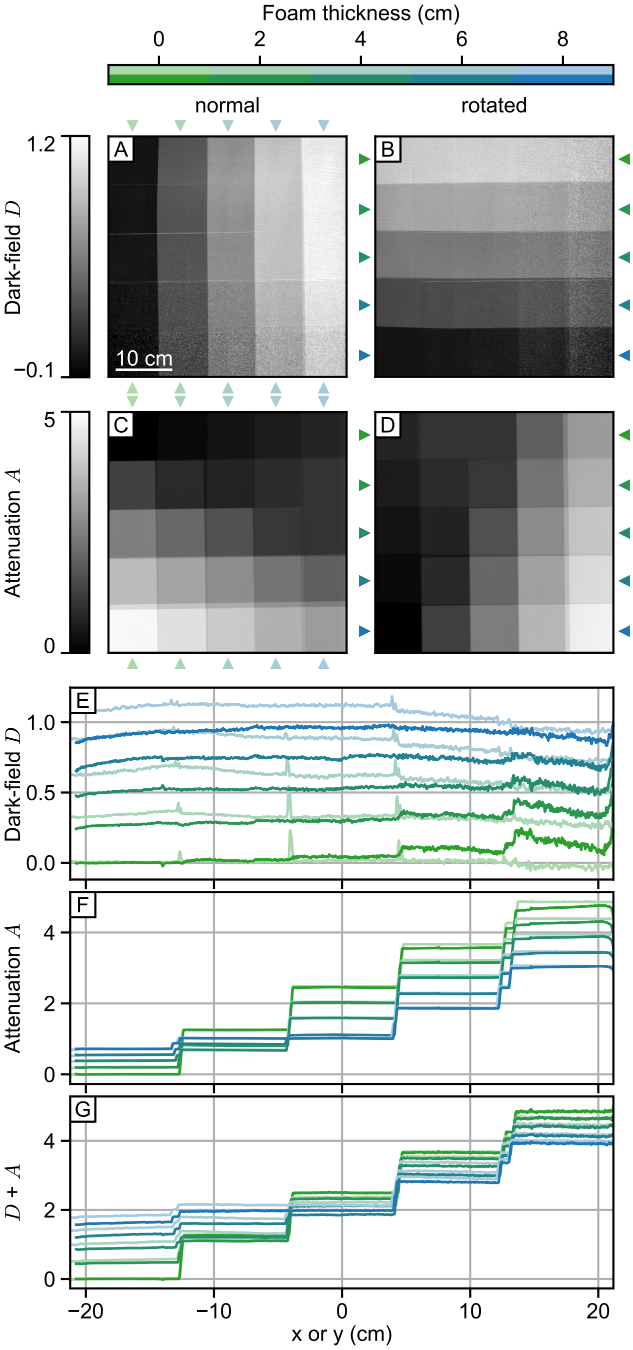

Figure 3.30: Validation of corrections with the constancy phantom imaged in two configurations. **A** and **C**, dark-field and attenuation images in normal orientation. **B** and **D**, dark-field and attenuation images of the phantom rotated by 90° counter-clockwise. **E** and **F** dark-field and attenuation profiles through different constant foam thicknesses of the phantom with varying POM thickness, indicated by the arrowheads. **G**, profile through total signal, i.e. dark-field D + attenuation A, where the influence of scatter is eliminated.

of the dark-field signal profiles, where POM thicknesses are high, we can see a distinct step in the dark-field signal, most prominent when there is no foam at all and the expected dark-field signal is zero (green lines in fig. 3.30E). Additionally, for higher foam thicknesses, there seems to be an offset in the dark-field signal especially in the left parts, where POM thicknesses are low (blue and purple lines in fig. 3.30E). Further, the dark-field signal is not constant for constant foam thicknesses in both orientations, but more prominent in normal orientation.

In the attenuation profiles, the differences are less distinct, partly because of the generally higher signal levels and steps with increasing POM thickness, but also because there are mainly small differences in the right part with high POM thicknesses.

To check if the remaining inconsistencies between the two orientations are due to scatter, we added up attenuation and dark-field images (fig. 3.30G). This eliminates the influence of scatter from the obtained images (see eqs. (3.17) and (3.18)). In the resulting profiles, the inconsistencies in the right parts at high POM thicknesses are removed, indicating that these are actually due to incorrect scatter estimates.

Unfortunately, the inconsistencies in the left parts remain, meaning that these are not from scatter but some other effect. If this effect was beam hardening induced dark-field signal, which does vary over the field of view, we would expect it to be worse for high POM thicknesses, but we actually observe that it is worst for high foam thicknesses and low POM thicknesses. Also, we would expect some effect of the grating tiles in the resulting images, which we also do not observe. Therefore, beam hardening is an unlikely explanation.

Another possible effect could be a directional dark-field signal from the foam. As our grating lamellae are oriented horizontally, we are sensitive to horizontal structures in the sample. If the micro-structure in the foam does not consist of isotropic bubbles, but has an anisotropic property, this could lead to a true dark-field signal varying with sample orientation. To check this explanation, further measurements with e.g. stepping only and very small collimation could be conducted.

Finally, I want to point out another effect visible in these measurements. The foam thickness increases by 2 cm in every sample column. The dark-field signal especially in the rotated orientation however does not increase by a constant value from column to column. Instead, the difference between 0 cm and 2 cm foam is about 0.3, while the difference between 6 cm and 8 cm foam is only about 0.15. This is due to the so-called visibility hardening [92]. This effect leads to a reduced dark-field signal per foam thickness with increasing foam thickness, in analogy to beam hardening in attenuation imaging. It has been proven and investigated by De Marco et al. at another setup of the Chair [92]. This measurement here shows that we also suffer from it, and its correction will hopefully be part of future Master's or PhD theses.

3.4.6 Application to dark-field chest radiographs

After validating the developed corrections with known phantoms, we now want to evaluate their effect in dark-field chest radiographs of humans. To do so, we use images acquired during the currently ongoing patient study on the diagnostic value of dark-field chest radiography for COPD. See sections 2.2.3 and 4.3.2 for details on image acquisition.

Images in pa orientation

Figures 3.31 and 3.32 show chest radiographs of an 42-year old woman imaged in posterior-anterior orientation at the clinical dark-field chest radiography system, and the dark-field signal profiles along the indicated regions, respectively. All images are corrected for other effects unrelated to detector crosstalk, scatter or beam hardening induced dark-field as described in section 3.3.7. Note that the attenuation image has not undergone contrast enhancement usually performed before clinical evaluation, an therefore shows actual quantitative attenuation.

The panels in the top row show the final dark-field (fig. 3.31A) and attenuation image (fig. 3.31B) after all corrections. The other panels show dark-field images with either one or all of the corrections for detector crosstalk, grating scatter, patient scatter, or beam hardening induced dark-field signal disabled, along with the corresponding artifact image.

In the uncorrected image (fig. 3.31K and gray lines in fig. 3.32), in addition to the true dark-field signal of the lung there is an additional, spurious signal. This affects the whole image, but especially the ribs, the spine, the abdomen, and the shoulders. For example at high edges of attenuation, as in the rib case with direct beam close by, the uncorrected dark-field signal goes up to about 0.7 (middle indicated region in fig. 3.31 and fig. 3.32B). Furthermore, in the abdomen, where we do not expect to measure any true dark-field signal for lack of tissue with micro-structure, the uncorrected dark-field signal goes up to about 0.3 (lower indicated region in fig. 3.31 and fig. 3.32C). These effects impede the qualitative assessment of the dark-field signal of the lung, as e.g. the lower edges of the recessus behind the diaphragm cannot clearly be distinguished, and make a quantitative assessment impossible.

As expected from the application of corrections to the barrel-shaped water phantom, the different artifact contributions have different effects in the dark-field chest radiographs. Detector crosstalk and scatter from the analyzer grating have their strongest impact in the vicinity of edges in the attenuation image, such as the shoulders and the rib cage close to the direct beam.

The scatter from the patient itself mainly affects regions where the overall attenuation is highest, such as the abdomen and spine, as in these regions, the scatter-to-primary ratios are highest.

The effect of beam hardening induced dark-field signal also depends on the overall attenuation. However, it depends on the location on the detector and the grating tile, too, and thus shows vertical stripes in the respective difference image (fig. 3.31J).

After all corrections are applied, the dark-field signal outside of the lung is mostly close to zero (fig. 3.32), while the dark-field signal in the lung remains.

Images in lat orientation

For the same 42-year old woman, the corresponding dark-field radiographs and effects of the different corrections are shown in figs. 3.33 and 3.34. Note the shadow of the collimation on the left and right, as well as the high apparent dark-field signal due to detector saturation in the direct beam.

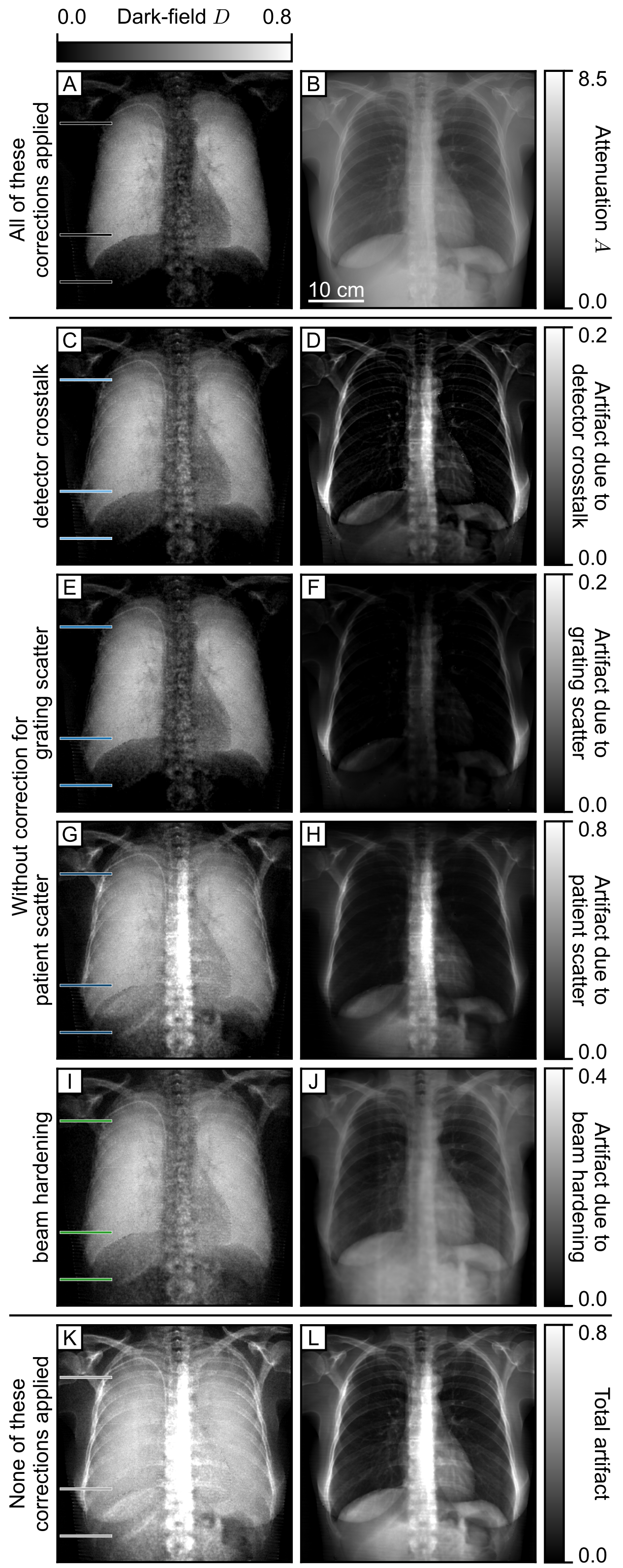
0.0 Dark-field D 0.8
A
B
10 cm
8.5
Attenuation A
0.0
All of these corrections applied
C
D
0.2
Artifact due to detector crosstalk
0.0
detector crosstalk
E
F
0.2
Artifact due to grating scatter
0.0
grating scatter
Without correction for
G
H
0.8
Artifact due to patient scatter
0.0
patient scatter
I
J
0.4
Artifact due to beam hardening
0.0
beam hardening
K
L
0.8
Total artifact
0.0
None of these corrections applied

Figure 3.31: Effect of corrections on dark-field chest radiographs of a 42-year old woman in pa orientation. **A**, final dark-field and **B**, final attenuation image after all corrections. Note that the attenuation image is without contrast enhancement usually applied before clinical evaluation. **C**, **E**, **G**, and **I**, dark-field images with either one of the corrections for detector crosstalk, grating scatter, patient scatter, or beam hardening induced dark-field signal disabled, with the corresponding artifact image on the right (**D**, **F**, **H**, **J**). **K**, and **L**, dark-field image and artifact image from reconstruction without any of these corrections.

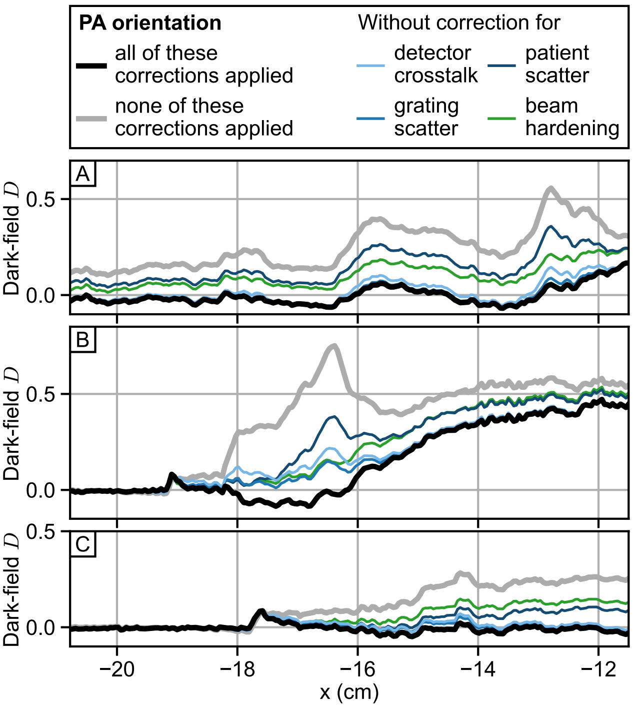

Figure 3.32: Quantitative evaluation of corrections on dark-field chest radiographs in pa orientation. See fig. 3.31 for the respective radiographs. **A**, profiles along highest region. **B**, profile along middle region. **C**, profile along lowest region. Corresponding regions are indicated in color in fig. 3.31.

After application of all corrections, the dark-field signal is mostly close to zero outside of the lung. In the upper parts and behind the shoulders (upper indicated region in fig. 3.33 and fig. 3.34A), the dark-field signal is reduced from about 2.0 to about 0.1. However, there is some dark-field signal in the very upper part of the thorax in fig. 3.33A that does not have a corresponding signal in the pa image in fig. 3.31A and is thus most likely a remaining artifact.

There is also a slight overcorrection in the abdomen (lower indicated region in fig. 3.33 and fig. 3.34C), which is most likely due to the correction for beam hardening induced dark-field signal assuming a mixture of bones and soft tissue in the beam path, while the abdomen consists of soft tissue only.

3.5 Discussion

In this chapter, we describe the influence of detector crosstalk, scatter from the analyzer grating and the sample, and beam hardening on dark-field radiographs. We propose methods for correction of the induced artifacts. For detector crosstalk and scatter, we propose algorithms to estimate the respective intensities. For beam hardening, we show a calibration procedure using equivalent absorber materials.

The overall influence of crosstalk, scatter, and beam hardening induced dark-field signal in dark-field chest radiographs is substantial. Especially in regions

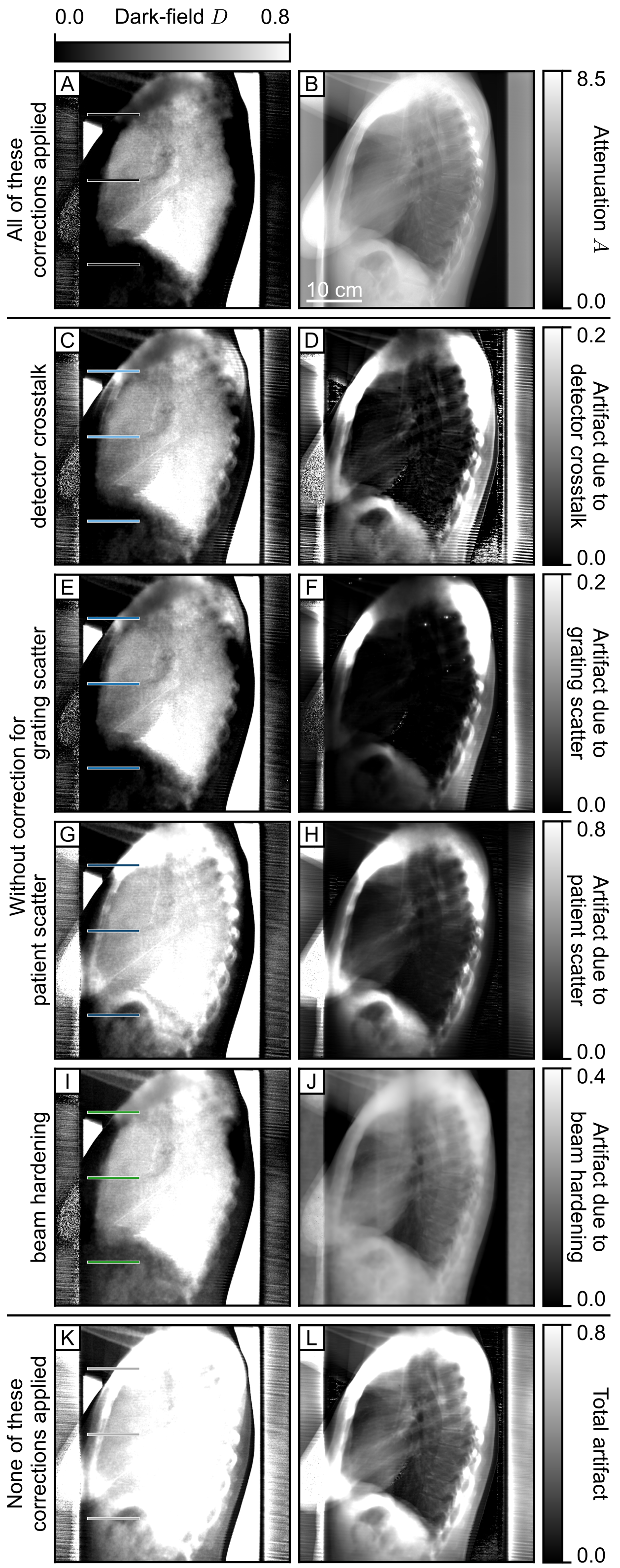
0.0
Dark-field D
0.8
A
B
All of these corrections applied
10 cm
8.5
Attenuation A
0.0
C
D
detector crosstalk
0.2
Artifact due to detector crosstalk
0.0
E
F
Without correction for
grating scatter
0.2
Artifact due to grating scatter
0.0
G
H
patient scatter
0.8
Artifact due to patient scatter
0.0
I
J
beam hardening
0.4
Artifact due to beam hardening
0.0
K
L
None of these corrections applied
0.8
Total artifact
0.0

Figure 3.33: Effect of corrections on dark-field chest radiographs of the same 42-year old woman as in fig. 3.31 in lat orientation. **A**, final dark-field and **B**, final attenuation image after all corrections. Note that the attenuation image is without contrast enhancement usually applied before clinical evaluation. **C**, **E**, **G**, and **I**, dark-field images with either one of the corrections for detector crosstalk, grating scatter, patient scatter, or beam hardening induced dark-field signal disabled, with the corresponding artifact image on the right (**D**, **F**, **H**, **J**). **K**, and **L**, dark-field image and artifact image from reconstruction without any of these corrections.

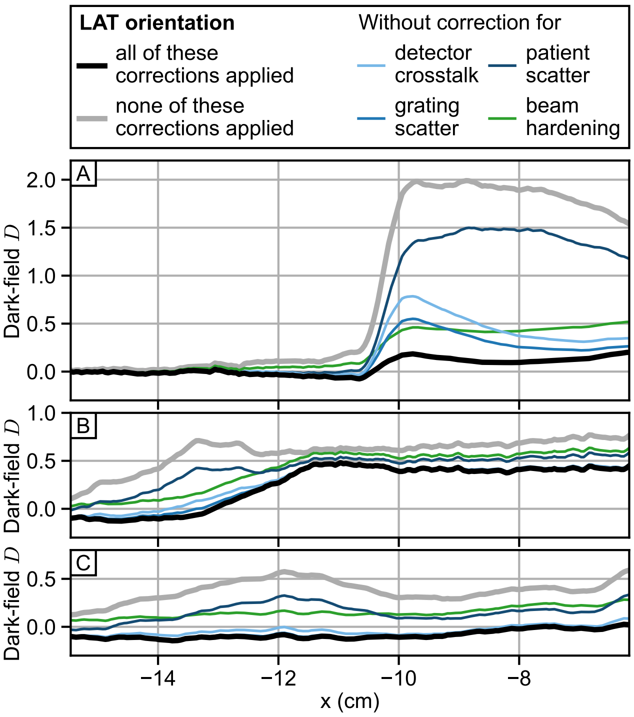

Figure 3.34: Quantitative evaluation of corrections on the dark-field chest radiographs in lat orientation. See fig. 3.31 for the respective radiographs. **A**, profiles along highest region. **B**, profile along middle region. **C**, profile along lowest region. Corresponding regions are indicated in color in fig. 3.33.

with high attenuation such as the abdomen and spine, there is strong beam hardening and a high ratio of scatter to primary intensities, and the apparent dark-field signal is actually dominated by artifacts.

The proposed correction algorithms

The proposed scatter correction algorithms estimate the scatter intensities separately for the three main contributions detector crosstalk, scatter from the analyzer grating, and scatter from the sample, with different algorithms due to the different mechanisms. The kernel for detector crosstalk is modelled analytically, and measurements where the primary beam is artially blocked are used to fit the parameters of the kernel. The kernel for scatter from the analyzer grating was calculated with Monte-Carlo simulations, and we conducted an in-depth analysis of the physical processes behind it. Scatter from the sample is estimated with an adapted version of a commercially used kernel-based scatter estimation software.

Monte-Carlo simulations of the full imaging procedure are used to validate the intensities estimated with the obtained kernel-based estimations. Furthermore, measurements where the primary beam is partially blocked are used to show that the estimated intensities match the measured ones.

The proposed correction for beam hardening induced dark-field signal is based on calibration measurements with phantoms with equivalent absorber materials. We use water as equivalent absorber for soft and adipose tissue, and aluminum for bones. We generate a spatially differential look-up table to connect attenuation with the associated beam hardening induced dark-field signal.

POM in dark-field imaging

We found that using POM as phantom material does not yield consistent results. The two sets of POM sheets with different dark-field signal were ordered from the same manufacturer, with the same specifications, but at different times.

After these findings, we wanted to further investigate the origin of the dark-field signal of the POM sheet, by imaging the sheets from both phantoms at another laboratory dark-field setup with a higher sensitivity and at a micro CT setup. However, due to the global pandemic, we never actually got around to doing so. Hopefully, this we be part of another Master or PhD thesis in the future.

For now, these results mean that we cannot trust the dark-field signal of POM, and should avoid using POM for calibrations whenever more than just its attenuation is evaluated. This also applies to other dark-field imaging setups.

Validation with phantoms

With a water phantom we validate the correction of the dark-field images of a purely attenuating sample quantitatively. The constancy phantom is used to evaulate the corrections in a more complex sample with a true dark-field signal.

The water phantom is a very simple sample, whose material and spatial distribution can be very well modelled by the scatter estimation algorithm for sample scatter, and whose material is the same as in the calibration measurement for the correction for beam hardening induced dark-field signal. The constancy phantom is more complex, but again consists of known materials and distributions. In a real patient, there are other materials present, which may not be modelled correctly with water and aluminum, and the assumption of water and aluminum being equally responsible for beam hardening is surely too simple for a human thorax.

Additionally, the materials may be distributed quite differently along the beam path, e.g. because of the lung cavity in the thorax, so the approximation with water spheres in the sample scatter estimation might lead to less realistic estimates.

Effect on patient images

The patient images show that detector crosstalk and scatter from the analyzer grating have their main impact near edges of attenuation, while sample scatter and beam hardening have their main impact when the overall attenuation is highest. For the general image impression, the influence of scatter from the sample is much larger than the one from detector crosstalk and scatter from the analyzer grating. This is because the whole exposed sample region acts as a source of scattered photons, with a high spatial range across the whole detector, whereas the range of detector crosstalk and scatter from the analyzer grating is much smaller.

Due to the larger regions with direct beam, a higher tube current leading to higher detector and grating exposure in these direct beams, and stronger attenuation close by, the influence of detector crosstalk and scatter from the analyzer grating is higher in lateral than in posterior-anterior orientation. Patient scatter and beam hardening are also more prominent in lateral images, mainly because of the overall higher attenuation due to more tissue in the beam path.

Sources of errors in the correction algorithms

A potential source of incorrect scatter or crosstalk estimates is detector saturation. As we use raw images for the estimation of detector crosstalk and attenuation images for the estimation of scatter from the analyzer grating and the sample, wrong values in these images also cause wrong estimates. A first countermeasure is a careful collimation to minimize the detector area not covered by the patient. Further, we reduce the effect of detector saturation by assuming a direct beam in all overexposed pixels. However, this assumption is not correct everywhere, as image areas might still run into detector saturation despite low attenuating sample features.

Another potential source of incorrect sample scatter estimates is the sample positioning, as the scatter intensity on the detector depends on sample to detector distance, which is included in the scatter estimation software. In phantom measurements, we can easily ensure a correct positioning, while for patients with varying anatomy, this is not always possible.

Limitations of the used methods

The proposed methods to establish artifact corrections have limitations. For detector crosstalk, the main methodological uncertainty is the model in eq. (3.28) used for fitting the kernel to the measurements. This model is rather simple and physically motivated. It includes only one source of detector crosstalk, while in reality, there might be more processes, e.g. X-ray and optical photon scattering, with different amplitudes α and attenuation coefficients $beta$ contributing to the overall observed crosstalk intensity distribution. However, the agreement of the estimated and the observed crosstalk intensities in fig. 3.13 indicates that one process modeled is sufficient.

The Monte-Carlo simulations used for the corrections of grating scatter and sample scatter depend on the so-called physics list, where all particle interaction probablities and outcomes are specified. We used the livermore physics list, which is intended for low-energy X-rays, i.e. X-rays in the keV energy range. Nevertheless, the exact interaction probabilities are not known for sure, and there exist other physics lists for low energy X-rays, e.g. the penelope or standard physics lists, which could yield slightly different results. Overall, the agreement of measurements and simulations show the validity of the used Monte-Carlo physics model, but smaller deviations in the scattered intensity distributions might be missed.

Another limitation is the adaption of the commercial Skyflow algorithm by our industrial collaborator, without provision of a detailed insight into the simulation framework or the used code. This means we cannot validate or test this algorithm with different scenarios. Further, the restricted access to this collaboration and algorithm is especially inconvenient for other groups who want to implement a similar dark-field radiography system.

For the correction for beam hardening induced dark-field signal, the main limitaion is within the calibration measurements. These have to take place in very controlled conditions and with very well-known phantoms and equivalent absorber materials, to avoid any other effects impacting the measured beam hardening induced dark-field signal. We learned this the hard way when trying to use POM as an equivalent absorber material.

Other possible methods and improvements

For the correction of detector crosstalk and scatter from the anaylzer grating, there are currently no other methods published. There are hardware-based options to reduce the amount of detector crosstalk, e.g. by increasing the walls between pixels in the detector, reducing its efficieny. Also, larger moiré fringe periods on the detector and avoiding discontinuities at grating tiles reduces the effect of detector crosstalk. Grating scatter cannot be avoided, as the grating between patient and detector is necessary for dark-field imaging. It can be reduced by a thoughtful system design, e.g. inserting it with the substrate facing the source as it luckily is in the current setup. However, for both detector crosstalk and scatter from the analyzer grating, these measures can only reduce but not eliminate their effects, and a estimation and subtraction of corresponding intensities may still be necessary even after these measures.

For an even better estimation of intensities due to scatter from the analyzer grating, we could repeat the simulation for different incident beam spectra. Unfortunately, in a real measurement, the exact sample composition and thus also the spectrum of the photons behind the sample is unknown. Another aspect that could be included in the simulation is the phase of the incident intensity pattern, which depends on the sample. This fine intensity pattern has a period similar to the analyzer grating, meaning that the number of photons hitting either grating lamellae or photoresist varies greatly with position. We know the relative position of intensity pattern and analyzer grating from the moiré fringes on the detector. We could conduct a number of simulations with different relative phases and use the phase image to determine the appropriate kernel for every pixel. However, the added value of the spectrum-dependent and phase-dependent approaches would probably be much less than the additional effort in both time and complexity of the correction.

For sample scatter, there are other methods besides estimating and subtracting scattered intensities to reduce its influence in chest radiography. One method is to target the overall amount of scatter generated, by exposure of a smaller portion of the sample at a time [118]. For clinical dark-field radiography, a further reduction of the active grating area and thus the exposed region is not feasible, as this would result in overall longer image acquisition times, meaning the patient would have to stand still and hold breath even longer. Another method is to prevent the scattered photons from reaching the detector by the use of anti-scatter grids. This would further reduce the dose-efficiency of this method. Both these methods can only reduce the sample scatter and not eliminate it [119, 120], in contrast to scatter estimation and subtraction.

For the correction of beam hardening induced dark-field signal, we could also use a theoretical model to calculate the X-ray spectrum $S^{s}\mathbf{E}$ after the sample and use this in combination with the visibility spectrum $V\mathbf{E}$ to calculate the beam hardening induced dark-field signal according to eq. (3.26). To simulate the spectrum after the sample, the attenuation coefficients of the materials could be looked up in e.g. [96], but their thicknesses would need to be estimated from the attenuation image. However, we do not actually know the exact X-ray spectrum and even less the visibility spectrum and material thicknesses in the sample. The data shown in fig. 3.5 are only estimates. Especially the visibility spectrum is hard to measure, and the simulation has never been verified. The spectra displayed in fig. 3.5B and C lead to an overall mean visibility of $V = 45\%$, which is much higher than the average visibility from the reference scans of about $V = 35\%$. This indicates that some effect was not considered correctly in these simulations. This includes

the grating bridges, but maybe also other effects.
Therefore, we chose not to use this option, and instead chose to directly measure the effect. However, this implies that we need to know exactly what we measure, meaning that we have to correct for scatter and ensure that our equivalent absorber materials do not generate a true dark-field signal. Still, measuring the effect has the advantage that we can account for a spatial variation of beam hardening induced artifacts.
A future improvement of the beam hardening correction could be more information to better estimate the material composition in the beam path. This material decomposition could either be achieved in the current setup using the differential phase image, similar to [121], or by spectral imaging, for which setup hardware and image acquisition would need to be adapted.

Other applications of the proposed corrections

The exact scatter and detector crosstalk kernels, as well as the calibration table for beam hardening induced dark-field signal used in this work depend on the used setup, as e.g. the anti-scatter grid properties of the analyzer grating depend on the grating parameters, and overall scatter reaching the detector depends on the beam spectrum and the distances. This means that all measurements and simulations to obtain these corrections will have to be repeated whenever the setup is changed.
For a hypothetical future setup featuring gratings that cover the whole field of view, the overall exposed area on the sample and gratings will increase, leading to even more scatter. The methods to correct for scatter presented in this thesis can still be used. Only if parts of the system are changed, e.g. by a new detector or gratings with different parameters, or if the system geometry changes, the simulations and measurements will have to be repeated. Still, the general concepts behind the scatter corrections presented here are applicable and can be adapted for all grating-based radiography systems. Furthermore, the influence of other scatter contributions which were not addressed in this thesis is much higher in the full-field system. It might therefore be necessary to investigate these scatter contributions further, and maybe even develop corrections for them.
Another setup where the proposed correction methods can be adapted for is the recently presented clinical dark-field CT system [122]. There, sample and grating scatter is currently reduced with an anti-scatter grid on the detector, but otherwise neglected. Detector crosstalk is also neglected. Beam hardening is corrected similarly to the method presented here, but with POM as single equivalent absorber material [123]. A further evaluation of the remaining effects of scatter and crosstalk, and maybe even a beam hardening calibration that uses more than one equivalent absorber material and the three-dimensional image information available could further improve image quality and signal quantitativity.

Overall quantitativity of obtained dark-field radiographs

There are also other processes that influence the measured visibility and corrupt the quantitative dark-field signal. We correct for some of them, as described in section 3.3.7. However, we know that there is the effect of visibility hardening [92], which we do not yet correct for. There could also be further effects that we are not yet aware of.
The residual dark-field signal near the clavicle in the lat image is probably an artifact, since there are no corresponding areas of strong dark-field signal in the pa image. This indicates that at least one of all the applied corrections is not entirely correct, or that there is another, yet undiscovered effect causing a artificial dark-field signal. The high attenuation in this area leads to very little primary intensity, making this area very sensitive to correct scatter and crosstalk estimates. The scatter and crosstalk estimations however are impeded by a relatively large amount of bone in the beam path and the close proximity of a direct beam causing detector saturation. Also, the correction for beam hardening induced dark-field signal could assume too little bone in the beam path in this area. An adaption and optimization of the proposed algorithms for this special case with very high attenuation due to mainly bones and detector saturation could further improve the quantitative results in lateral images.

Conclusion

With the corrections presented here – and other corrections that are not related to crosstalk, scatter or beam hardening – the obtained dark-field signal is due to the micro-structure of the examined tissue, and differences between the dark-field signal of different patients can be attributed to their lung condition rather than artifacts. This ensures a unobstructed qualitative evaluation, and enables a quantitative evaluation of dark-field radiographs.

Chapter 4

Application for COPD Assessment

The content of this section has been published in peer-reviewed journals within three separate publications, describing the qualitative and quantitative characteristics of dark-field images in healthy participants [83], using quantitative dark-field chest radiography for emphysema assessment [80], and comparing its diagnostic value with conventional radiography in a reader study [82].

4.1 Medical Context

COPD is a major contributor to morbidity and mortality worldwide. Main risk factors are tobacco smoking and air pollution [124]. With nearly 5 % of the population, a significant number of people are affected by this condition [125]. COPD usually worsens over time, especially when the risk factors persist, and can ultimately result in death. Prior to that, relevant disability is caused, leading to impaired life quality as well as to high healthcare and economical costs [126]. It is estimated that 3 % of all disability is related to COPD [125].

The disease is induced by a chronic inflammatory process of the airways, causing a degradation of the connective tissue of the lungs. This leads to a destruction of the small airways, impairing the ability to exhale completely, and to a destruction of the alveoli, resulting in pulmonary emphysema [127].

Early diagnosis of this disease is crucial for treatment and smoking cessation programs. However, current widely applied diagnostic tests do not work well for the early stages of this disease.

The diagnostic gold-standard for COPD is spirometry [128], as it measures breathing patterns and provides several parameters representing lung function. However, spirometry shows low sensitivity [129], does not provide localized information, and strongly depends on patient cooperation [130].

CT provides three-dimensional information. Chest CT can visualize density variations in lung tissue and is currently the most accurate imaging technique to assess the in vivo presence, pattern, and extent of emphysema [129, 131]. The visual presence and severity of emphysema is correlated with mortality risk [129]. Chest CT also enables emphysema quantification through classification of lung voxels by attenuation (in HU) [39, 132]. However, attenuation measurements of emphysema are known to vary with patient dose, section thickness, hardware, and reconstruction algorithm [38]. Therefore, only an overall emphysema index (EI) of 6 % or more is considered significant by the Fleischner Society [131].

CT causes a relevant radiation exposure with about 7 mSv for standard chest CT examinations [40]. Even though a significant dose reduction is possible by using low-dose techniques [41], still a radiation exposure of 1.4 mSv to 2.4 mSv is applied [42]. Therefore, CT is not suitable for screening examinations, especially in younger patients.

Conventional radiography is a commonly used first-line imaging modality of the chest, as it is widely available, relatively cheap, and fast [133, 134]. Only a low radiation dose of 0.02 mSv (pa) or 0.1 mSv (pa and lat combined) is reported for this modality [37]. However, early stage diseases may sometimes be difficult to detect with plain radiography due to overlapping anatomy. In particular, the ribs and heart are high-contrast areas and can obscure overlapping lesions or infiltrates. Therefore, conventional radiography offers only very limited sensitivity to the presence of emphysema, especially in cases of mild emphysema [135], and is not recommended for COPD diagnosis [136].

In summary, neither spirometry, CT, nor chest radiography are viable diagnostic modalities for pulmonary emphysema in early stages. Therefore, a new diagnostic method sensitive for lung diseases and dose-compatible with screening applications for early disease detection is highly desirable.

Various studies in animal models have shown that dark-field imaging is particularly useful for lung imaging and that an impairment of the alveolar structure leads to a reduction of dark-field signal [19, 21, 22, 24, 48, 51, 137]. For pulmonary emphysema in particular, dark-field chest radiography showed a strong signal decrease in affected lung areas [20, 23, 50].

In a first study, the clinical system for dark-field chest radiography was introduced, and it was shown that dark-field chest radiography indeed allows for the diagnosis of pulmonary emphysema in COPD patients [33], at about twice the dose of conventional chest radiography [70]. The patient study on the diagnostic value of dark-field chest radiography is ongoing.

The purpose of this work is to investigate the use of dark-field chest radiography for emphysema assessment in more detail. First, the qualitative and quantitative characteristics of dark-field radiographs in healthy human participants will be described. This includes an investigation of the quantitative dark-field coefficient, to check if there are any further dependencies of the dark-field signal besides the lung's alveolar integrity.

Second, the qualitative and quantitative features of dark-field radiographs in participants with pulmonary emphysema will be evaluated, comparing areas of dark-field signal loss with emphysema localization, and showing the decrease of dark-field signal with emphysema severity.

Finally, the diagnostic value of dark-field chest radiography for the detection and staging of pulmonary emphysema will be compared to conventional radiography in a reader study.

4.2 Quantitative Dark-field Radiography

The dark-field signal is measured via a loss of visibility v of the reference pattern (see section 2.2.2). This loss of visibility v follows an exponential law and can be expressed as

$$v = \exp\left(-\int_s \epsilon(\vec{r}) \cdot \mathrm{d}\vec{r}\right) \tag{4.1}$$

in analogy to Beer-Lamberts law for conventional attenuation [138]. Here, s denotes the path of the X-rays through the sample, and $\epsilon(\vec{r})$ is the dark-field coefficient of the tissue at location $\vec{r}$, which depends on setup parameters, but also, more importantly, on the local micro-structure of the sample.

The aim of quantitative dark-field radiography is to retrieve the dark-field coefficient $\epsilon(\vec{r})$ of the investigated sample and thereby gain information on the sample's micro-structural properties. To ensure the dependency of obtained dark-field coefficient on the sample's micro-struture alone, other physical effects contributing to reduced visibility need to be corrected for (see chapter 3).

Assuming a constant dark-field coefficient ϵ along the beam path, the measured dark-field signal D in every pixel depends on both the dark-field coefficient ϵ and the thickness of the sample d on the associated beam path:

$$D = -\ln v = \int_s \epsilon \cdot \mathrm{d}\vec{r} = \epsilon \cdot d. \tag{4.2}$$

For clinical dark-field chest radiography, the sample thickness d for every pixel is unknown, and no direct conversion from the measured dark-field signal to the dark-field coefficient is possible.

However, it is possible to obtain the average dark-field coefficient over the sample if the overall sample volume is known. To do so, we calculate the total dark-field signal and normalize it with the sample volume. The total dark-field is expected to be a measure for the number of interfaces and is given in units of m^2.

The average dark-field coefficient is then calculated as

$$\epsilon = \int_{\text{Sample area}} \frac{D}{\text{Sample volume}} \mathrm{d}A \tag{4.3}$$

It is given in units of m^{-1} and denotes the dark-field signal generated per path length through the investigated sample. This average dark-field coefficient depends on the amount of material interfaces per length. For dark-field chest radiography, we assume that the lung is the only part of the sample generating a dark-field signal. We can then calculate the average dark-field coefficient of the lung by normalizing the total dark-field signal of the dark-field radiograph with the lung volume.

The obtained dark-field coefficient is expected to be proportional to the alveolar density of the lung tissue. Thus, healthy lung tissue with an intact alveolar stucture will have a high dark-field coefficient, while impaired lung tissue, e.g. because of emphysema, will have a lower dark-field coefficient. By evaluating the dark-field coefficient, the influence of different lung thickness and volume due to different patient body types can be eliminated.

4.3 Methods

The purpose of the study was to evaluate the diagnostic value of dark-field chest radiography for COPD assessment. To do so, the overall goal of the ongoing study is to include 250 subjects with and 250 subjects without pulmonary emphysema, respectively. Most of the subjects are included via the radiology department after a medically indicated chest CT. Some are included via the pulmonology department by their pulmonologist, who is familiar with their case. We then perform a number of diagnostic procedures on them, including conventional radiography, dark-field radiography, pulmonary function testing and a questionaire.

In the work presented here, only image-based diagnostic methods are compared, using the chest CT as reference. In these evaluations, we only included participants that had a recent chest CT. In this section, only the parts of the study that were later evaluated will be explained in detail. See [33, 53] for more information on other parts of the study.

4.3.1 Participants

This prospective study was conducted in accordance with the Declaration of Helsinki (as revised in 2013). Approval of the institutional review board and the national radiation protection agency was obtained prior to this study (Ethics Commission of the Medical Faculty, Technical University of Munich, Germany; reference no. 166/20S). Participants gave their written informed consent.

Between October 2018 and October 2020, subjects whe were at least 18 years old and underwent chest CT as part of their diagnostic work-up were screened for study participation. Inclusion criteria were the ability to consent, to stand upright without help, and to hold breath for the duration of the scan, about 7 seconds.

We included participants either without lung impairment or with any stage of pulmonary emphysema, based on their CT. Exclusion criteria were pregnancy and any lung condition other than emphysema, such as fibrosis, cancer, pleural effusion, atelectasis, airspace disease, ground-glass opacities, pneumothorax, masses, or infiltrates.

Eligible subjects were approached immediately after the CT scan. Usually,the study protocoll was performed soon afterwards; the maximum time between CT and study participation was 48 hours. We documented the participant's height, weight, age, and sex.

For the evaluation of the dark-field signal in participants without lung impairment, the CT images from all study participants were further screened by three radiologists (A.A.F., A.P.S., F.T.G.) and were assessed for lung changes. Exclusion criteria for this sub-study were any changes in the lung tissue, including those from emphysema.

Most, but not all, participants underwent chest CT with iodine contrast agent. For sub-study with a quantitative CT analysis, only those with contrast agent were included.

4.3.2 Imaging protocols

Chest CT

All participants underwent clinically indicated CT on one of two CT scanners (iCT and IQon Spectral CT; Philips) according to routine clinical protocols with the following parameters for iCT and IQon Spectral CT, respectively: collimation, 128 mm × 0.6 mm and 64 mm × 0.6 mm; pixel spacing, 0.4 mm and 0.3 mm; pitch factor, 0.8 and 0.9; peak tube voltage, 120 kVp; modulated tube current, 102 mA to 132 mA.

Images were reconstructed with the routine clinical software at 0.9 mm section thickness with a lung-specific convolution kernel, called YA.

Conventional chest radiography

Participants were imaged at a commercial radiography device (DigitalDiagnost, Philips Medical Systems, Hamburg, Germany) in pa and lat orientation, yielding a conventional digital attenuation-based radiograph of the thorax. The effective dose for the reference person in pa orientation at this device is 18 µSv.

Dark-field chest radiography

Dark-field chest radiography was performed with the system described in section 2.2.3. The acquisition was either performed by a radiological technologist or a radiologist. A physicist familiar the the dark-field chest radiography system and the study protocoll was always present to ensure the correct procedures.

The acquisition time was about 7 s, during which the participant is supposed to hold his or her breath. There is an automated voice command instructing the participant to do so. Each image acquisition yields both attenuation-based and dark-field image simultaneously.

All participants were examined with one acquisition each in pa and lat orientations at full inspiration and full expiration, but only images acquired in inspiration were used for further analysis in this work. The effective dose for the reference person for one pa image acquisition is 35 µSv [70]. The effective dose (participant collective median) was 37 µSv for the pa [70] and 46 µSv for the lat images.

Dark-field radiographs were corrected for various effects, including the corrections developed within this thesis (see chapter 3), to obtain quantitatively correct dark-field signal intensities. See section 3.3.7 for details on all performed corrections. Attenuation radiographs underwent standard post-processing (UNIQUE, Philips Medical Systems, Hamburg, Germany) adjusted for this specific system.

4.3.3 Quantitative image analysis

CT images

Emphysema quantification, yielding the EI, was performed using dedicated commercial software (IntelliSpace Portal, version 11.1.1; Philips Medical Systems, Hamburg, Germany). Its working principle has been previously described [39, 132]: Essentially, the lung is segmented from the chest CT data, and a threshold of -950 HU is applied to classify voxels with a lower density as emphysemateous (see fig. 4.1A). The EI is determined by the percentage of emphysematous lung voxels in the whole lung, and thus represents a lung average quantity.

Due to variations of EI with various other parameters such as dose, reconstruction method and CT machine, only an EI of 6 % or more is considered significant according to the Fleischner Society [131]. Below this

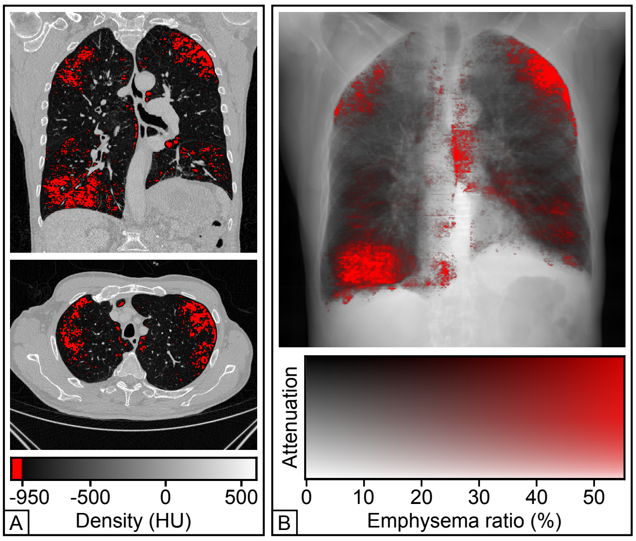

Figure 4.1: Emphysema quantification on a CT scan in a 71-year-old man. **A**, example sections in axial and coronal reformation. All voxels within the lung with less than -950 HU are labeled as emphysematous and colored in red. **B**, overlay of the CT-based attenuation and the emphysema projection, generated by projecting the three-dimensional emphysema map along the sagittal axis. Figure previously published in [80].

value, no definite statement on emphysema presence can be made. Therefore, we assessed the correlation between dark-field coefficient and EI twice, once for all participants and once for only those participants with an EI of 6 % or more.

For visual comparison of quantitative CT results with dark-field images, the three-dimensional CT emphysema map was projected along the sagittal axis, generating an overlay of the CT-based attenuation image and the projected emphysema quantification, as shown in fig. 4.1B. We used a two-dimensional color map, relating the color of each pixel to its quantitative CT emphysema ratio and its brightness to the attenuation. The intensity of the red color increases with the number of emphysematous voxels relative to the total number of lung voxels along the projection of that pixel (i.e. a ray sum) and saturates to maximum red intensity at 50 % or greater.

Dark-field radiographs

As detailed in section 4.2, the dark-field coefficient describes the interface density of the sample, and is expected to have provide diagnostic information regarding the participant's alveolar integrity. Similar to the EI, the dark-field coefficient also represents a quantity averaged over the whole lung.

To calculate the dark-field coefficient of a participant's lung, we need the total dark-field signal and the lung volume. For the total dark-field signal, the integral of the dark-field signal over the lung area was calculated for every participant. The lung area was segmented manually in every radiograph, using both attenuation-based and dark-field contrast. The exact segmentation is not too important here, as the dark-field signal outside of the lung is mostly zero, anyway. However, we want to exclude larger regions with detector saturation, the spine with a little true dark-field signal, and large areas of the diaphragm where the dark-field signal might be negative due to the correction for beam hardening induced dark-field signal assuming a mixture of bone and soft tissue in the beam path.

The total lung volume of the participant was derived from the attenuation-based pa and lat images based on manual segmentation of the lung and surrounding structures, as described previously [139]. The actual segmentation and lung volume calculation was performed in the scope of a Master's thesis at the dark-field chest radiography system [140].

4.3.4 Reader study

CT images

To establish the ground truth on the lung condition of each patient, the CT images were analyzed and graded using the Fleischner Society guidelines for emphysema severity scoring (absent, trace, mild, moderate, confluent, and advanced destructive emphysema) [131]. The three independent radiologists J.H.B., A.P.S., A.A.F. had 4, 7, and 13 years of experience in CT imaging, respectively, and A.A.F. also had subspecialty experience in thoracic radiology. The ground truth was obtained by treating these scores as mono-spaced numbers and taking the median of the three readers.

Conventional and dark-field radiographs

Images from conventional and dark-field radiography were each read by three independent radiologists. Conventional radiographs from the commercial device were read by F.T.G., A.P.S. and D.P., who have 3, 7, and 12 years of experience in radiology, respectively. Both attenuation-based and dark-field radiographs from the dark-field chest radiography system displayed simultaneously were read by F.T.G., A.P.S. and A.A.F., who are experienced in dark-field image interpretation from other studies on animals or cadavers and from previous discussions on dark-field radiography in exemplary patients.

Emphysema detection and severity was rated on a four-point scale (no emphysema, mild emphysema, moderate emphysema, severe emphysema). Dianostic confidence was rated on a six-point scale (0-5). Readers first evaluated all images from dark-field radiography and about a year later those from conventional radiography. Images were shown in random order, with the same window width and level within the modalities. The readers could adjust window settings as they wanted and could return to previous images and change their rating.

4.3.5 Statistical analysis

Statistical analysis was performed using Python libraries, specifically NumPy [141], SciPy [142], and Pandas [143], as well as R [144]. A significance level of 0.05 was chosen for all tests.

Quantitative dark-field signal of healthy lungs

Spearman r correlation statistics were used to test the total dark-field signal for correlation with the lung volume, and to test the dark-field coefficient for correlation with age, weight, and height. Student's-t test was used to compare the dark-field coefficient of men and with that of women.

Quantitative dark-field signal and emphysema severity

Spearman r correlation statistics were also used to test the dark-field coefficient and the CT-based EI for correlation, once for all participants and additionally only for participants with an EI greater than or equal to 6 %. The Wilcoxon Mann-Whitney U test was used to compare dark-field coefficients of groups with different ground truth emphysema severity scores.

A receiver-operating-characteristic (ROC) curve analysis was performed to evaluate the dark-field coefficient as a classifier once for the presence of at least trace emphysema and once for the presence of at least mild emphysema. The Youden index was used to determine optimum cutoff values for either task.

Comparison of conventional and dark-field chest radiography

Fleiss' kappa κ was used to assess inter-reader agreement . Student's t-test was used to test the diagnostic confidence ratings of the two imaging methods for significant differences. Participants were grouped by presence of at least mild emphysema to analyze the capability to detect at least mild emphysema. Data from all readers was pooled together. ROC curves and the respective area under the curve (AUC) values were used to assess the utility of images from either device for prediction of emphysema. Obuchowski's method [145] for correlated and clustered AUC data was used to test AUC values for significant differences.

Additionally, a more detailed analysis was performed regarding the staging of emphysema. Participants were grouped by their ground truth emphysema severity score, and AUC values for differentiation of adjacent groups were calculated. A z-test based on these AUC values was used to determine whether there was a significant difference in the ratings of the adjacent groups.

4.4 Results

4.4.1 Subjects

A total of 88 participants were included, 54 men and 34 women, with a mean age of (64 ± 12) years (standard deviation). Based on their CT-based visual emphysema grades, we included 36 participants with absent, 21 with trace, 11 with mild, 9 with moderate, 7 with confluent, and 4 with advanced destructive emphysema. Due to their small numbers, the groups confluent and advanced destructive were combined for all further analyses. Further demographic details stratified by emphysema severity are listed in table 4.1.

Of these 88 participants, 83 participants (51 men, 32 women) had contrast agent used in their CT scan and were included in the quantitative image analysis. See table 4.2 for further demographic details.

A total of 40 participants (25 men, 15 women) had no lung impairment and were included in the analysis of the dark-field signal characteristics of healthy lungs. Since their status as healthy participants was determined in a earlier, separate reader study (see section 4.3.1), these 40 participants do not match the 36 patients whose Fleischner emphysema severity score was later determined to be "absent". They rather include 25 participants with absent, 14 participants with trace, and even 1 participant with mild emphysema. Further demographic details stratified by gender are listed in table 4.3.

4.4.2 Dark-field chest radiography of healthy lungs

Figure 4.2 shows attenuation-based and dark-field radiographs of four example participants, all without any lung impairment. In attenuation-based radiography, dense structures have a high signal, while in dark-field imaging, the material interfaces generate a high signal. Therefore, on the attenuation-based radiograph lung tissue generates very little signal due to a high air fraction, while it generates a high signal intensity on the dark-field image.

Bony structures have a very high signal intensity on the attenuation-based radiograph (fig. 4.3A), whereas there is no or only very little signal intensity on the dark-field radiograph. The same applies for soft tissue surrounding the lung and to organs of the upper abdomen.

For attenuation-based radiographs, the heart yields a high signal in the area of the lower medial left lung, called heart shadow (fig. 4.3C). In that area, the dark-field radiograph has a lower signal intensity due to less lung tissue along the X-ray beam path (fig. 4.3D). The primary bronchi and the soft tissue and lymph nodes around the hila lead to higher signal compared with the surrounding lung tissue in attenuation-based

	All	Absent	Trace	Mild	Moderate	Confluent or Advanced Destructive
Participants	88	36	21	11	9	11
Men / Women	54 / 34	21 / 15	13 / 8	5 / 6	6 / 3	9 / 2
Age (years)	64 ± 12	62 ± 11	63 ± 12	67 ± 13	65 ± 10	70 ± 9
Weight (kg)	74 ± 15	79 ± 16	74 ± 15	67 ± 11	74 ± 14	67 ± 12

Table 4.1: Demographic characteristics of all participants included in the reader study, grouped by their emphysema severity level. Values are given as mean ± standard deviation. Table adapted from [82].

	All	Absent	Emphysema
Participants	83	35	48
Men / Women	51 / 32	20 / 15	31 / 17
Age (years)	65 ± 12	62 ± 12	66 ± 12
Weight (kg)	74 ± 15	78 ± 15	72 ± 14

Table 4.2: Demographic characteristics of all participants included in the quantitative image analysis, i.e. with a contrast-enhanced CT available. The emphysema group contains all participant with trace, mild, moderate, confluent, or advanced destructive emphysema. Values are given as mean ± standard deviation. Table adapted from [80].

	All	Men	Women
Participants	40	25	15
Age (years)	61 ± 12	61 ± 13	59 ± 11
Weight (kg)	79 ± 15	82 ± 16	73 ± 13
Height (cm)	170 ± 7	173 ± 5	164 ± 6

Table 4.3: Demographic characteristics of all participants included in the analysis of the dark-field signal of healthy lungs, i.e. all participants without any lung impairment. Values are given as mean ± standard deviation. Table adapted from [83].

imaging (fig. 4.3E). Because of the reduced amount of lung tissue in the respective beam path, the dark-field radiograph shows a lower signal intensity compared with the surrounding lung tissue (fig. 4.3F).

In general, the dark-field radiograph displays a higher signal intensity in the lower lung field on both sides compared with the upper lung fields (fig. 4.3B).

Correlation with body parameters

The total dark-field signal of all participants covered a wide range from $8.5 \times 10^{-3}\,\mathrm{m}^2$ to $28 \times 10^{-3}\,\mathrm{m}^2$. The total dark-field signal of showed a positive correlation with the lung volume over all participants ($r = 0.61$, $p < 0.001$, fig. 4.4A) and for women only ($r = 0.53$, $p = 0.04$). No correlation was found for men only ($r = 0.37$, $p = 0.07$).

The average dark-field coefficient was $(2.5 \pm 0.4)\,\mathrm{m}^{-1}$ (mean ± standard deviation) over all participants. No correlation was found between dark-field coefficient and age ($r = -0.27$, $p = 0.09$; fig. 4.4B). Also, no difference was found between men ($(2.5 \pm 0.4)\,\mathrm{m}^{-1}$) and women ($(2.6 \pm 0.4)\,\mathrm{m}^{-1}$, $p = 0.37$, fig. 4.4C). There was no correlation found between dark-field coefficient and height ($r = -0.13$, $p = 0.44$; fig. 4.4D). There was a correlation between dark-field coefficient and weight ($r = 0.36$, $p = 0.02$, fig. 4.4E).

4.4.3 Dark-field chest radiography for pulmonary emphysema

Figure 4.5 shows attenuation-based and dark-field chest radiograph from the dark-field chest radiography system and emphysema projections from CT scans of six example participants, all with an significant EI above 6 %. In attenuation-based chest radiographs, participants with pulmonary emphysema often have secondary signs of hyperinflation such as flattened diaphragms and a barrel-shaped lung. In dark-field chest radiographs, participants with pulmonary emphysema exhibit an overall reduced signal intensity and a rather inhomogeneous patchy appearance compared with the homogeneous high signal intensity seen in healthy participants (fig. 4.2). The areas of reduced dark-field signal intensity correspond well to the areas of emphysema detected on the CT-based emphysema projections.

Figure 4.6 shows results for participants with an inconclusive emphysema index below 6 %. The signal reduction in dark-field radiographs shows again correspondence with the emphysema pattern on CT-based emphysema projections, even though these emphysema quantifications are not yet considered significant.

Correlation with emphysema severity

The dark-field coefficient was negatively correlated with the CT-based emphysema index for all participants ($r = -0.54$, $p < 0.001$) and evaluating only those participants with an emphysema index greater than or equal to 6 % ($r = -0.79$, $p < 0.01$) (fig. 4.7A).

The dark-field coefficient of the trace emphysema group was similar to that of the group without emphysema ($p = 0.34$). In the other Fleischner-grade emphysema groups, the dark-field coefficient was signifcanlty lower (fig. 4.7B, table 4.4).

The AUC was 0.68 for detection of at least trace emphysema and 0.79 for detection of at least mild emphysema (fig. 4.7C). The optimum cutoff value

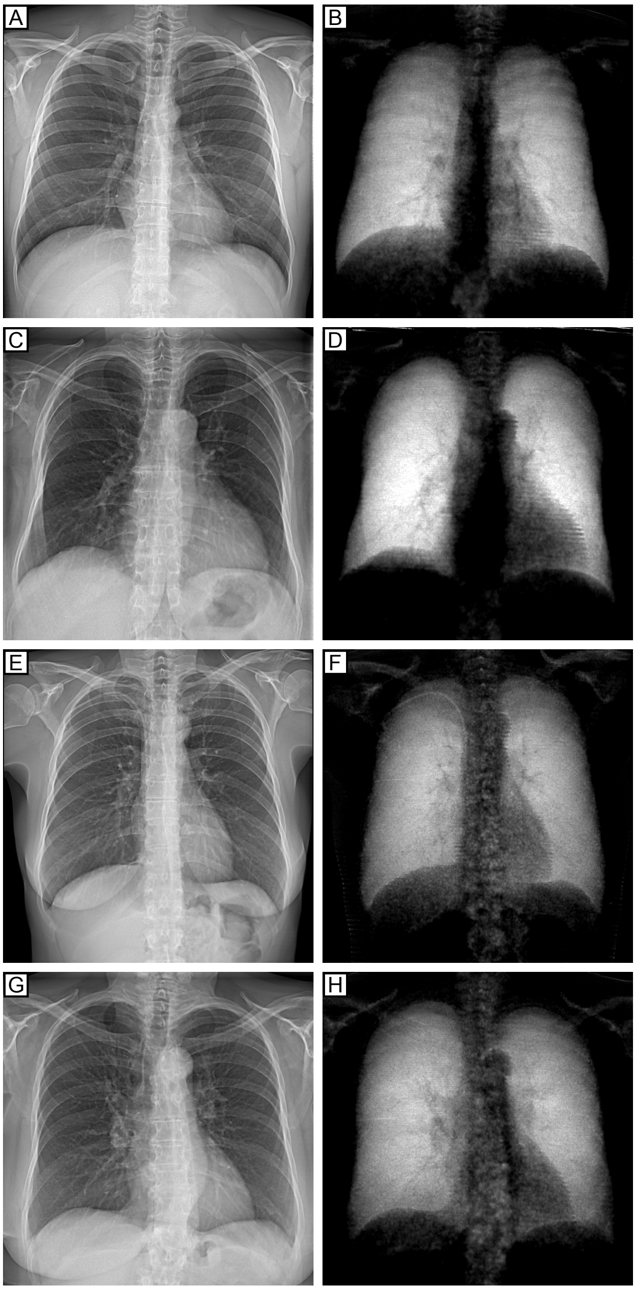

Figure 4.2: Comparison of attenuation-based and dark-field radiographs of the thorax for example participants without lung impairment. **Left**, attenuation-based, and **right**, dark-field pa radiographs. **A** and **B**, 33-year-old man. **C** and **D**, 54-year-old woman. **E** and **F**, 42-year-old woman with a right-sided port catheter in place. **G** and **H**, 79-year-old woman. While attenuation-based images show anatomical structures such as bones and the soft tissue, dark-field images show the amount of tissue interfaces in the beam path. Figure previously published in [83].

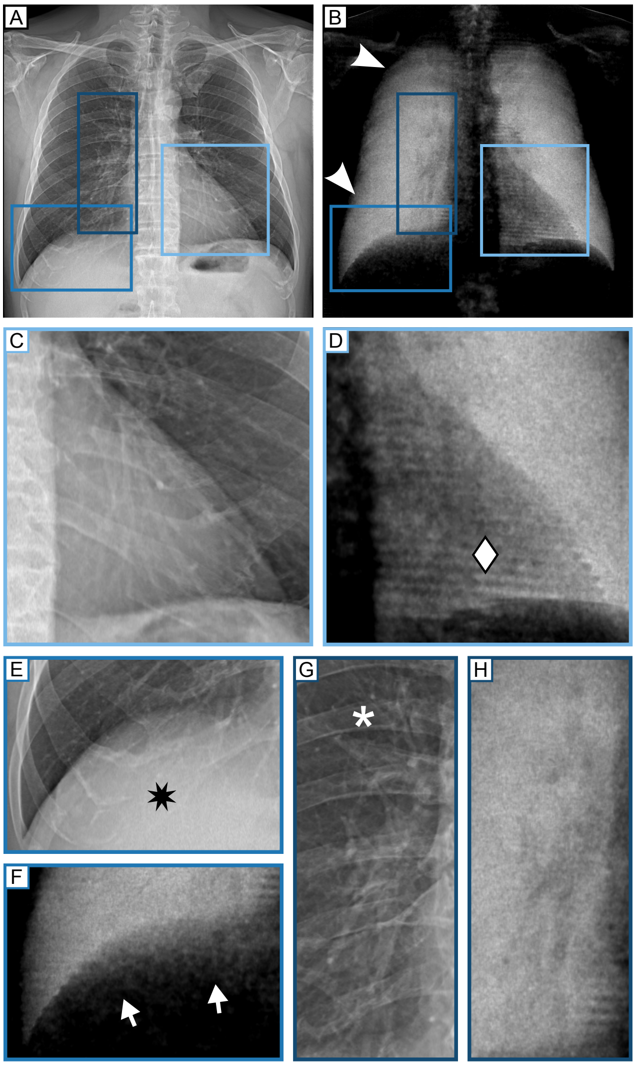

Figure 4.3: Details for comparison of attenuation-based and dark-field radiographs. **A** and **B**, attenuation-based and dark-field radiographs of the thorax in a 61-year-old man without lung impairments. **C**-**H**, magnifications of different regions indicated in **A** and **B**. Because of larger lung thickness, lower lung areas appear brighter compared with upper lung areas (arrowheads in **B**). The heart appears bright on the attenuation-based image (**C**) but generates hardly any dark-field signal; therefore, dark-field images allow for an overlay-free assessment of lung tissue behind the heart (◇ in **D**). The same applies to the upper abdominal organs that obscure the lung tissue behind the diaphragm (⋆ in **E**, arrows in **F**). The hilar region, including bronchi, blood vessels, and lymph nodes, appears bright on attenuation-based images (**G**), and the dark-field signal intensity decreases in this area (**H**). Also, osseous structures such as the ribs ($*$ in **G**), claviculae, and scapulae generate an attenuation signal and overlay the lung in several areas (**A** and **G**). On dark-field images, these structures generate hardly any signal (**B**, **H**). Figure previously published in [83].

in dark-field coefficients, below which a participant was classified as having at least trace emphysema was $2.4\,\mathrm{m}^{-1}$. For mild emphysema, it was lower with $2.3\,\mathrm{m}^{-1}$. The corresponding Youden index was $J = 0.38$ for trace emphysema detection and $J = 0.51$ for mild emphysema detection.

Applying those cutoff values for the detection of at least trace emphysema, sensitivity, specificity, and accuracy were 0.69, 0.69, and 0.69, respectively. For the detection of at least mild emphysema, sensitivity, specificity, and accuracy were 0.78, 0.73, and 0.75, respectively.

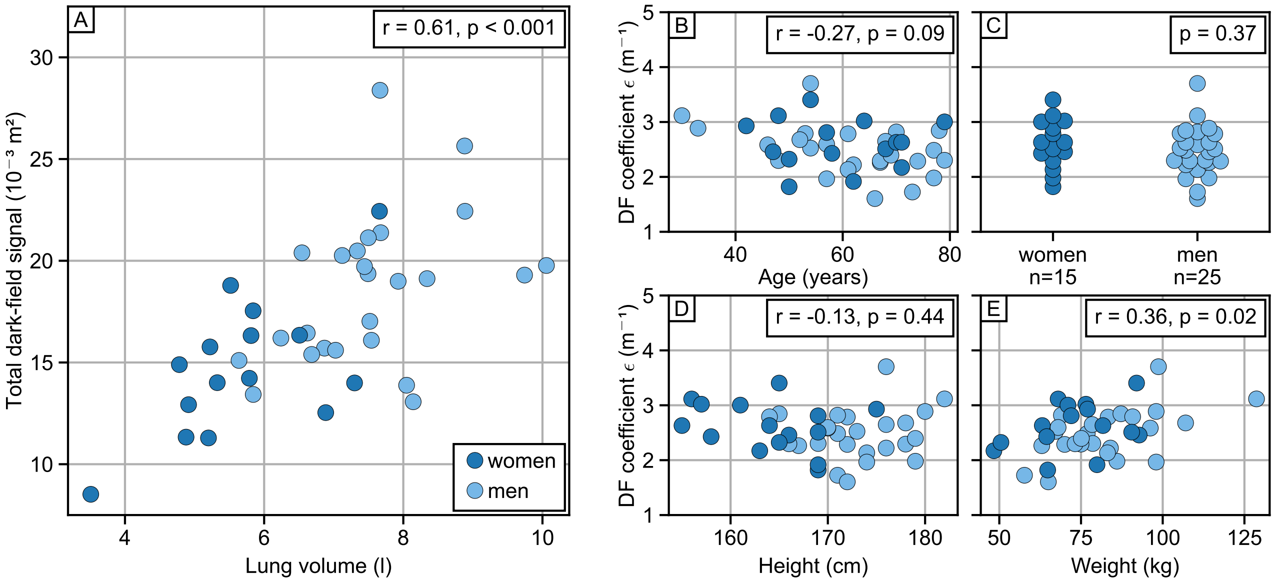

Figure 4.4: Statistical analysis of the dark-field signal of 40 participants without lung impairment (25 males, orange dots; 15 females, blue dots). **A**, correlation of the total dark-field signal with the lung volume over all participants. **B**, **C**, **D**, and **E**, correlation of the dark-field coefficient with the demographic participant parameters age, sex, height, and weight, respectively. The only demographic parameter we found a significant correlation with is the participant's weight. The dark-field coefficient was obtained by normalizing the participant's total dark-field signal with the their lung volume. Abbreviation: DF, dark-field. Figure previously published in [80].

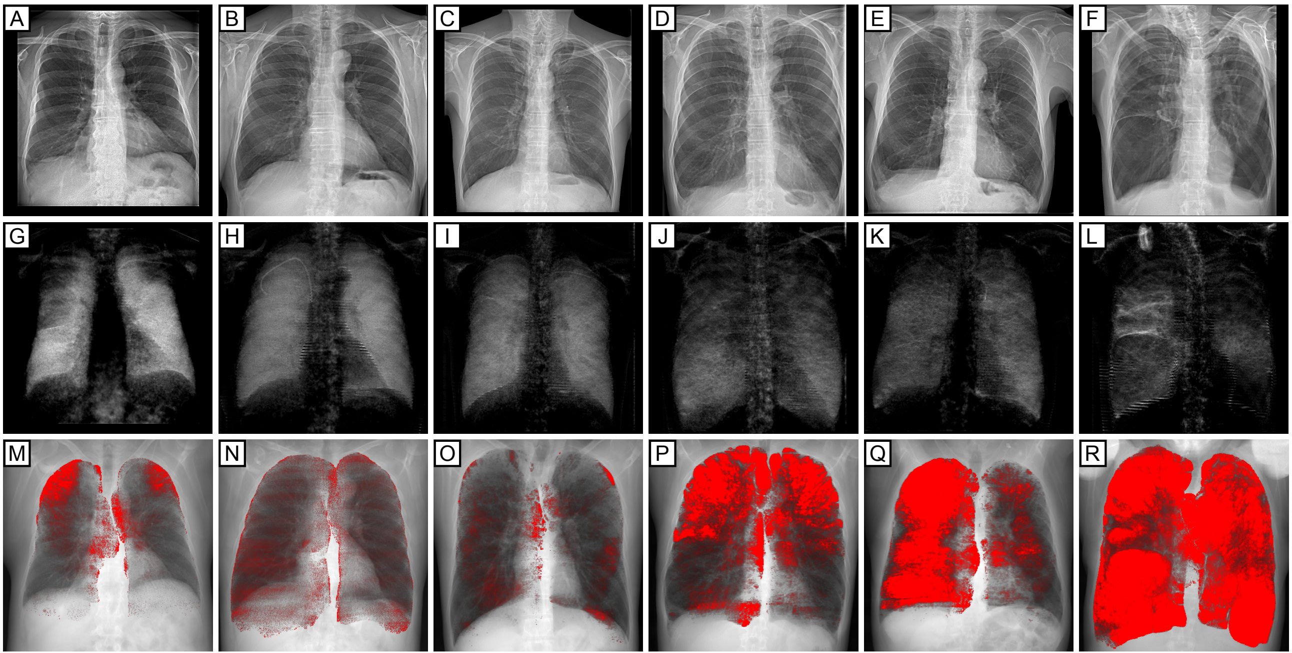

EI = 11 % EI = 14 % EI = 9.0 % EI = 26 % EI = 36 % EI = 51 %

Figure 4.5: Comparison of dark-field radiography and CT-based emphysema assessment for participants with a significant emphysema index of 6 % or more. **Top row**, attenuation-based, **middle row**, dark-field radiographs, and **bottom row**, projections of CT-based emphysema quantification in six example participants. Signs of hyperinflation can be observed in attenuation-based images of participants with high emphysema severities. Areas of decreased dark-field signal correspond well to emphysematous areas on the CT-based emphysema projections. The participant in **B**, **H**, and **N** has a right-sided port catheter in place. Images previously published in [80].

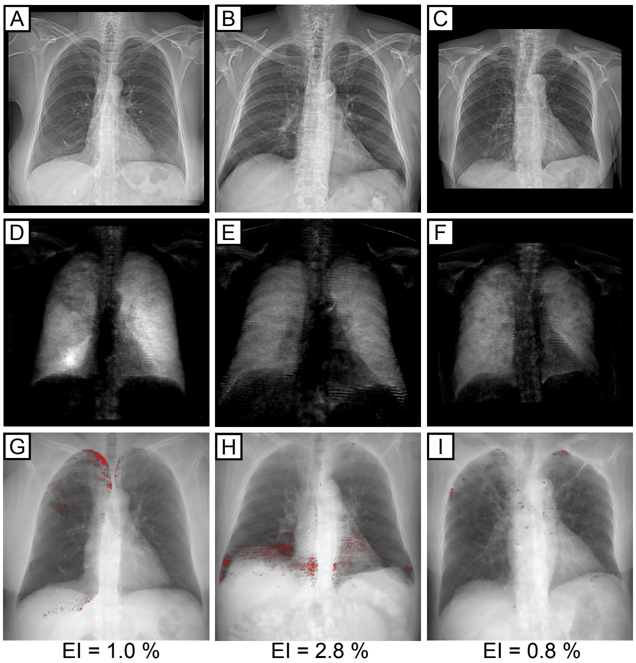

Figure 4.6: Comparison of dark-field radiography and CT-based emphysema assessment for participants with a non-significant emphysema index. **Top row**, attenuation-based, **middle row**, dark-field radiographs, and **bottom row**, projections of CT-based emphysema quantification in three participants with an emphysema index (EI) below 6 % but a decreased, inhomogeneous dark-field signal intensity. Images previously published in [80].

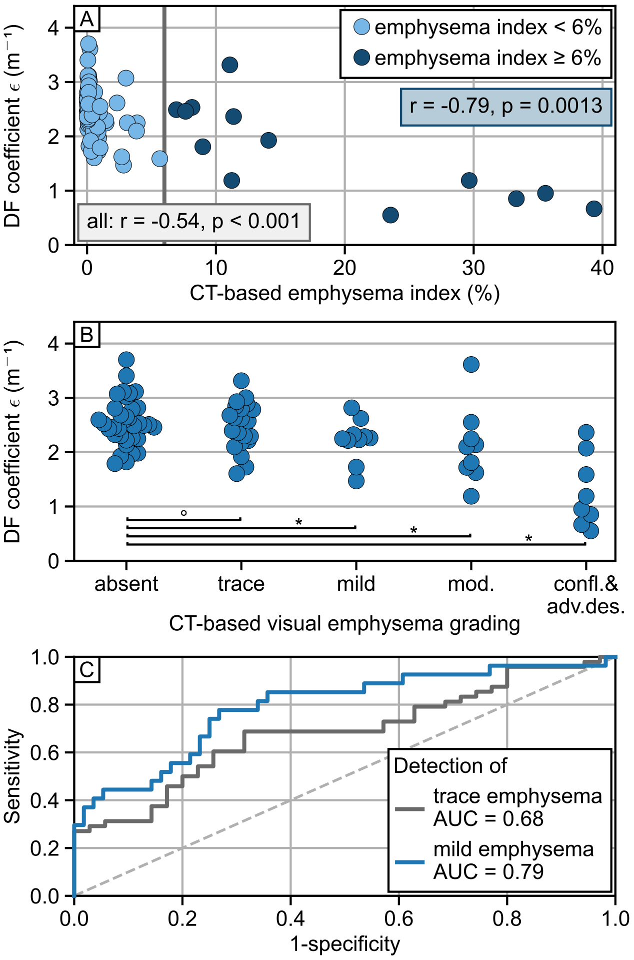

Figure 4.7: Comparison of dark-field coefficient and CT-based emphysema evaluation of 83 participants. **A**, comparison of dark-field coefficient with the emphysema index (EI) from quantitative CT evaluation. **B**, comparison of dark-field coefficient and visual emphysema severity scores determined from CT assessment according to the Fleischner scale. The symbols indicate the significance of p values from Wilcoxon Mann-Whitney U tests of each group with the absent group: °, $p > 0.05$, *, $p < 0.05$. **C**, ROC curve showing the capability of the dark-field coefficient to detect at least trace emphysema and at least mild emphysema. Abbreviation: DF, dark-field. Figure previously published in [80].

4.4.4 Comparison of conventional and dark-field chest radiography

Figure 4.8 shows exemplary conventional radiographs from the commercial system and attenuation-based and dark-field images acquired with the dark-field chest radiography system of five participants with increasing emphysema severity. As expected, the conventional chest radiographs and the attenuation-based radiographs from the dark-field chest radiography system look quite similar. Their main difference is a lower contrast of bones in the conventional images due to the higher tube voltage (120 kVp in conventional vs 70 kVp in dark-field radiography) and a different post-processing for contrast enhancement. A more detailed study on image features of conventional attenuation radiographs and attenuation-based radiographs from the dark-field chest radiography system was performed in a Master's thesis at the dark-field chest radiography system [146, 147].

In both conventional radiographs and attenuation-based radiographs from the dark-field chest radiography system, emphysema can mainly be diagnosed based on secondary symptoms such as the flattened diaphragm or the barrel shape of the lung in more severe emphysema stages (fig. 4.8D, E, I, J). A diagnosis based on a decreased density is only possible in advanced stages of COPD in which these secondary signs are also present.

The dark-field images on the other hand are sensitive to the destruction of the alveoli in emphysema. Thus,

Emphysema group	#	Dark-field coefficient (m^{-1})	P-value
absent	35	2.6 ± 0.4	
trace	21	2.5 ± 0.4	0.68
mild	10	2.2 ± 0.4	0.037
moderate	9	2.1 ± 0.7	0.015
confluent or adv. destr.	8	1.3 ± 0.6	<0.001

Table 4.4: Statistical evaluation of dark-field coefficients for the different emphysema severity groups. Groups were tested for differences from the absent emphysema group using the Wilcoxon Mann-Whitney U test. Abbreviations: #, Number of participants; adv. destr., advanced destructive. Values are given as mean ± standard deviation.

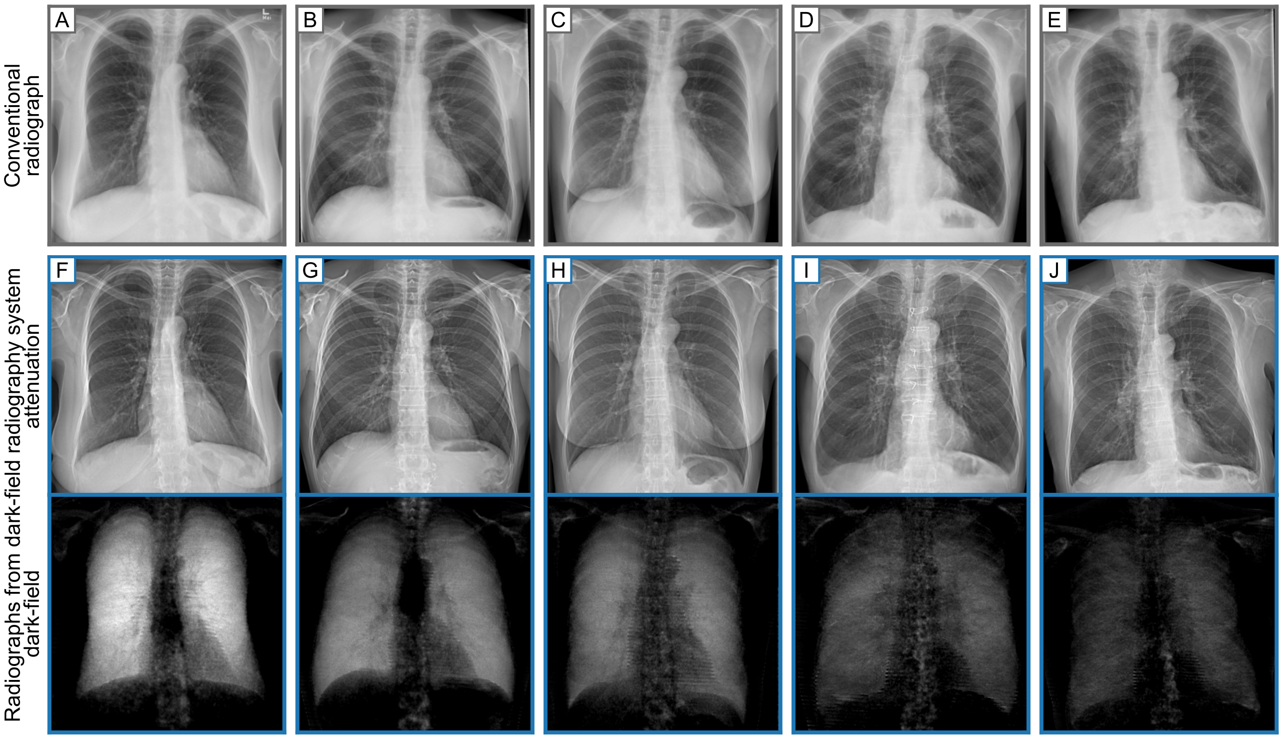

Figure 4.8: Comparison of conventional and dark-field chest radiography for five participants with increasing CT-based visual emphysema scores on the Fleischner scale. **A**-**E**, conventional attenuation-based chest radiographs from the commercial system. **F**-**I**, attenuation-based and dark-field chest radiographs from the dark-field chest radiography system. **A** and **F**, 64-year-old woman without emphysema. **B** and **G**, 57-year-old man with trace emphysema. **C** and **H**, 54-year-old woman with mild emphysema; **D** and **I**, 71-year-old man with moderate emphysema; **E** and **J**, 73-year-old man with confluent emphysema. Same window and level were applied within all images of each modality. The dark-field radiographs are directly sensitive to the lung's alveolar structure, and the dark-field signal strength is decreased in emphysematous lungs (**H**, **I** and **J**). Images previously published in [82].

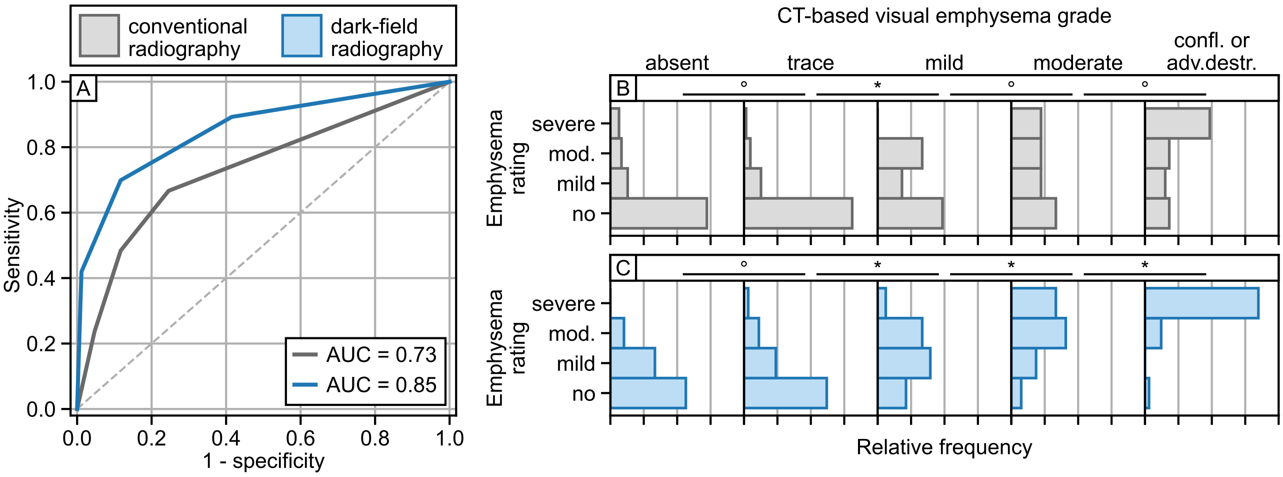

Figure 4.9: Statistical analysis of reader study. **A**, ROC-curves and corresponding AUC values for the detection of at least mild emphysema for images from both devices. **B** and **C**, a more detailed analysis regarding the staging of emphysema. AUC values indicating significant differentiation of the groups are printed in bold. While readers were only able to differentiate between trace and mild emphysema based on conventional radiography, with use of the dark-field radiography a differentiation was possible between trace, mild, moderate, and confluent emphysema. The legend applies to all panels. Abbreviations: mod., moderate; confl., confluent; adv. destr., advanced destructive. Parts of the data in this figure were previously published in [82].

	Conventional radiography		Dark-field radiography	
	AUC	*P*-value	AUC	*P*-value
absent / trace	0.47	0.85	0.49	0.55
trace / mild	0.68	<0.001	0.72	0.002
mild / mod.	0.62	0.10	0.72	0.011
mod. / confl. or adv. destr.	0.65	0.055	0.76	<0.001

Table 4.5: Statistical evaluation of the reader study on differentiation of emphysema severity groups. Adjacent Groups were tested for differences using an AUC-based z-test. Abbreviations: AUC, area under the curve; mod., moderate; confl., confluent; adv. destr., advanced destructive. Parts of this table have been previously published in [82].

while the healthy lungs with intact alveolar structure exhibit a strong dark-field signal (fig. 4.8F and fig. 4.2), lungs affected by – even mild – emphysema show a much lower dark-field signal (fig. 4.8H, I, J), where the signal decrease is a measure for emphysema severity.

Reader study

Values are given as mean ± standard deviation. The diagnostic confidence of all readers increased significantly ($P < 0.001$) from 2.78 ± 0.96 for conventional radiographs to 4.30 ± 0.71 for dark-field and attenuation radiographs from the dark-field chest radiography system. There was slight inter-reader agreement for emphysema severity with conventional images ($\kappa = 0.12$), and fair agreement for assessment of images from the dark-field chest radiography system ($\kappa = 0.39$).

Figure 4.9A shows the ROC curves for the performance of both imaging methods regarding the detection of at least mild emphysema. The increase in emphysema detection capability from conventional radiography (AUC = 0.73) to dark-field chest radiography (AUC = 0.85) was significant ($P = 0.005$).

Figure 4.9B and C and table 4.5 provide a more detailed analysis of the reader study regarding the staging of the emphysema. For images from both devices, the readings were not significantly different between absent and trace emphysema. Based on the conventional radiographs (fig. 4.9B), readings were different between trace and mild emphysema, but were not significantly different between mild and moderate emphysema, moderate and confluent emphysema, as well as between confluent and advanced destructive emphysema. When readers had attenuation-based and dark-field radiographs from the dark-field chest radiography system (fig. 4.9C) available, however, readings were significantly different between trace and mild emphysema, mild and moderate emphysema, and moderate and confluent emphysema.

4.5 Discussion

This chapter shows the qualitative and quantitative characteristics of dark-field radiographs of participants without lung impairments and of COPD patients, and evaluates the diagnostic value of dark-field chest radiography for emphysema assessment.

Context

Dark-field imaging with X-rays has first been introduced in 2008 [9]. Ever since, it has been evaluated in multiple ex vivo and in vivo approaches, including both healthy models and various disease models. Dark-field radiography and CT has been shown to be beneficial for the diagnosis of pulmonary fibrosis [21, 23], acute lung inflammation [148] and lung cancer in mice [24]. Furthermore, it was shown that dark-field imaging allows for the early detection of radiation-induced lung damage [149]. For pulmonary emphysema, the disease investigated in this thesis, extensive studies in animals showed the diagnostic potential of dark-field radiography [20, 48–50].

In the last years, research has been focused towards clinical application of dark-field imaging. Together with this one, two other PhD theses at this Chair have been working on clinical dark-field chest radiography [53, 68]. Konstantin Willer developed the clinical dark-field chest radiography system and showed a first application for emphysema patients [53]. Manuela Frank worked on patient exposure and dosimetry, and applied dark-field chest radiography for patients suffering from Covid-19 [68].

For reference on emphysema staging, we used CT-based visual emphysema scores as the underlying imaging gold-standard. The diagnostic goal to differentiate of the CT-based visual emphysema scores is of high relevance. These CT-based visual emphysema scores have been shown to be an independent predictor of subsequent progression of emphysema in participants who are current or former tobacco smokers with and without COPD [150]. For early stages of emphysema, the score is based mainly on small, localized changes in the lung parenchyma. With the projection in radiography, these changes in lung density are overlaid with the signal from other tissues in the beam path, such as bones and soft tissue, impeding the diagnostic power of conventional radiography. As the dark-field signal originates from the lung's alveolar structure itself, and other tissues generate no or very little signal, the assessment of structural changes in the lung parenchyma is expected to be much easier. When emphysema is found in CT, mortality is increased in a general population without a significant smoking history or a clinical disease [151], and in smokers, even if there is no obstruction found in spirometry [129, 152]. For smokers especially, an early detection is crucial to be able to start preventive interventions, such as smoking cessation or other risk factor modifications. Furthermore, an early detection of emphysema could also be beneficial in the general population.

Qualitative image analysis

The appearance and features of X-ray dark-field radiographs in humans are introduced and described in detail. Due to the inherent signal generation in dark-field imaging and the corrections established in chapter 3, bone structures and soft tissue generate none or only a much smaller dark-field signal than lung tissue. This property allows for a detailed depiction of lung tissue without impairment by surrounding or overlaying structures.

The higher dark-field signal in the upper compared to the lower lung areas can be attributed to both regionally different lung thickness and alveolar density [153], and are consistent with previous pre-clinical studies [30, 31].

Compared with images in healthy participants, dark-field chest radiographs in participants with emphysema had lower dark-field signal intensity and an inhomogeneous patchy appearance of the lungs. The locations of lower dark-field signal dark-field radiographs corresponded well with emphysematous areas found on CT images.

In the presented reader study on COPD patients and participants without lung impairments, dark-field radiography clearly outperformed conventional radiography for the diagnosis and staging of pulmonary emphysema, with a significantly higher capability for detection of at least mild emphysema with dark-field chest radiography (AUC = 0.85) than with conventional radiography (AUC = 0.73). This finding is not only of great interest for the early detection of pulmonary emphysema and its predominant corresponding disease COPD, it also highlights the potential of dark-field chest radiography for lung imaging in general.

Quantitative image analysis

Furthermore, the dark-field coefficient is introduced for a quantitative evaluation of dark-field chest radiographs. The dark-field coefficient is calculated from the total dark-field signal in the radiograph, normalized by the lung volume.

The variation of the total dark-field signal between different patients without lung impairment can be attributed to different lung sizes and therefore different number of alveoli present in the lung [73]. Therefore, rather than evaluating the total dark-field signal alone, the dark-field coefficient obtained by normalizing with the lung volume should be used for further quantitative evaluations regarding the health status of the lung. This dark-field coefficient is expected to differ between participants with and without lung impairments, as it depends on the alveolar density alone. To test these hypotheses, the dark-field coefficent is first evaluated in participants without lung impairments only. We found that it is independent of the participant's demographic parameters sex, age, and height, while it is unfortunately influenced by the participant's weight.

A potential explanation could be found in the positioning of the participant during dark-field imaging. Participants are asked to lean on to the patient contact plane with their upper body. Participant weight presumably goes along with greater upper body diameter, and the distance between the participant's lung and analyzer grating G_2 is thus expected to be greater in heavier patients. Since the setup's dark-field sensitivity increases with distance from the analyzer grating G_2 [114], the positioning might lead to a higher dark-field signal in heavier patients. In future dark-field radiography systems, this behaviour might be prevented either by using a different positioning method, such as a fixed position on the floor to stand on, or by measuring the participant position and correcting vor variations.

The decrease of dark-field coefficient with age is not significant. Still, it might suggest a smaller amount of intact alveoli in older participants, implying a decrease of healthy lung tissue with age. This finding is in accordance with a study suggesting that increased air space is associated with advancing age in adult lungs [154] and another study suggesting an alveolar wall thickening in older participant's lungs [155].

In a second step, the dark-field coefficient is analyzed regarding its value for emphysema assessment, again using CTs for reference. We found a significant correlation between dark-field coefficient and CT-based quantitative emphysema evaluation, i.e. the emphysema index, as well as lower dark-field coefficient in participants with Fleischner Society emphysema grades of mild, moderate, and confluent or advanced destructive compared with participants without pulmonary emphysema. This suggests that quantitative evaluation of dark-field chest radiography may be a useful tool in the assessment of pulmonary emphysema. Especially for the detection of mild emphysema, the ROC curve analysis showed that the dark-field coefficient may be a useful quantitative measure (AUC = 0.79).

For detection of the earlier stage trace emphysema, specificity was lower due to a large variation in dark-field coefficients and the large overlap of dark-field coefficient in the absent and trace groups. Similarly, the dark-field coefficients of participants with an emphysema index below 6 % covered a wide range. This could either be due to an actually wide range of alveolar densities in these patients, or due to other factors which we do not yet take into account. One of these could be the correlation of dark-field coefficient with patient's weight via patient positioning.

Diagnostic value of dark-field radiography

With conventional radiography, no quantitative evaluation regarding lung assessment is established, mainly due to overlaying tissue with high attenuation. Instead, conventional radiographs are post-processed to have the highest information yield for visual assessment by radiologists.

In this study, when the readers evaluated conventional chest radiographs, the distribution of ratings differed between participants with trace and mild emphysema – other adjoining stages did not show significant differences in rating distributions. For more severe stages (moderate, confluent, advanced destructive) the ratings did differ from those of participants with trace emphysema.

Dark-field radiography generates perfectly aligned attenuation-based and dark-field radiographs from one acquisition. Because the attenuation image shows the attenuating anatomic structures and the dark-field image gives information on the alveolar integrity, information from the two complementary modalities, acquired within one image aqcuisition, improves the accuracy of emphysema assessment compared to analysing the conventional images alone.

Thus, dark-field chest radiography yields better results than conventional radiography for the detection of early stages of emphysema. Adjoining stages trace and mild, mild and moderate, and moderate and confluent of advanced destructive showed differences in rating distribution, with higher effect sizes than for conventional radiography. The more severe emphysema stages are often also visible on conventional radiographs due to secondary changes, such as flattening of the diaphragm. However, patients in advanced stages often already have other symptoms such as shortness of breath or fatigue. This limits the value of conventional radiography to excluding other diagnoses responsible for the symptoms. The advantage of dark-field radiography in these stages is mainly the possible localization of emphysematous changes.

As CT-detected trace emphysema could not be differentiated statistically significantly from absent emphysema using dark-field radiography, the sensitivity of dark-field radiography seems to be slightly lower than for CT-based emphysema detection. This might be simply because the readers in the presented study evaluated emphysema on a four-point scale (no/mild/moderate/severe emphysema). For differentiation of earlier stages, it might be beneficial to provide a more detailed rating scale. Additionally, the current study is based on the first patients ever receiving dark-field radiography for emphysema detection. Thus, an increasing sensitivity can be assumed as the radiologists' experience in dark-field radiography improves and upcoming dark-field scanners provide higher image quality.

Furthermore, dark-field radiography allows a quantitative image evaluation, possibly yielding more objective results at lower work load. However, the AUC-values for the detection of at least mild emphysema with dark-field radiography were higher when evaluated by radiologists than with the dark-field coefficient. This could be due the dark-field coefficient being averaged over the whole lung, since we can only estimate lung volume but not lung thickness for now. Localized changes in the lung might therefore not lead to an overall change in dark-field coefficent.

Recently, Manuel Schultheiss, another PhD at this Chair, used a convolutional neural network (CNN) to estimate lung thickness from chest radiographs [156]. A Master's thesis at the dark-field system applied the established CNN to estimate lung thickness from the attenuation-based radiograph from our system and used that to get local dark-field coefficients [157]. This promising approach will have to be evaluated in further quantitative studies and reader studies. It might provide a more sophisticated and powerful quantitative analysis of dark-field radiographs.

Comparison of diagnostic value with patient dose

One posteroanterior dark-field image acquisition exposes the patient to 0.037 mSv of radiation [70]. At that low dose, it provides a fairly high diagnostic value with AUC $= 0.78$ for quantitative and AUC $= 0.85$ for qualitative image analysis for detection of mild emphysema, with the CT-based Fleischner grading as the reference standard.

The dose at the dark-field chest radiography system is substantially less (about 2 %) than low-dose chest CT [42]. Even for recently reported ultra-low-dose CT using deep-learning based image reconstruction [158], radiation exposure was with 0.39 mSv more than ten times higher than the reference dose for the dark-field chest radiography system.

The radiation dose will probably be even lower in commercially available dark-field systems compared to the current system. Dark-field radiography could then be used for clinical routine chest X-rays (e.g. obtained for pre-operative screening, trauma or pneumonia). Considering that dark-field radiography can detect emphysema in early stages, emphysema could be detected in more patients, making interventions or further diagnosis possible. Additionally, follow-up examinations for emphysema could be possible given the low radiation exposure of dark-field radiography.

Spirometry is often used in daily clinical routines and does not apply any dose. However, it crucially depends on the operator and cooperation of the patient [159], and therefore has a low sensitivity for detection of mild emphysema. In a recent study, 23 % of smokers without spirometric impairment had at least mild emphysema at CT [129]. Dark-field radiography was able to detect mild emphysema with a much higher sensitivity; thus, dark-field radiography might close this diagnostic gap and allow the detection of emphysema in early stages at a comparably low dose. In contrast to spirometry, dark-field radiography additionally provides an image for emphysema localization.

Limitations

Much like attenuation-based radiographs exhibit a different appearance for different setup paramaters, e.g. tube voltages, dark-field radiographs also depend on the specific setup parameters, namely the geometry of the interferometer. Whereas the general trends found in these studies should still apply, quantitative values for the dark-field coefficients will be different for different setups. However, as long as setup parameters are identical, dark-field radiography allows for a quantitative comparison between individuals.

The main limitation of the presented studies is the small number of participants, especially in the higher emphysema stages. The results will have to be confirmed with larger cohorts, preferentially also at other institutions, in the future.

Another limitation is the restriction to emphysema as the only lung pathology, and only different stages of emphysema had to be differentiated. Therefore, the specificities reported in the presented studies are only valid for the comparison of healthy and emphysematous lungs. However, a decreased dark-field signal can also be caused by other pathologies such as pneumonia [81] or masses. In these cases, the attenuation-based images could be used to differentiate between emphysema and other causes. Further studies including other pathologies of the lung, such as pneumonia, fibrosis, or pneumothorax, will ne necessary to investigate the specificity of dark-field chest radiography for differentiation between different lung diseases or conditions.

Finally, very early stages of emphysema could be missed using CT for reference. As patients without evidence of emphysema in the CT examination were rated as healthy, an evaluation of these stages was not possible.

Conclusion

In conclusion, this chapter introduces the qualitative and quantitative characteristics of X-ray dark-field chest radiography in participants without lung impairments and in COPD patients. Pulmonary emphysema leads to a reduced signal intensity on dark-field chest radiographs. Further, dark-field chest radiographs are superior to conventional radiographs for emphysema diagnosis and quantification.

Thus, dark-field chest radiography may be suitable for early detection of emphysema and could be used for long-term treatment or disease progression monitoring.

This work reveals the potential of X-ray dark-field radiography for imaging of the lung in general, for the diagnosis of COPD and possibly other lung diseases that alter the alveolar interfaces in the lung.

Chapter 5

Conclusion

The aim of this thesis was to increase and evaluate the diagnostic value of dark-field chest radiography, and thereby promote its clinical application for lung assessment.

Summary

The recently installed clinical dark-field chest radiography system is used throughout this work.
In the first part of this thesis, image quality and quantitative accuracy are improved by investigating image artifacts and establishing corrections for them. Besides the well-known sample scatter it is demonstrated that also X-ray scatter generated by the interferometer as well as detector crosstalk create artifacts in the dark-field radiographs.
For the induced artifacts due to crosstalk and scatter, deconvolution-based correction methods are established. The kernel for detector crosstalk is measured and fitted to a model. For the kernel for scatter from the analyzer grating, the dark-field chest radiography system is implemented in a Monte-Carlo simulation. To estimate scatter from the sample, we use an adapted algorithm originally developed for scatter correction in conventional radiography. The estimated scatter and crosstalk intensities are validated with a variety of simulations and measurements. Detector crosstalk and scatter from the analyzer grating have relatively narrow kernels and corrupt the dark-field signal mainly in regions with a high variance in attenuation. Scatter from the sample has a much larger range, and its biggest impact is wherever the overall attenuation is high.
Another effect leading to artifacts in dark-field radiography is beam hardening. To characterize this effect at our dark-field chest radiography system, calibration measurements with different materials that generate no true dark-field signal but attenuate similarly to materials in the human body are conducted. We find that POM, which is often used as an equivalent absorber material for soft tissue, cannot be used for this calibration, as it itself generates a true dark-field signal. This cannot be distinguished from beam hardening induced dark-field signal, and leads to wrong corrections. This finding is highly relevant for our system as well as many other dark-field imaging systems.
In the light of these results, we choose to use water as equivalent absorber material for soft tissue. For bone, we use aluminum. From the conducted calibration measurements, we obtain a look-up table, connecting attenuation of materials with their beam hardening induced dark-field signal. We further demonstrate the spatial dependence of the effect of beam hardening due to the grating tiles and alignment.
For phantoms where we know the exact material composition, we can choose the appropriate equivalent absorber material for beam hardening correction. For humans, where we do not know the material composition, we simply use a mixture of half water and half aluminum.
Images of a barrel-shaped water phantom show that the corrections work quite well. Images of another, more complex phantom also show the validity of the applied corrections, but also raise the point that there are further processes not yet corrected for that influence the dark-field signal.
Finally, we show the impact of detector crosstalk, scatter from the analyzer grating, scatter from the sample, and beam hardening and their successful correction on dark-field radiographs of a human thorax.
The established correction ensure to a large extent that the signal in dark-field radiographs actually stems from the tissue micro-structure and not from artifacts. This enables an unobstructed evaluation of dark-field chest radiography for disease assessment.

In the second part of this thesis, the diagnostic potential of dark-field chest radiography for assessment of a wide-spread lung disease, COPD, is evaluated in detail. For a quantitative evaluation, the dark-field coefficient is introduced, which describes the dark-field signal generated per length of tissue. This dark-field coefficient is first evaluated in participants without lung impairments. It does not show a correlation with demographic parameters age, sex, and height, but does show a correlation with participant's weight. This will need further investigation, and should be corrected for in future studies.
Next, the dark-field radiographs are analyzed for their capability to assess the severity of pulmonary emphysema, the main manifestation of COPD, using CT scans as reference. We find a strong correlation of dark-field coefficient with the emphysema index from quantitative CT evaluation, and we show that the dark-field coefficient decreases with emphysema severity from visual assessment of CT scans.

Further, we developed a projection of emphysema segmentations from the CT scans to enable a qualitative comparison of local signal losses in dark-field radiography with CT-based emphysema location, and found that dark-field radiograph and CT-based emphysema projection agree very well.

Finally, the diagnostic value of dark-field chest radiography is compared with conventional radiography in a reader study. We demonstrate that dark-field chest radiography outperforms conventional radiography for emphysema diagnosis and staging, yielding higher AUC values for emphysema detection and higher effect sizes for differentiation of emphysema severity stages.

These evaluations prove the high diagnostic value of dark-field chest radiography as a low-dose, image-based tool for emphysema assessment, and constitute an important step in the way towards clinical application of dark-field chest radiography.

Outlook

Future dark-field chest radiography systems could be further enhanced regarding simplicity and image quality. One major advance would be the use of gratings large enough to cover the whole field of view. This would render the scanning process unnecessary, and thus enable a much faster and simpler image acquisition, potentially reducing artifacts from interferometer vibrations or patient motion. However, the smaller grating area in the slot-scanning system comes with advantages in cost from grating fabrication, and the smaller exposed volume reduces artifacts from sample scatter. The future will show which system design proves to be overall more favorable.

Another advancement in future systems could be a more precise patient positioning system, potentially eliminating the correlation of dark-field coefficient with patient weight by ensuring the same system sensitivity in all examinations. Besides further development of artifact correction methods, this could significantly enhance quantitative image evaluation.

For a wide-spread acceptance and use of dark-field chest radiography in the radiological community, its diagnostic value will have to be proven in larger studies, including more patients and more pathologies, ideally also conducted at other institutions. Especially the differentiation of different lung diseases has not yet been investigated at all, and may pose a challenge for dark-field chest radiography. Furthermore, its use for other applications besides lung imaging such as mammography or bone imaging may attract further attention to this new technique.

Finally, a further big step in the development of clincical X-ray dark-field imaging is its implementation in a CT system, yielding three-dimensional images rather than the two-dimensional projections from radiography. Recently, a group from this Chair realized a dark-field CT system in human scale [122]. Patient studies with this system will further increase the interest in X-ray dark-field imaging for medical applications.

Conclusion

With the quantitative corrections presented in this thesis, as well as those developed by others in this collaboration, dark-field chest radiography is ready to become a novel, quantitative image-based tool for lung assessment. Based on its evaluation for COPD assessment, I am fully convinced that it complements and improves conventional radiography, and will sonner or later find its way into clinical routine.

Bibliography

[1] A. Momose, "Recent advances in X-ray phase imaging", *Japanese Journal of Applied Physics*, vol. 44, no. 9R, p. 6355, 2005.

[2] M. Endrizzi, "X-ray phase-contrast imaging", *Nuclear instruments and methods in physics research section A: Accelerators, spectrometers, detectors and associated equipment*, vol. 878, pp. 88–98, 2018.

[3] U. Bonse and M. Hart, "An X-ray interferometer", *Applied Physics Letters*, vol. 6, no. 8, pp. 155–156, 1965.

[4] T. J. Davis, D. Gao, T. E. Gureyev, A. W. Stevenson, and S. W. Wilkins, "Phase-contrast imaging of weakly absorbing materials using hard X-rays", *Nature*, vol. 373, no. 6515, pp. 595–598, 1995.

[5] P. Cloetens *et al.*, "Hard X-ray phase imaging using simple propagation of a coherent synchrotron radiation beam", *Journal of Physics D: Applied Physics*, vol. 32, no. 10A, A145, 1999.

[6] A. Momose, S. Kawamoto, I. Koyama, Y. Hamaishi, K. Takai, and Y. Suzuki, "Demonstration of X-ray Talbot interferometry", *Japanese Journal of Applied Physics*, vol. 42, no. 7B, p. L866, 2003.

[7] T. Weitkamp, A. Diaz, C. David, F. Pfeiffer, M. Stampanoni, P. Cloetens, and E. Ziegler, "X-ray phase imaging with a grating interferometer", *Optics Express*, vol. 13, no. 16, pp. 6296–6304, 2005.

[8] F. Pfeiffer, T. Weitkamp, O. Bunk, and C. David, "Phase retrieval and differential phase-contrast imaging with low-brilliance X-ray sources", *Nature Physics*, vol. 2, no. 4, pp. 258–261, 2006.

[9] F. Pfeiffer *et al.*, "Hard-X-ray dark-field imaging using a grating interferometer", *Nature Materials*, vol. 7, no. 2, pp. 134–137, 2008.

[10] W. Yashiro, Y. Terui, K. Kawabata, and A. Momose, "On the origin of visibility contrast in X-ray Talbot interferometry", *Optics Express*, vol. 18, no. 16, p. 16 890, 2010.

[11] J. Graetz, A. Balles, R. Hanke, and S. Zabler, "Review and experimental verification of X-ray dark-field signal interpretations with respect to quantitative isotropic and anisotropic dark-field computed tomography", *Physics in Medicine & Biology*, vol. 65, no. 23, p. 235 017, 2020.

[12] Z.-T. Wang, K.-J. Kang, Z.-F. Huang, and Z.-Q. Chen, "Quantitative grating-based X-ray dark-field computed tomography", *Applied Physics Letters*, vol. 95, no. 9, 2009.

[13] D. Stutman, T. J. Beck, J. A. Carrino, and C. O. Bingham, "Talbot phase-contrast X-ray imaging for the small joints of the hand", *Physics in Medicine & Biology*, vol. 56, no. 17, p. 5697, 2011.

[14] E. Eggl *et al.*, "Prediction of vertebral failure load by using X-ray vector radiographic imaging", *Radiology*, vol. 275, no. 2, pp. 553–561, 2015.

[15] E.-M. Braig *et al.*, "X-ray dark-field radiography: Potential for visualization of monosodium urate deposition", *Investigative Radiology*, vol. 55, no. 8, pp. 494–498, 2020.

[16] M. Stampanoni *et al.*, "The first analysis and clinical evaluation of native breast tissue using differential phase-contrast mammography", *Investigative Radiology*, vol. 46, no. 12, pp. 801–806, 2011.

[17] K. Scherer *et al.*, "Improved diagnostics by assessing the micromorphology of breast calcifications via X-ray dark-field radiography", *Scientific Reports*, vol. 6, no. 1, pp. 1–11, 2016.

[18] M. Bech *et al.*, "In-vivo dark-field and phase-contrast X-ray imaging", *Scientific Reports*, vol. 3, no. 1, pp. 1–3, 2013.

[19] A. Velroyen *et al.*, "Grating-based X-ray dark-field computed tomography of living mice", *eBioMedicine*, vol. 2, no. 10, pp. 1500–1506, 2015.

[20] K. Hellbach *et al.*, "In vivo dark-field radiography for early diagnosis and staging of pulmonary emphysema", *Investigative Radiology*, vol. 50, no. 7, pp. 430–435, 2015.

[21] A. Yaroshenko *et al.*, "Improved in vivo assessment of pulmonary fibrosis in mice using X-ray dark-field radiography", *Scientific Reports*, vol. 5, no. 1, pp. 1–8, 2015.

[22] K. Hellbach *et al.*, "Facilitated diagnosis of pneumothoraces in newborn mice using X-ray dark-field radiography", *Investigative Radiology*, vol. 51, no. 10, pp. 597–601, 2016.

[23] K. Hellbach *et al.*, "X-ray dark-field radiography facilitates the diagnosis of pulmonary fibrosis in a mouse model", *Scientific Reports*, vol. 7, no. 1, pp. 1–6, 2017.

[24] K. Scherer *et al.*, "X-ray dark-field radiography-in-vivo diagnosis of lung cancer in mice", *Scientific Reports*, vol. 7, no. 1, pp. 1–9, 2017.

[25] J. Mohr *et al.*, "High aspect ratio gratings for X-ray phase contrast imaging", *AIP Conference Proceedings*, vol. 1466, no. 1, pp. 41–50, 2012.

[26] T. J. Schröter *et al.*, "Large field-of-view tiled grating structures for X-ray phase-contrast imaging", *Review of Scientific Instruments*, vol. 88, no. 1, p. 015 104, 2017.

[27] C. Kottler, F. Pfeiffer, O. Bunk, C. Grünzweig, and C. David, "Grating interferometer based scanning setup for hard X-ray phase contrast imaging", *Review of Scientific Instruments*, vol. 78, no. 4, p. 043 710, 2007.

[28] T. Koehler, H. Daerr, G. Martens, N. Kuhn, S. Löscher, U. van Stevendaal, and E. Roessl, "Slit-scanning differential X-ray phase-contrast mammography: Proof-of-concept experimental studies", *Medical Physics*, vol. 42, no. 4, pp. 1959–1965, 2015.

[29] L. B. Gromann *et al.*, "In-vivo X-ray dark-field chest radiography of a pig", *Scientific Reports*, vol. 7, no. 1, pp. 1–7, 2017.

[30] A. A. Fingerle *et al.*, "Imaging features in post-mortem X-ray dark-field chest radiographs and correlation with conventional X-ray and CT", *European Radiology Experimental*, vol. 3, no. 1, pp. 1–12, 2019.

[31] K. Willer *et al.*, "X-ray dark-field imaging of the human lung – a feasibility study on a deceased body", *PLOS ONE*, vol. 13, no. 9, e0204565, 2018.

[32] J. Andrejewski *et al.*, "Whole-body X-ray dark-field radiography of a human cadaver", *European Radiology Experimental*, vol. 5, no. 1, pp. 1–9, 2021.

[33] K. Willer *et al.*, "X-ray dark-field chest imaging for detection and quantification of emphysema in patients with chronic obstructive pulmonary disease: A diagnostic accuracy study", *The Lancet Digital Health*, vol. 3, no. 11, e733–e744, 2021.

[34] T. J. Vogl, W. Reith, and E. J. Rummeny, Eds., *Diagnostische und interventionelle Radiologie*. Springer-Verlag, 2011.

[35] D. McMorrow and J. Als-Nielsen, *Elements of modern X-ray physics*. John Wiley & Sons, 2011.

[36] Bundesamt für Strahlenschutz. "Benefit and risk of X-ray diagnostics". (2021), [Online]. Available: `https://www.bfs.de/EN/topics/ion/medicine/diagnostics/x-rays/benefit-risk.html` (visited on 04/20/2023).

[37] F. A. Mettler Jr, W. Huda, T. T. Yoshizumi, and M. Mahesh, "Effective doses in radiology and diagnostic nuclear medicine: A catalog", *Radiology*, vol. 248, no. 1, pp. 254–263, 2008.

[38] A. M. Den Harder *et al.*, "Emphysema quantification using chest CT: Influence of radiation dose reduction and reconstruction technique", *European Radiology Experimental*, vol. 2, no. 1, pp. 1–10, 2018.

[39] Z. Wang *et al.*, "Optimal threshold in CT quantification of emphysema", *European Radiology*, vol. 23, no. 4, pp. 975–984, 2013.

[40] J. Vilar-Palop, J. Vilar, I. Hernández-Aguado, I. González-Álvarez, and B. Lumbreras, "Updated effective doses in radiology", *Journal of Radiological Protection*, vol. 36, no. 4, p. 975, 2016.

[41] D. S. Gierada, T. K. Pilgram, B. R. Whiting, C. Hong, A. J. Bierhals, J. H. Kim, and K. T. Bae, "Comparison of standard- and low-radiation-dose CT for quantification of emphysema", *American Journal of Roentgenology*, vol. 188, no. 1, pp. 42–47, 2007.

[42] F. J. Larke *et al.*, "Estimated radiation dose associated with low-dose chest CT of average-size participants in the national lung screening trial", *American Journal of Roentgenology*, vol. 197, no. 5, pp. 1165–1169, 2011.

[43] U.S. Food and Drug Administration FDA. "Medical X-ray Imaging". (2020), [Online]. Available: `https://www.fda.gov/radiation-emitting-products/medical-imaging/medical-x-ray-imaging` (visited on 01/11/2023).

[44] Siemens Healthineers GmbH. "Siemens healthineers launches world's first CT scanner with photon-counting technology". (2021), [Online]. Available: `https://www.siemens-healthineers.com/press/releases/naeotomalpha` (visited on 01/11/2023).

[45] J. Scholz *et al.*, "X-ray dark-field radiography for in situ gout diagnosis by means of an ex vivo animal study", *Scientific Reports*, vol. 11, no. 1, pp. 1–11, 2021.

[46] T. Michel *et al.*, "On a dark-field signal generated by micrometer-sized calcifications in phase-contrast mammography", *Physics in Medicine & Biology*, vol. 58, no. 8, p. 2713, 2013.

[47] T. Baum *et al.*, "X-ray dark-field vector radiography – a novel technique for osteoporosis imaging", *Journal of Computer Assisted Tomography*, vol. 39, no. 2, pp. 286–289, 2015.

[48] S. Schleede *et al.*, "Emphysema diagnosis using X-ray dark-field imaging at a laser-driven compact synchrotron light source", *Proceedings of the National Academy of Sciences*, vol. 109, no. 44, pp. 17 880–17 885, 2012.

[49] A. Yaroshenko *et al.*, "Pulmonary emphysema diagnosis with a preclinical small-animal X-ray dark-field scatter-contrast scanner", *Radiology*, vol. 269, no. 2, pp. 427–433, 2013.

[50] F. G. Meinel *et al.*, "Improved diagnosis of pulmonary emphysema using in vivo dark-field radiography", *Investigative Radiology*, vol. 49, no. 10, pp. 653–658, 2014.

[51] A. Yaroshenko *et al.*, "Visualization of neonatal lung injury associated with mechanical ventilation using X-ray dark-field radiography", *Scientific Reports*, vol. 6, no. 1, pp. 1–8, 2016.

[52] F. De Marco *et al.*, "Contrast-to-noise ratios and thickness-normalized, ventilation-dependent signal levels in dark-field and conventional in vivo thorax radiographs of two pigs", *PLOS ONE*, vol. 14, no. 6, e0217858, 2019.

[53] K. Willer, "Development of a dark-field chest radiography prototype system for the initial clinical evaluation in COPD patients", Ph.D. dissertation, Technische Universität München, 2022.

[54] W. Noichl *et al.*, "Correction for mechanical inaccuracies in a scanning Talbot-Lau interferometer", *IEEE Transactions on Medical Imaging*, 2023, accepted. Preprint available on TechRxiv: `https://www.techrxiv.org/articles/preprint/Correction_for_mechanical_inaccuracies_in_a_scanning_Talbot-Lau_interferometer/21201475`.

[55] O. Glatter and O. Kratky, *Small angle X-ray acattering*. Academic Press, 1982.

[56] C. J. Gommes, S. Jaksch, and H. Frielinghaus, "Small-angle scattering for beginners", *Journal of Applied Crystallography*, vol. 54, no. 6, pp. 1832–1843, 2021.

[57] P. Modregger, F. Scattarella, B. Pinzer, C. David, R. Bellotti, and M. Stampanoni, "Imaging the ultrasmall-angle X-ray scattering distribution with grating interferometry", *Physical Review Letters*, vol. 108, no. 4, p. 048 101, 2012.

[58] A. Olivo and R. Speller, "A coded-aperture technique allowing X-ray phase contrast imaging with conventional sources", *Applied Physics Letters*, vol. 91, no. 7, p. 074 106, 2007.

[59] M. Endrizzi, B. Murat, P. Fromme, and A. Olivo, "Edge-illumination X-ray dark-field imaging for visualising defects in composite structures", *Composite Structures*, vol. 134, pp. 895–899, 2015.

[60] T. Weitkamp, C. David, C. Kottler, O. Bunk, and F. Pfeiffer, "Tomography with grating interferometers at low-brilliance sources", in *Developments in X-ray Tomography V*, SPIE, vol. 6318, 2006, pp. 249–258.

[61] H. F. Talbot, "LXXVI. facts relating to optical science. no. iv", *The London, Edinburgh, and Dublin Philosophical Magazine and Journal of Science*, vol. 9, no. 56, pp. 401–407, 1836.

[62] Lord Rayleigh, "XXV. on copying diffraction-gratings, and on some phenomena connected therewith", *The London, Edinburgh, and Dublin Philosophical Magazine and Journal of Science*, vol. 11, no. 67, pp. 196–205, 1881.

[63] A. W. Lohmann and J. A. Thomas, "Making an array illuminator based on the Talbot effect", *Applied Optics*, vol. 29, no. 29, pp. 4337–4340, 1990.

[64] T. J. Suleski, "Generation of Lohmann images from binary-phase Talbot array illuminators", *Applied Optics*, vol. 36, no. 20, pp. 4686–4691, 1997.

[65] F. D. De Marco, "Image reconstruction, preclinical studies, and signal formation investigations at a dark-field chest radiography setup", Ph.D. dissertation, Technische Universität München, 2021.

[66] M. Bech, T. H. Jensen, R. Feidenhans, O. Bunk, C. David, and F. Pfeiffer, "Soft-tissue phase-contrast tomography with an X-ray tube source", *Physics in Medicine & Biology*, vol. 54, no. 9, p. 2747, 2009.

[67] G. Pelzer *et al.*, "A beam hardening and dispersion correction for X-ray dark-field radiography", *Medical Physics*, vol. 43, no. 6Part1, pp. 2774–2779, 2016.

[68] M. Frank, "Clinical dark-field chest radiography – patient exposure and application for COVID-19-pneumonia", Ph.D. dissertation, Technische Universität München, 2023.

[69] V. Revol *et al.*, "X-ray interferometer with bent gratings: Towards larger fields of view", *Nuclear Instruments and Methods in Physics Research Section A: Accelerators, Spectrometers, Detectors and Associated Equipment*, vol. 648, no. SUPPL. 1, S302–S305, 2011.

[70] M. Frank *et al.*, "Dosimetry on first clinical dark-field chest radiography", *Medical Physics*, vol. 48, no. 10, pp. 6152–6159, 2021.

[71] R. C. Schick *et al.*, "Correction of motion artifacts in dark-field radiography of the human chest", *IEEE Transactions on Medical Imaging*, vol. 41, no. 4, pp. 895–902, 2021.

[72] A. Kurtz, *Physiologie*, 9th ed., H.-C. Pape, A. Kurtz, and S. Silbernagl, Eds. Thieme, 2019, ch. 8. Atmung.

[73] M. Ochs *et al.*, "The number of alveoli in the human lung", *American Journal of Respiratory and Critical Care Medicine*, vol. 169, no. 1, pp. 120–124, 2004.

[74] E. Roan and C. M. Waters, "What do we know about mechanical strain in lung alveoli?", *American Journal of Physiology – Lung Cellular and Molecular Physiology*, vol. 301, no. 5, pp. L625–L635, 2011.

[75] Medwell Inc. "Learn about COPD". (2018), [Online]. Available: `https://medwell.hk/learn-about-copd` (visited on 01/17/2023).

[76] S. C. Lareau, B. Fahy, P. Meek, and A. Wang, "Chronic obstructive pulmonary disease (COPD)", *American Journal of Respiratory and Critical Care Medicine*, vol. 199, no. 1, P1–P2, 2019.

[77] Global Initiative for Chronic Obstructive Lung Disease, "Global Strategy for the Diagnosis, Management, and Prevention of Chronic Obstructive Lung Disease. 2023 Report", Tech. Rep., 2023.

[78] W. M. Thurlbeck and N. Müller, "Emphysema: Definition, imaging, and quantification.", *American Journal of Roentgenology*, vol. 163, no. 5, pp. 1017–1025, 1994.

[79] A. Momose, "X-ray phase imaging reaching clinical uses", *Physica Medica*, vol. 79, pp. 93–102, 2020.

[80] T. Urban *et al.*, "Qualitative and quantitative assessment of emphysema using dark-field chest radiography", *Radiology*, vol. 303, no. 1, pp. 119–127, 2022.

[81] M. Frank *et al.*, "Dark-field chest X-ray imaging for the assessment of COVID-19-pneumonia", *Communications Medicine*, vol. 2, no. 1, pp. 1–9, 2022.

[82] T. Urban *et al.*, "Dark-field chest radiography outperforms conventional chest radiography for the diagnosis and staging of pulmonary emphysema", *Investigative Radiology*, 2023, published online ahead of print.

[83] F. T. Gassert *et al.*, "X-ray dark-field chest imaging: Qualitative and quantitative results in healthy humans", *Radiology*, vol. 301, no. 2, pp. 389–395, 2021.

[84] T. Urban, W. Noichl, K.-J. Engel, T. Koehler, and F. Pfeiffer, "Correction for X-ray scatter and detector crosstalk in dark-field radiography", *IEEE Transactions on Medical Imaging*, 2023, in revision. Preprint available on TechRxiv: `https://www.techrxiv.org/articles/preprint/Correction_for_X-ray_Scatter_and_Detector_Crosstalk_in_Dark-field_Radiography/22047098`.

[85] S. Vedantham, L. Shi, and A. Karellas, "Large-angle X-ray scatter in Talbot-Lau interferometry for breast imaging", *Physics in Medicine & Biology*, vol. 59, no. 21, pp. 6387–6400, 2014.

[86] J. Vignero, H. Bosmans, N. Marshall, and S. Rodríguez Pérez, "Minimizing the scatter contribution and spatial spread due to the absorption grating G2 in grating-based phase-contrast imaging", in *Medical Imaging 2018: Physics of Medical Imaging*, G.-H. Chen, J. Y. Lo, and T. Gilat Schmidt, Eds., vol. 10573, SPIE, 2018, 105734H.

[87] R. A. Brooks and G. Di Chiro, "Beam hardening in X-ray reconstructive tomography", *Physics in Medicine & Biology*, vol. 21, no. 3, p. 390, 1976.

[88] G. T. Herman, "Correction for beam hardening in computed tomography", *Physics in Medicine & Biology*, vol. 24, no. 1, p. 81, 1979.

[89] Y. Kyriakou, E. Meyer, D. Prell, and M. Kachelrieß, "Empirical beam hardening correction (EBHC) for CT", *Medical Physics*, vol. 37, no. 10, pp. 5179–5187, 2010.

[90] G. Van Gompel, K. Van Slambrouck, M. Defrise, K. J. Batenburg, J. De Mey, J. Sijbers, and J. Nuyts, "Iterative correction of beam hardening artifacts in CT", *Medical Physics*, vol. 38, no. S1, S36–S49, 2011.

[91] N. Bevins, K. Li, J. Zambelli, and G.-H. Chen, "Type II beam hardening artifacts in phase contrast imaging", in *Medical Imaging 2013: Physics of Medical Imaging*, SPIE, vol. 8668, 2013, pp. 308–313.

[92] F. De Marco *et al.*, "X-ray dark-field signal reduction due to hardening of the visibility spectrum", 2020, Preprint. Available on arXiv: `http://arxiv.org/abs/2011.03542`.

[93] A. Pandeshwar, M. Kagias, Z. Wang, and M. Stampanoni, "Modeling of beam hardening effects in a dual-phase X-ray grating interferometer for quantitative dark-field imaging", *Optics Express*, vol. 28, no. 13, pp. 19 187–19 204, 2020.

[94] W. Zhao, G. Ristic, and J. A. Rowlands, "X-ray imaging performance of structured cesium iodide scintillators", *Medical Physics*, vol. 31, no. 9, pp. 2594–2605, 2004.

[95] Physical Measurement Laboratory, National Institute of Standards and Technology, U.S. Department of Commerce. "Material Composition Data". (2017), [Online]. Available: `https://physics.nist.gov/cgi-bin/Star/compos.pl` (visited on 02/03/2023).

[96] Physical Measurement Laboratory, National Institute of Standards and Technology, U.S. Department of Commerce. "X-ray mass attenuation coefficients". (2019), [Online]. Available: `https://physics.nist.gov/PhysRefData/Xcom/html//xcom1.html` (visited on 02/03/2023).

[97] Siemens Healthineers GmbH. "Medical Accessories, OEM & Electronics". (2023), [Online]. Available: `https://bps.healthcare.siemens-healthineers.com/booneweb/index.html` (visited on 02/03/2023).

[98] M. Frank, "Characterization of a dark-field chest radiography scanner", M.S. thesis, Technische Universität München, 2018.

[99] Geant4 collaboration. "Geant4". (2023), [Online]. Available: `https://geant4.web.cern.ch/` (visited on 02/16/2023).

[100] S. Agostinelli *et al.*, "Geant4 – a simulation toolkit", *Nuclear Instruments and Methods in Physics Research Section A: Accelerators, Spectrometers, Detectors and Associated Equipment*, vol. 506, no. 3, pp. 250–303, 2003.

[101] J. Allison *et al.*, "Geant4 developments and applications", *IEEE Transactions on Nuclear Science*, vol. 53, no. 1, pp. 270–278, 2006.

[102] J. Allison *et al.*, "Recent developments in Geant4", *Nuclear Instruments and Methods in Physics Research Section A: Accelerators, Spectrometers, Detectors and Associated Equipment*, vol. 835, pp. 186–225, 2016.

[103] D. J. van der Laan, D. R. Schaart, M. C. Maas, F. J. Beekman, P. Bruyndonckx, and C. W. van Eijk, "Optical simulation of monolithic scintillator detectors using GATE/GEANT4", *Physics in Medicine & Biology*, vol. 55, no. 6, pp. 1659–1675, 2010.

[104] J. Nilsson, V. Cuplov, and M. Isaksson, "Identifying key surface parameters for optical photon transport in GEANT4/GATE simulations", *Applied Radiation and Isotopes*, vol. 103, pp. 15–24, 2015.

[105] Geant4 collaboration. "Geant4 Physics Reference Manual, Release 10.6". (2019), [Online]. Available: `https://geant4-userdoc.web.cern.ch/UsersGuides/PhysicsReferenceManual/BackupVersions/V10.6/html/index.html` (visited on 06/27/2023).

[106] D. E. Cullen, J. H. Hubbell, and L. Kissel, "EPDL97: The evaluated photo data library '97 version", Lawrence Livermore National Lab (LLNL), Livermore, CA (United States), Tech. Rep., 1997.

[107] L. Brombal, F. Arfelli, F. Brun, F. Longo, N. Poles, and L. Rigon, "X-ray differential phase-contrast imaging simulations with Geant4", *Journal of Physics D: Applied Physics*, vol. 55, no. 4, p. 045 102, 2021.

[108] V. N. Hansen, W. Swindell, and P. M. Evans, "Extraction of primary signal from EPIDs using only forward convolution", *Medical Physics*, vol. 24, no. 9, pp. 1477–1484, 1997.

[109] H. P. McAdams, E. Samei, J. Dobbins III, G. D. Tourassi, and C. E. Ravin, "Recent advances in chest radiography", *Radiology*, vol. 241, no. 3, pp. 663–683, 2006.

[110] G. T. Barnes, "Contrast and scatter in X-ray imaging", *Radiographics*, vol. 11, no. 2, pp. 307–323, 1991.

[111] D. Mentrup, S. Jockel, B. Menser, and U. Neitzel, "Iterative scatter correction for grid-less bedside chest radiography: Performance for a chest phantom", *Radiation Protection Dosimetry*, vol. 169, no. 1-4, pp. 308–312, 2016.

[112] M. Bertram, S. Hohmann, and J. Wiegert, "SU-FF-I-22: Scatter correction for flat detector cone-beam CT based on simulated sphere models", *Medical Physics*, vol. 34, no. 6, pp. 2342–2343, 2007.

[113] Geant4 collaboration. "DICOM Example". (2023), [Online]. Available: `https://geant4-userdoc.web.cern.ch/Doxygen/examples_doc/html/ExampleDICOM.html` (visited on 02/14/2023).

[114] T. Donath *et al.*, "Inverse geometry for grating-based X-ray phase-contrast imaging", *Journal of Applied Physics*, vol. 106, no. 5, p. 054 703, 2009.

[115] M. Chabior, T. Donath, C. David, M. Schuster, C. Schroer, and F. Pfeiffer, "Signal-to-noise ratio in X-ray dark-field imaging using a grating interferometer", *Journal of Applied Physics*, vol. 110, no. 5, p. 053 105, 2011.

[116] A. C. Thompson, D. Vaughan, *et al.*, *X-ray data booklet*. Lawrence Berkeley National Laboratory, University of California Berkeley, CA, 2001, vol. 8.

[117] R. Behling, *Modern Diagnostic X-Ray Sources: Technology, Manufacturing, Reliability.* CRC Press, 2021, pp. 226–231.

[118] E. Samel *et al.*, “Comparative scatter and dose performance of slot-scan and full-field digital chest radiography systems”, *Radiology*, vol. 235, no. 3, pp. 940–949, 2005.

[119] L. T. Niklason, J. A. Sorenson, and J. A. Nelson, “Scattered radiation in chest radiography”, *Medical Physics*, vol. 8, no. 5, pp. 677–681, 1981.

[120] C. E. Floyd, J. A. Baker, J. Y. Lo, and E. Ravin, “Measurement of scatter fractions in clinical bedside radiography”, *Radiology*, vol. 183, pp. 857–861, 1992.

[121] E. Braig *et al.*, “Direct quantitative material decomposition employing grating-based X-ray phase-contrast CT”, *Scientific Reports*, vol. 8, no. 1, p. 16 394, 2018.

[122] M. Viermetz *et al.*, “Dark-field computed tomography reaches the human scale”, *Proceedings of the National Academy of Sciences*, vol. 119, no. 8, e2118799119, 2022.

[123] M. Viermetz *et al.*, “Initial characterization of dark-field CT on a clinical gantry”, *IEEE Transactions on Medical Imaging*, vol. 42, no. 4, pp. 1035–1045, 2023.

[124] M. Decramer, W. Janssens, and M. Miravitlles, “Chronic obstructive pulmonary disease”, *The Lancet*, vol. 379, pp. 1341–1351, 9823 2012.

[125] C. J. Murray *et al.*, “Disability-adjusted life years (DALYs) for 291 diseases and injuries in 21 regions, 1990–2010: A systematic analysis for the Global Burden of Disease Study 2010”, *The Lancet*, vol. 380, no. 9859, pp. 2197–2223, 2012.

[126] T. Vos *et al.*, “Global, regional, and national incidence, prevalence, and years lived with disability for 310 diseases and injuries, 1990 – 2015: A systematic analysis for the Global Burden of Disease Study 2015”, *The Lancet*, vol. 388, no. 10053, pp. 1545–1602, 2016.

[127] C. O’Brien, P. Guest, S. Hill, and R. Stockley, “Physiological and radiological characterisation of patients diagnosed with chronic obstructive pulmonary disease in primary care”, *Thorax*, vol. 55, no. 8, pp. 635–642, 2000.

[128] A. Qaseem *et al.*, “Diagnosis and management of stable chronic obstructive pulmonary disease: A clinical practice guideline update from the American College of Physicians, American College of Chest Physicians, American Thoracic Society, and European Respiratory Society”, *Annals of Internal Medicine*, vol. 155, no. 3, pp. 179–191, 2011.

[129] D. A. Lynch *et al.*, “CT-based visual classification of emphysema: Association with mortality in the COPDGene study”, *Radiology*, vol. 288, no. 3, pp. 859–866, 2018.

[130] D. P. Johns, J. A. Walters, and E. H. Walters, “Diagnosis and early detection of COPD using spirometry”, *Journal of Thoracic Disease*, vol. 6, no. 11, p. 1557, 2014.

[131] D. A. Lynch *et al.*, “CT-definable subtypes of chronic obstructive pulmonary disease: A statement of the Fleischner Society”, *Radiology*, vol. 277, no. 1, p. 192, 2015.

[132] N. L. Müller, C. A. Staples, R. R. Miller, and R. T. Abboud, “’density mask’: An objective method to quantitate emphysema using computed tomography”, *CHEST*, vol. 94, no. 4, pp. 782–787, 1988.

[133] C. E. Ravin and H. G. Chotas, “Chest radiography”, *Radiology*, vol. 204, no. 3, pp. 593–600, 1997.

[134] C. Schaefer-Prokop and M. Prokop, “New imaging techniques in the treatment guidelines for lung cancer”, *European Respiratory Journal*, vol. 19, no. 35 suppl, 71s–83s, 2002.

[135] M. Miniati *et al.*, “Value of chest radiography in phenotyping chronic obstructive pulmonary disease”, *European Respiratory Journal*, vol. 31, no. 3, pp. 509–515, 2008.

[136] Global Initiative for Chronic Obstructive Lung Disease, “Global Strategy for the Diagnosis, Management, and Prevention of Chronic Obstructive Lung Disease. 2020 Report”, Tech. Rep., 2020.

[137] A. Tapfer *et al.*, “Experimental results from a preclinical X-ray phase-contrast CT scanner”, *Proceedings of the National Academy of Sciences*, vol. 109, no. 39, pp. 15 691–15 696, 2012.

[138] M. Bech, O. Bunk, T. Donath, R. Feidenhans, C. David, and F. Pfeiffer, “Quantitative X-ray dark-field computed tomography”, *Physics in Medicine & Biology*, vol. 55, no. 18, p. 5529, 2010.

[139] R. Pierce, D. Brown, M. Holmes, G. Cumming, and D. Denison, “Estimation of lung volumes from chest radiographs using shape information”, *Thorax*, vol. 34, no. 6, pp. 726–734, 1979.

[140] P. Buchberger, "Estimation of anatomical changes during the breathing cycle for evaluation of X-ray dark-field chest images", M.S. thesis, Technische Universität München, 2021.

[141] C. R. Harris *et al.*, "Array programming with numpy", *Nature*, vol. 585, no. 7825, pp. 357–362, 2020.

[142] P. Virtanen *et al.*, "Scipy 1.0: Fundamental algorithms for scientific computing in python", *Nature Methods*, vol. 17, no. 3, pp. 261–272, 2020.

[143] W. McKinney *et al.*, "Data structures for statistical computing in python", in *Proceedings of the 9th Python in Science Conference*, Austin, TX, vol. 445, 2010, pp. 51–56.

[144] R Core Team *et al.*, "R: A language and environment for statistical computing", 2013.

[145] N. A. Obuchowski, "Nonparametric analysis of clustered ROC curve data", *Biometrics*, vol. 53, no. 2, pp. 567–578, 1997.

[146] M. Kattau, "Comparison of grating-based attenuation and dark-field X-ray images with conventional radiography and computed tomography", M.S. thesis, Technische Universität München, 2020.

[147] M. Kattau *et al.*, "X-ray dark-field chest radiography: A reader study to evaluate the diagnostic quality of attenuation chest X-rays from a dual-contrast scanning prototype", *European Radiology*, 2023.

[148] K. Hellbach *et al.*, "X-ray dark-field imaging to depict acute lung inflammation in mice", *Scientific Reports*, vol. 8, no. 1, pp. 1–9, 2018.

[149] R. Burkhardt *et al.*, "Early detection of radiation-induced lung damage with X-ray dark-field radiography in mice", *European Radiology*, vol. 31, no. 6, pp. 4175–4183, 2021.

[150] B. El Kaddouri, M. J. Strand, D. Baraghoshi, S. M. Humphries, J.-P. Charbonnier, E. M. van Rikxoort, and D. A. Lynch, "Fleischner society visual emphysema CT patterns help predict progression of emphysema in current and former smokers: Results from the COPDGene study", *Radiology*, vol. 298, no. 2, p. 441, 2021.

[151] E. C. Oelsner *et al.*, "Per cent emphysema is associated with respiratory and lung cancer mortality in the general population: A cohort study", *Thorax*, vol. 71, no. 7, pp. 624–632, 2016.

[152] A. S. Oh *et al.*, "Visual emphysema at chest CT in GOLD stage 0 cigarette smokers predicts disease progression: Results from the COPDGene study", *Radiology*, vol. 296, no. 3, pp. 641–649, 2020.

[153] J. E. McDonough, L. Knudsen, A. C. Wright, W. M. Elliott, M. Ochs, and J. C. Hogg, "Regional differences in alveolar density in the human lung are related to lung height", *Journal of Applied Physiology*, vol. 118, no. 11, pp. 1429–1434, 2015.

[154] M. Gillooly and D. Lamb, "Airspace size in lungs of lifelong non-smokers: Effect of age and sex", *Thorax*, vol. 48, no. 1, pp. 39–43, 1993.

[155] E. K. Verbeken, M. Cauberghs, I. Mertens, J. Clement, J. M. Lauweryns, and K. P. Van de Woestijne, "The senile lung: Comparison with normal and emphysematous lungs 1. Structural aspects", *CHEST*, vol. 101, no. 3, pp. 793–799, 1992.

[156] M. Schultheiss *et al.*, "Per-pixel lung thickness and lung capacity estimation on chest x-rays using convolutional neural networks", 2021, Preprint. Available on arXiv: `https://arxiv.org/abs/2110.12509`.

[157] J. Heuchert, "Quantitative evaluation of clinical dark-field chest radiography", M.S. thesis, Technische Universität München, 2022.

[158] J.-A. Yeom *et al.*, "Emphysema quantification using ultra-low-dose chest CT: Efficacy of deep learning-based image reconstruction", *Medicina*, vol. 58, no. 7, p. 939, 2022.

[159] J. A. Walters, E. C. Hansen, D. P. Johns, E. L. Blizzard, E. H. Walters, and R. Wood-Baker, "A mixed methods study to compare models of spirometry delivery in primary care for patients at risk of COPD", *Thorax*, vol. 63, no. 5, pp. 408–414, 2008.

List of Figures

2.1 Conventional thorax radiographs . . . 3
2.2 Exemplary thorax and abdomen CT . . . 4
2.3 Exemplary Talbot carpets . . . 5
2.4 Influence of contrast mechanisms on the Talbot carpet . . . 6
2.5 Phase stepping and stepping curve . . . 6
2.6 Overview of the dark-field chest radiography system . . . 8
2.7 COPD and the human lung . . . 9

3.1 Scatter in dark-field radiography . . . 11
3.2 Beam hardening in dark-field radiography . . . 12
3.3 Exemplary stepping curves after crosstalk between two pixels . . . 13
3.4 Effect of crosstalk on the visibility . . . 14
3.5 Theory of beam hardening in dark-field radiography . . . 15
3.6 The dark-field chest radiography system in Geant4 . . . 17
3.7 Measurements for scatter and crosstalk characterization . . . 18
3.8 Monte-Carlo simulation of scatter from the the analyzer grating . . . 19
3.9 Monte-Carlo simulations of experiments for verification of sample scatter estimates . . . 20
3.10 Monte-Carlo simulations of experiments for beam hardening characterization . . . 21
3.11 Flowchart of processing pipeline . . . 23
3.12 Fit of detector crosstalk kernel . . . 24
3.13 Measurement and verification of detector crosstalk estimates . . . 25
3.14 The kernel for scatter from the analyzer grating . . . 25
3.15 Contributions to scatter from the analyzer grating . . . 26
3.16 Dependency of scatter from the analyzer grating on position in the field of view . . . 26
3.17 Spectra of photons scattered at the analyzer grating . . . 27
3.18 Photons scattered back to the analyzer grating . . . 27
3.19 Validation of kernel for scatter from the analyzer grating with full-field simulation . . . 27
3.20 Verification of intensities estimated with the kernel for scatter from the analyzer grating . . . 28
3.21 Comparison of full Monte-Carlo simulation and scatter estimation for the water phantom . . . 28
3.22 Verification of sample scatter estimation with the water phantom measurement . . . 29
3.23 Comparison of full Monte-Carlo simulation and scatter estimation for the LUNGMAN phantom 30
3.24 Scatter in a system with full-field gratings . . . 31
3.25 Scatter in beam hardening measurements . . . 31
3.26 Dark-field signal of POM for the two phantoms . . . 32
3.27 Beam hardening induced dark-field signal of water . . . 33
3.28 Beam hardening calibration curves for the different materials . . . 33
3.29 Validation of corrections with the barrel-shaped water phantom . . . 34
3.30 Validation of corrections with the constancy phantom . . . 34
3.31 Effect of corrections on dark-field chest radiographs in pa orientation . . . 36
3.32 Quantitative evaluation of corrections on pa images . . . 36
3.33 Effect of corrections on dark-field chest radiographs in lat orientation . . . 37
3.34 Quantitative evaluation of corrections on lat images . . . 37

4.1 Quantitative CT evaluation and emphysema projection . . . 44
4.2 Comparison of attenuation-based and dark-field radiographs for participants without lung impairment . . . 47
4.3 Details for comparison of attenuation-based and dark-field radiographs . . . 47
4.4 Statistical analysis of the dark-field signal of participants without lung impairment . . . 48

4.5 Comparison of dark-field radiography and CT-based emphysema assessment for participants with a significant emphysema index 48
4.6 Comparison of dark-field radiography and CT-based emphysema assessment for participants with a non-significant emphysema index 49
4.7 Dark-field coefficient and CT-based emphysema evaluation 49
4.8 Comparison of conventional and dark-field chest radiography 50
4.9 Statistical analysis of reader study 50

List of Tables

2.1 Interferometer parameters 7

3.1 Phantoms for beam hardening calibration 22
3.2 Material thicknesses in the constancy phantom 23

4.1 Characteristics of all participants 46
4.2 Characteristics of participants in the quantitative analysis 46
4.3 Characteristics of participants in the analysis of dark-field signal of healthy lungs 46
4.4 Statistical evaluation of dark-field coefficients 49
4.5 Statistical evaluation of reader study 51

List of Abbreviations

Acronyms

CT X-ray computed tomography

COPD chronic obstructive pulmonary disease

EI emphysema index

HU Hounsfield units

pa posterior-anterior

lat lateral

ROC receiver-operating-characteristic

AUC area under the curve

POM polyoxymethylen

PMMA polymethylmethacrylat

CNN convolutional neural network

SAXS small-angle X-ray scattering

Radiologists

A.A.F. Dr. Alexander A. Fingerle

A.P.S. Dr. Andreas P. Sauter

F.T.G. Dr. Dr. Florian T. Gassert

J.H.B. Dr. Jannis H. Bodden

D.P. Prof. Dr. Daniela Pfeiffer

Scientific Contributions

Publications with first or shared first authorship

- **Urban, Theresa***; Gassert, Florian T.*; Frank, Manuela; Willer, Konstantin; Noichl, Wolfgang; Buchberger, Philipp; Schick, Rafael C.; Koehler, Thomas; Bodden, Jannis H.; Fingerle, Alexander A.; Sauter, Andreas P.; Makowski, Marcus R.; Pfeiffer, Franz*; Pfeiffer, Daniela*: Qualitative and Quantitative Assessment of Emphysema Using Dark-field Chest Radiography. Radiology 303(1), 119-127, 2022
- Gassert, Florian T.*; **Urban, Theresa***; Frank, Manuela; Willer, Konstantin; Noichl, Wolfgang; Buchberger, Philipp; Schick, Rafael; Koehler, Thomas; von Berg, Jens; Fingerle, Alexander A.; Sauter, Andreas P.; Makowski, Marcus R.; Pfeiffer, Daniela*; Pfeiffer, Franz*: X-ray Dark-field Chest Imaging: Qualitative and Quantitative Results in Healthy Humans. Radiology 301(2), 389-395, 2021
- **Urban, Theresa***; Sauter, Andreas P.*, Frank, Manuela; Willer, Konstantin; Noichl, Wolfgang; Bast, Henriette; Schick, Rafael; Herzen, Julia; Koehler, Thomas; Gassert, Florian T.; Bodden, Jannis H.; Fingerle, Alexander A.; Gleich, Bernhard; Renger, Bernhard; Makowski, Marcus R.; Pfeiffer, Franz*; Pfeiffer, Daniela*: Dark-field Chest Radiography Outperforms Conventional Chest Radiography for the Diagnosis and Stanging of Pulmonary Emphysema. Investigative Radiology, published online ahead of print, 2023
- **Urban, Theresa**, Noichl, Wolfgang; Engel, Klaus Juergen; Koehler, Thomas; Pfeiffer, Franz: Correction for X-ray Scatter and Detector Crosstalk in Dark-field Radiography. IEEE Transactions on Medical Imaging, in revision, 2023
- Gassert, Florian T.*; **Urban, Theresa***; Kufner, Alexander; Frank, Manuela; Feuerriegel, Georg C.; Baum, Thomas; Makowski, Marcus R.; Braun, Christian; Pfeiffer, Daniela; Schwaiger, Benedikt J; Pfeiffer, Franz*; Gersing, Alexandra S.*: Dark-field X-ray imaging for the assessment of osteoporosis. Frontiers in Physiology, in revision, 2023
- **Urban, Theresa***; Gassert, Florian T.*; Frank, Manuela;Schick, Rafael; Bast, Henriette; Bodden, Jannis; Sauter, Andreas;Fingerle, Alexander; Koehler, Thomas; Makowski, Marcus R.; Pfeiffer,Daniela; Pfeiffer, Franz: Dark-field Chest Radiography Signal Characteristics in Inspiration and Expiration. In submission, 2023

Publications with co-authorship

- De Marco, Fabio; Andrejewski, Jana; **Urban, Theresa**; Willer, Konstantin; Gromann, Lukas; Koehler, Thomas; Maack, Hanns-Ingo; Herzen, Julia; Pfeiffer, Franz: X-ray dark-field signal reduction due to hardening of the visibility spectrum. IEEE Transactions on Medical Imaging, submitted, 2023
- Noichl, Wolfgang; De Marco, Fabio; Willer, Konstantin; **Urban, Theresa**; Frank, Manuela; Schick, Rafael; Gleich, Bernhard; Hehn, Lorenz; Gustschin, Alex; Meyer, Pascal; Koehler, Thomas; Maack, Ingo; Engel, Klaus-Jürgen; Lundt, Bernd; Renger, Bernhard; Fingerle, Alexander; Pfeiffer, Daniela; Rummeny, Ernst; Herzen, Julia; Pfeiffer, Franz: Correction for mechanical inaccuracies in a scanning Talbot-Lau interferometer. IEEE Transactions on Medical Imaging, in press, 2023
- Frank, Manuela; Willer, Konstantin; **Urban, Theresa**; Noichl, Wolfgang; Schick, Rafael; De Marco, Fabio; Koehler, Thomas; Maack, Ingo; Pfeiffer, Daniela; Renger, Bernhard; Pfeiffer, Franz: Exposure Control at the First Dark-field Chest Radiography Demonstrator System. Medical Physics, in revision, 2023

- Gassert, Florian T.; Bast, Henriette; **Urban, Theresa**; Frank, Manuela; Gassert, Felix G.; Willer, Konstantin; Schick, Rafael; Renger, Bernhard; Koehler, Thomas; Karrer, Alexandra; Sauter, Andreas P.; Fingerle, Alexander A.; Makowski, Marcus R.; Pfeiffer, Franz; Pfeiffer, Daniela: Comparison of Dark-field Chest Radiography and CT for the Assessment of COVID-19 Pneumonia. Medica Physica, under review, 2023

- Kattau, Margarete; Willer, Konstantin; Noichl, Wolfgang; **Urban, Theresa**; Frank, Manuela; De Marco, Fabio; Schick, Rafael; Koehler, Thomas; Maack, Hanns-Ingo; Renger, Bernhard; Renz, Martin; Sauter, Andreas; Leonhardt, Yannik; Fingerle, Alexander; Makowski, Marcus; Pfeiffer, Daniela; Pfeiffer, Franz: X-ray dark-field chest radiography: a reader study to evaluate the diagnostic quality of attenuation chest X-rays from a dual-contrast scanning prototype. European Radiology, 2023

- Gassert, Florian T.*; Frank, Manuela*; De Marco, Fabio; Willer, Konstantin; **Urban, Theresa**; Herzen, Julia; Fingerle, Alexander A.; Sauter, Andreas P.; Makowski, Marcus R.; Kriner, Fabian; Fischer, Florian; Braun, Christian; Pfeiffer, Franz; Pfeiffer, Daniela: Assessment of Inflation in a Human Cadaveric Lung with Dark-field Chest Radiography. Radiology: Cardiothoracic Imaging 4(6), e220093, 2022

- Frank, Manuela; Gassert, Florian T.; **Urban, Theresa**; Willer Konstantin; Noichl, Wolfgang; Schick, Rafael; Schultheiss, Manuel; Viermetz, Manuel; Gleich, Bernhard; De Marco, Fabio; Herzen, Julia; Koehler, Thomas; Engel, Klaus Juergen; Renger, Bernhard; Gassert, Felix G.; Sauter, Andreas P.; Fingerle, Alexander A.; Haller, Bernhard; Makowski, Marcus R.; Pfeiffer, Daniela; Pfeiffer, Franz: Dark-field chest X-ray imaging for the assessment of COVID-19-pneumonia. Nature Communications Medicine 2(1), 1–9, 2022

- Gassert, Florian T.; **Urban, Theresa**; Pfeiffer, Daniela; Pfeiffer, Franz: Dark-field Chest Radiography of Combined Pulmonary Fibrosis and Emphysema. Radiology: Cardiothoracic Imaging 4(4), e220085, 2022

- Zimmermann, Gregor S.; Fingerle, Alexander A.; Renger, Bernhard; Laugwitz, Karl-Ludwig; Hautmann, Hubert; Sauter, Andreas; Meurer, Felix; Gassert, Florian T.; Bodden, Jannis; Müller-Leisse, Christina; Renz, Martin; Rummeny, Ernst J.; Makowski, Marcus R.; Willer, Konstantin; Noichl, Wolfgang; De Marco, Fabio; Frank, Manuela; **Urban, Theresa**; Schick, Rafael C.; Herzen, Julia; Koehler, Thomas; Haller, Bernhard; Pfeiffer, Daniela; Pfeiffer, Franz: Dark-field chest x-ray imaging: first experience in patients with alpha1-antitrypsin deficiency. European Radiology Experimental 6(1), 1-9, 2022

- Frank, Manuela; **Urban, Theresa**; Willer, Konstantin; Noichl, Wolfgang; De Marco, Fabio; Schick, Rafael; Gleich, Bernhard; Schegerer, Alexander; Lechel, Ursula; Meyer, Pascal; Mohr, Juergen; Koehler, Thomas; Yaroshenko, Andre; Maack, Ingo; Pralow, Thomas; Proksa, Roland; Renger, Bernhard; Noël, Peter; Fingerle, Alexander; Pfeiffer, Daniela; Rummeny, Ernst; Herzen, Julia; Pfeiffer, Franz: Dosimetry on first clinical dark-field chest radiography. Medical Physics 48(10), 6152-6159, 2021

- Willer, Konstantin*; Fingerle, Alexander A*; Noichl, Wolfgang; De Marco, Fabio; Frank, Manuela; **Urban, Theresa**; Schick, Rafael; Gustschin, Alex; Gleich, Bernhard; Herzen, Julia; Koehler, Thomas; Yaroshenko, Andre; Pralow, Thomas; Zimmermann, Gregor S; Renger, Bernhard; Sauter, Andreas P; Pfeiffer, Daniela; Makowski, Marcus R; Rummeny, Ernst J; Grenier, Philippe A; Pfeiffer, Franz: X-ray dark-field chest imaging for detection and quantification of emphysema in patients with chronic obstructive pulmonary disease: a diagnostic accuracy study. The Lancet Digital Health 3(11), e733-e744, 2021

- Andrejewski, Jana; De Marco, Fabio; Willer, Konstantin; Noichl, Wolfgang; **Urban, Theresa**; Frank, Manuela; Gustschin, Alex; Meyer, Pascal; Koehler, Thomas; Pfeiffer, Franz; Herzen, Julia: Retrieval of 3D information in X-ray dark-field imaging with a large field of view. Scientific Reports 11(1), 1-8, 2021

- Schick, Rafael C.*; Koehler, Thomas*; Noichl, Wolfgang; De Marco, Fabio; Willer, Konstantin; **Urban, Theresa**; Frank, Manuela; Pralow, Thomas; Maack, Ingo; Prevrhal, Sven; Lundt, Bernd; Fingerle, Alexander; Pfeiffer, Daniela; Herzen, Julia; Pfeiffer, Franz: Correction of Motion Artifacts in Dark-field Radiography of the Human Chest. IEEE Transactions on Medical Imaging 41(4), 895-902, 2021

* shared authorship

Presentations

- "Dark-field chest radiography outperforms conventional radiography for the diagnosis and staging of pulmonary emphysema" – Poster presentation at the Annual Meeting of the Radiological Society of North America (RSNA), November 2022, Chicago, United States of America

- "Correction for optical and x-ray scatter in dark-field radiography" – Oral presentation at the IEEE Nuclear Science Symposium, Medical Imaging Conference and Room Temperature Semiconductor Detector Conference (IEEE MIC), November 2022, Milano, Italy

- "Dark-field chest radiography - First clinical results with COPD and Covid-19" – Invited Talk at the International Symposium on Medical Applications of X-ray, Phase-Contrast & Photon-Counting (IMXP), August 2022, Garching, Germany

- "Detection and diagnosis of pulmonary emphysema in COPD-patients using X-ray dark-field chest radiography" – Oral presentation at the European Congress of Radiology (ECR), July 2022, Vienna, Austria

- "Comparison of conventional and dark-field chest radiography for the diagnosis of pulmonary emphysema" – Oral presentation at the European Congress of Radiology (ECR) Overture, March 2022, Online

- "Vergleich von Dunkelfeld-Radiographien mit CT-basierter Emphysem-Quantifizierung" – Oral presentation at the Jahrestagung der Deutschen Gesellschaft für Medizinische Physik (DGMP), September 2020, Online

- "Dark-field chest radiography - Influence of the breathing state on image appareance" – Oral presentation at the 9th International Symposium on Biomedical Applications of X-ray Phase Contrast Imaging (IMXP), January 2020, Munich, Germany

- "Variation of dark-field chest X-ray signal strength with breathing state" – Oral presentation at the Annual Meeting of the Radiological Society of North America (RSNA), December 2019, Chicago, United States of America

- "Variation of dark-field chest X-ray signal strength with breathing state" – Oral presentation at the 5th International Conference on X-ray and Neutron Phase Imaging with Gratings (XNPIG), October 2019, Sendai, Japan